STRUCTURAL INVESTIGATION OF SILK FIBROIN-BASED MEMBRANES

A Thesis
Presented to
The Academic Faculty

by

Brett Wallet

In Partial Fulfillment
of the Requirements for the Degree
Master of Science in the
School of Materials Science and Engineering

Georgia Institute of Technology
May 2014

STRUCTURAL INVESTIGATION OF SILK FIBROIN-BASED MEMBRANES

Approved by:

Dr. Vladimir Tsukruk, Advisor
School of Materials Science and Engineering
Georgia Institute of Technology

Dr. Valeria Milam
School of Materials Science and Engineering
Georgia Institute of Technology

Dr. Meisha Shofner
School of Materials Science and Engineering
Georgia Institute of Technology

Date Approved: April 3, 2014

Dedicated to George & Corinne Wallet

ACKNOWLEDGEMENTS

I would like to first and foremost acknowledge Professor Tsukruk, my research advisor throughout the duration of my studies in the MSE department at Georgia Tech. I sincerely appreciate his amiability towards me, and the patience and accommodation he has bestowed while always maintaining a professional demeanor. His extensive knowledge and understanding of the MSE field as related to biomaterials and surface engineering furnished my own understanding and outlook with respect to meaningful and productive research. I would also like to express my gratitude towards my committee members, Professor Meisha Shofner and Professor Valeria Milam, for their considerate participation and bearing with me amid previous trials while progressing through the MSE graduate program at Georgia Tech.

Special thanks is extended to Professor Eugenia Kharlampieva who provided valuable mentorship, insightful instruction, and constant encouragement in the course of my research efforts. Furthermore, I am grateful for the continued assistance throughout my experimental work and helpful support during my thesis study provided by Dr. Maneesh Gupta. For all of the contributions towards my experiments given by Dr. Kyle Anderson, Professor Veronika Kozlovskaya, and Dr. Katie Campbell-Proszowska, I convey my appreciativeness.

Finally, I express my thankfulness to my family and well received professional colleagues for their expressed interest and encouragement in my thesis study.

TABLE OF CONTENTS

Page

LIST OF TABLES

LIST OF FIGURES

LIST OF SYMBOLS AND ABBREVIATIONS

ZrO_2	Zirconia
SiO_2	Silica
TiO_2	Titania
UV	Ultraviolet
LbL	Layer-by-Layer Assembly
SA-LbL	Spin-Assisted Layer-by-Layer Assembly
AgNPLs	Silver Nanoplatelets
MeOH	Methanol
ATR-FTIR	Attenuated Total Reflection Fourier-Transform Infrared Spectroscopy
2D	Two-dimensional
3D	Three-dimensional
GNPs	Gold nanoparticles
POSS	Polyhedral Oligomeric Silsequioxane Nanoparticles
MMT	Clay Montmorillonite Nanoplatelets
NR	Neutron Reflectivity
AFM	Atomic Force Microscopy
SEM	Scanning Electron Microscopy
FFT	Fast Fourier-Transform
D_2O	Heavy Water
PDMS	Polydimethylsiloxane
GA	Glutaraldehyde

RMS	Surface Microroughness
PVA	Polyvinyl Alcohol
PDDA	Poly(diallydimethylammonium)
TEM	Transmission Electron Microscopy
MWCO	Molecular Weight Cutoff
DIC	Differential Interface Contrast
CCD	Charged Coupled Device
SLD	Scattering Length Density
SNS-LR	Spallation Neutron Source - Liquid Reflectomer
ORNL	Oak Ridge National Laboratory
IL	Interference Lithography
HAuCl4	Gold Chloride
SU-8	Bisphenol-A Novolac Negative Photoresist
PS	Polystyrene
PSS-PAH	Polystrene Sulfonate - Polyanhydride

SUMMARY

Silk fibroin has created a surge of interest for use as organic material due to its optical transparency, biocompatibility, biodegradability, and excellent physical properties. However, the implementation of silk films and structures into biomedical and sensing devices has been relatively low due to a lack of understanding of the mechanisms involved in such implementation. Increasing need for multifunctional high-performance organic materials has caused an emphasis on the ability of researchers to spatiotemporally pattern and control the structure and consequently functional properties of materials. Silk fibroin displays high potential for use as a controllable biomaterial that can be formed into a myriad of different structures for various applications. By implementation of an aqueous silk solution approach combining various fabrication techniques, several different pristine-silk and silk-composite membranes have been developed to investigate the importance of internal structuring. Different methods of investigation include: 1) incorporation of reinforcing nanoparticles within the silk matrix; 2) neutron reflectivity measurements of ultrathin silk films; 3) film patterning with nanoscale features followed by boundary organized surface mineralization of inorganic nanoparticles. The ultimate goal will be to provide fundamental data assisting in an increased knowledge of silk fibroin-based membranes and the effect of secondary structures on properties of interest.

CHAPTER I

SILK FIBROIN AS A NANOMATERIAL

1.1 Critical Review

The key emphasis of current research on silk-based structures has revolved around the field of biotechnology, especially cellular scaffolds for tissue regeneration. Other areas of interest include mineralization of the surface, optical sensing, and chemical sensing. Due to various inherent properties and ease of fabrication techniques, silk fibroin has presented itself as a novel material for applications in such fields of research. Silk fibroin undergoes a transition from an amorphous state, silk I, to a partially crystalline one, silk II, upon exposure to heat, organic solvents, dehydration, and mechanical stress. The fundamental details of this transition will be discussed later, but for now, it is of importance to note that most research involves the utilization and comparison of both silk structures.

1.1.1 Bionanocomposites

Bioenabled and bioderived nanocomposite materials have been designed and widely investigated as prospective advanced materials fabricated under environmentally benign conditions.[1,2] Biomaterials-based nanocomposites exhibit novel synergetic properties by integrating features from both bioderived and inorganic components, and provide potential as biomedical materials and biomolecular devices.[3] Variations in assembly techniques and conditions provide a broad range of biological surfaces and structures, while incorporation of natural polymers, degradable materials, enzymes, and proteins increases the broadness of possible applications.[4] These nanomaterials are prepared by the physical mixing of two components, *in situ* synthesis of inorganic nanostructures within organic matrixes, or by employing bottom-up approaches with step-by-step component assembly.[5,6] The latter strategy affords nanomaterials with enhanced interfacial strength because it overcomes problems with poorly controlled phase separation and allows precisely tailored composition, function, and tunable thickness, all at the nm-scale. A novel preparation approach is presented and reviewed in Chapter II.

The control of the structural organization of proteins at interfaces with inorganic materials is crucially important for the design of bionanocomposite materials. Biology is full of examples in which material interfaces have been designed and assembled to provide unique properties, and strategies have been demonstrated to exhibit specific molecular control over these interfaces through self-assembly driven processes.[7,8] Furthermore, simple mixing of biological entities (i.e. proteins, organic molecules, enzymes, antibodies) in solution prior to film fabrication can provide a route for their maintained function within the organic matrix. [9]

1.1.2 Silk Fibroin

Silk fibroin presents itself as a promising biomaterial candidate for many medical applications because of its unique structure, versatility in processing, non-immunogenic response upon *in vivo* implantation, biocompatibility, availability of different biomaterial morphologies, ease of sterilization, thermal stability, surface chemistry for facile chemical modifications, and controllable degradation features. [10,11] Tissue engineering and biomedical applications are explored because of its biocompatibility and biodegradability.[12,13,14] The degradation kinetics are related to several variables such as structural and morphological aspects of the polymer, processing conditions, features of the surrounding biological environment, and stresses induced either chemically or physically.[15] Utilization of biodegradable materials for drug delivery and tissue engineering systems is in increasing demand, and has already been demonstrated with silk as a microfluidic device.[16] More specifically, silk fibroin protein has become an appealing biomaterial for implementation as a key component in hybrid bionanocomposites with advanced performance for applications ranging from sensing and optical systems to advanced structural composites.[7,9,10,17,18,19,20] Several inherent physical properties suggest silk fibroin as a prospective candidate material in these areas including optical transparency, high strength combined with high elastic modulus, elongation to break, and toughness.[21,22,23]

However, silk-based membranes and films still lack the necessary mechanical robustness for demanding applications in biotechnology, and therefore an inorganic filler is frequently implemented to reinforce silk-based nanocomposites. To date, reinforced silk-based bulk materials, films, and fibers have been obtained by utilizing inorganic nanofillers such as carbon nanotubes, zirconia (ZrO_2), silica (SiO_2), titania (TiO_2), apatite, or metal particles.[24,25] Such an approach is highlighted in the review of the studies documented in Chapter II. Moreover, silk materials possess remarkable optical properties such as near-perfect transparency in a visible range.[26] In this respect, nanocomposites, consisting of transparent organic or polymeric matrices with embedded particles of diameters less than 50-100 nm, are finding increased attention in research on optical materials due to the low light intensity loss by scattering which is effectively reduced when compared to incorporated particles of larger dimensions.[27] The low light intensity loss is an important characteristic of these nanocomposites for optical applications such as nonlinear optics photoconductivity and as transparent ultraviolet (UV) - absorbing layers.[28]

1.1.3 Reconstituted Silk Solution

The processing challenges in handling these high molecular weight proteins without aggregation has led to the use of reconstituted or regenerated silk fibroin aqueous solution for the fabrication of silk films and complex topographical structures such as fibers and microcapsules.[22,24,29,30,31,32,33,34,35,36,37,38] Production of silk fibroin solution for composite formation starts with the purification of harvested *Bombyx mori* cocoons, shown in Figure 1.1, by removing sericin, the glue-like binding component of silk. Sericin is a water-soluble glycoprotein that binds fibroin filaments[7], and although it contributes to increased mechanical properties of silk, it also has detrimental effects on the integration of silk into optical and biomedical devices.[39] The optical transparency of silk films necessary to minimize scattering is decreased by sericin and it also proves to be undesirable for biomedical applications due to the associated inflammatory response.[39] Once sericin has been removed, the remaining silk solution in diluted form can then be used as is for the deposition and fabrication of films and structures. Furthermore, the all-aqueous approach allows for direct incorporation of reactive biological and inorganic components in the fabrication of devices to add selective functions.[8] Each of the individual studies presented in Chapters II, III, and IV utilize this silk solution in the fabrication method, and a schematic of the process is displayed in Figure 1.2.

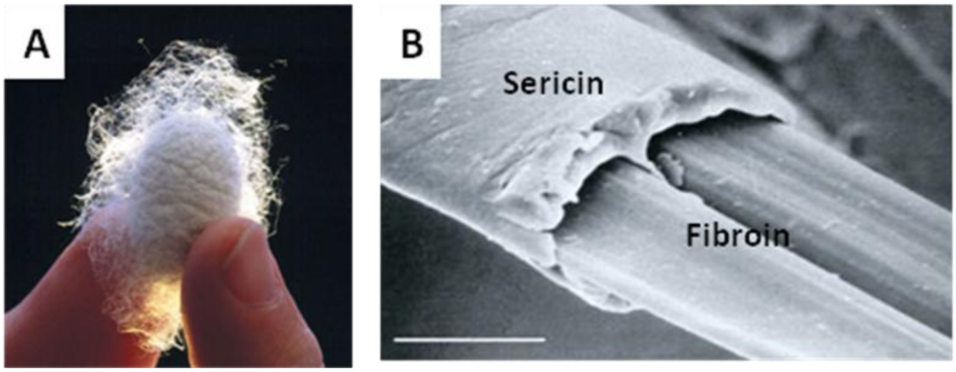

Figure 1.1: Images of a harvested *Bombyx mori* cocoon (A) and unpurified silk fiber (B), from Z. Shao and F. Vollrath, *Nature*, (2002) 418, 741.

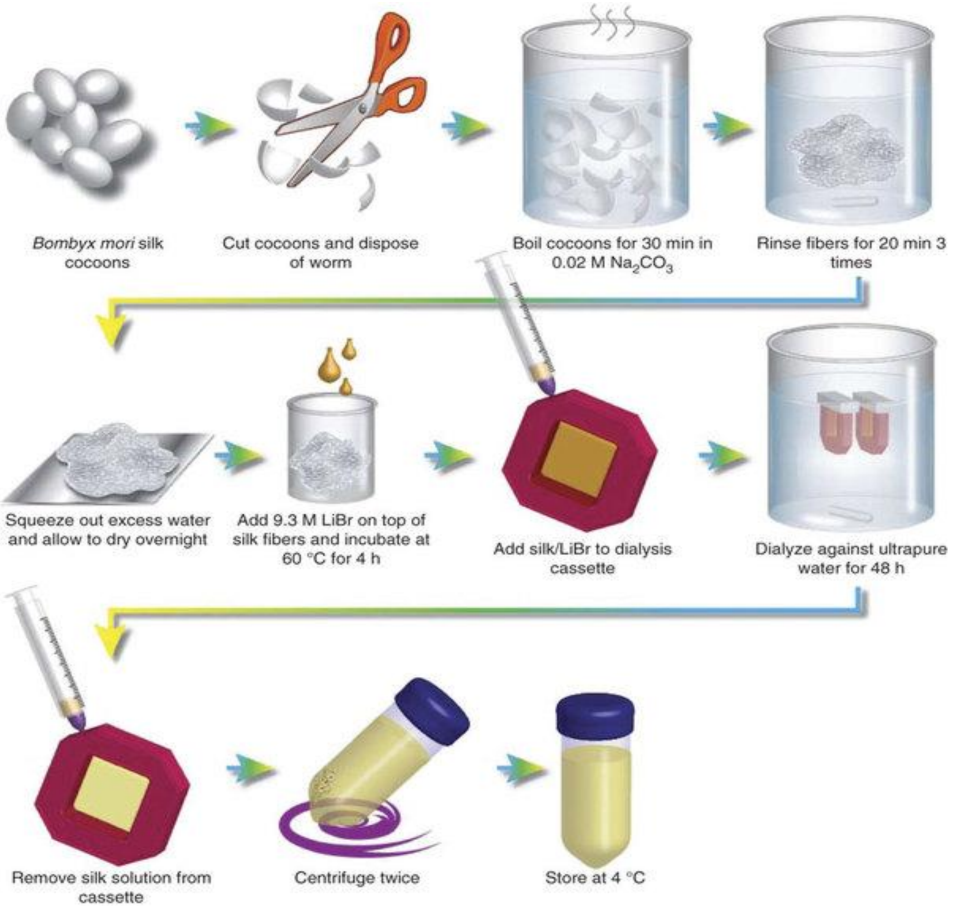

Figure 1.2: Schematic representation of the silk fibroin extraction procedure, from D. Rockwood et al., *Nature Protocols*, (2011) 6, 1612.

Silk fibroin displays high potential for use as a controllable biomaterial that can be formed into a myriad of different structures for various applications. Recent research has explored the ability to fabricate silk fibroin into various geometries including films, non-woven mats, sponges, and fibers from purified, aqueous silk solution for use as a cellular scaffold (Figure 1.3).[11,38,40,41,42,43,44,45] Characteristics of silk proteins such as cytocompatibility, controllable degradation rates, robust mechanical strength, and ambient aqueous processing are reasons why its use is explored in tissue engineering and cellular regeneration applications.[22] Studies have shown the ability to use the silk solution technique for enzyme immobilization[20], correlating the mode of processing with enzyme stability (i.e. glucose oxidase)[44], *in-vivo* and *in-vitro* cell culture[39], and evaluation of cytoxicity, adhesion, cell cycle and apoptosis supported by a silk-based membrane.[43]

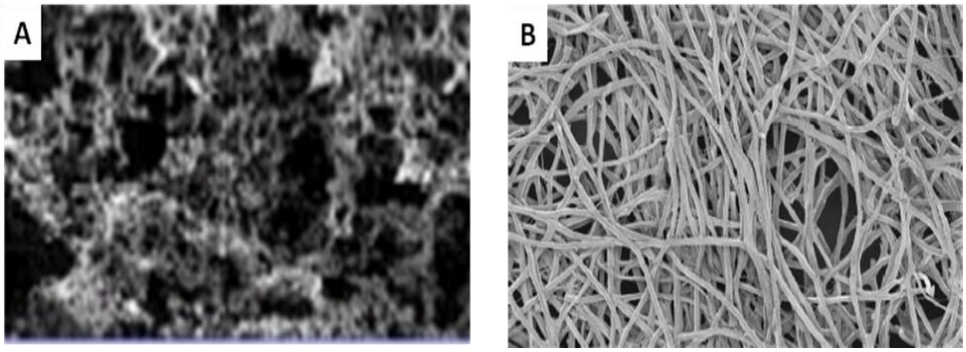

Figure 1.3: Examples of a porous freeze-dried sponge (A) and non-woven mat (B) fabricated structures from aqueous silk fibroin solution, from C. Vepari et al., *Prog. Polym. Sci.*, (2007) 32, 991 (A) and R.E. Unger et al., *Biomaterials*, (2004) 25, 5137.

The novel, all-aqueous processing approach to the fabrication of silk fibroin films has driven recent research to implementation of the material as a biosensor that can be easily characterized and biochemically functionalized. Silk fibroin is a specifically interesting candidate for integration of optical and biological function in a single device and various research has been conducted to this extent.[8,17,19] Characteristic properties of excellent surface quality, transparency, mechanically robust, ease of functionalization, and capacity to form optically relevant morphologies such as nanoscale films have been leading reasons why silk fibroin has drawn so much attention as a novel material for biosensing applications.[8]

1.1.4 Spin-Assisted Layer-by-Layer Assembly

Ultrathin multilayered films have been developed *via* a variety of different processing approaches (i.e. drop casting, Langmuir Blodgett) for utilization in a wide range of applications for the fields of biotechnology, sensors, integrated optics, molecular electronics, and hydrophobic surfaces.[46,47] Specifically, the use of Layer-by-Layer (LbL) has been of particular interest since its introduction by Decher et al. in 1991.[48] The flexibility of the LbL approach allows for material selection from small inorganic particles, proteins, polymers, colloids, and bioactive molecules.[46] LbL assembly is based on alternating deposition of oppositely charged species, and this approach has been applied to integrate synthetic and biological materials with inorganic moieties such as nanoparticles, nanosheets, and nanowires.[49] Utilization of the LbL technique, for formation of polymeric organic and organic-inorganic films, enables incorporation of different organic and inorganic nanoparticles affording increased functionality such as electro-optic and electroluminescent.[4] The added functionality of the overall bionanocomposite, allotted by these different fillers, enables increased control of the overall mechanical stability, and imparts new properties for application as biological templates, microcapsules, microfluidic networks, mechanical and thermal sensors, electroluminescent devices, and optically diffractive components.[5,50]

The LbL assembly process can also be modified by combining the technique with spin-casting through a process known as Spin-Assisted Layer-by-Layer (SA-LbL) assembly.[51] The fundamental difference between the two techniques lies within the adsorption mechanisms at play. In the conventional dip LbL method, polyelectrolyte chains must diffuse towards the substrate, adsorb, and subsequently rearrange at interfaces as well as internally. During SA-LbL, the combination of air shear force and centrifugal force facilitates the kinetics of adsorption for these mechanisms to occur almost simultaneously, thus making the process faster, simpler, and less expensive.[52] Furthermore, SA-LbL assembly provides an opportunity to obtain well-defined and stratified films with tunable thickness, structure and composition at the nanoscale, which cannot be accomplished easily when casting solution mixtures or adding an inorganic component in the conventional LbL approach.[53]

The SA-LbL assembly method was implemented in the studies presented in Chapters II and III because it allows for the production of ultrathin films with greater control over thickness, composition, and properties at the nanometer level.[54,55,56,57,58] Applicability of SA-LbL for designing robust and flexible ultrathin films with excellent mechanical properties has already been demonstrated.[22] Furthermore, the ability to fabricate similar films using the SA-LbL deposition approach in conjunction with reconstituted silk fibroin aqueous solution has been established.[23,30,59] Combination of aqueous silk solution and SA-LbL provides an avenue for fabrication of mechanically robust, flexible, transparent, and biocompatible nanocomposites for biomedical applications such as reinforced tissue engineering. Organized assembly of silk fibroin with clay montmorillonite (MMT) nanoplatelets by way of SA-LbL resulted in nanoscale films (< 120 nm) with increased mechanical properties compared to pristine silk films, while also remaining highly transparent.[59] In the same work, the multifunctional capacity of silk fibroin, effect of inorganic fillers, and broadness of use of the silk solution and SA-LbL approach for use in tailoring properties was exemplified by incorporation of silver nanoplatelets (AgNPLs) leading to a nanoscale film with similar flexibility, but highly reflective optical properties (Figure 1.4).[59] Such a nanocomposite film has potential for use in photonic applications such as optical sensing.

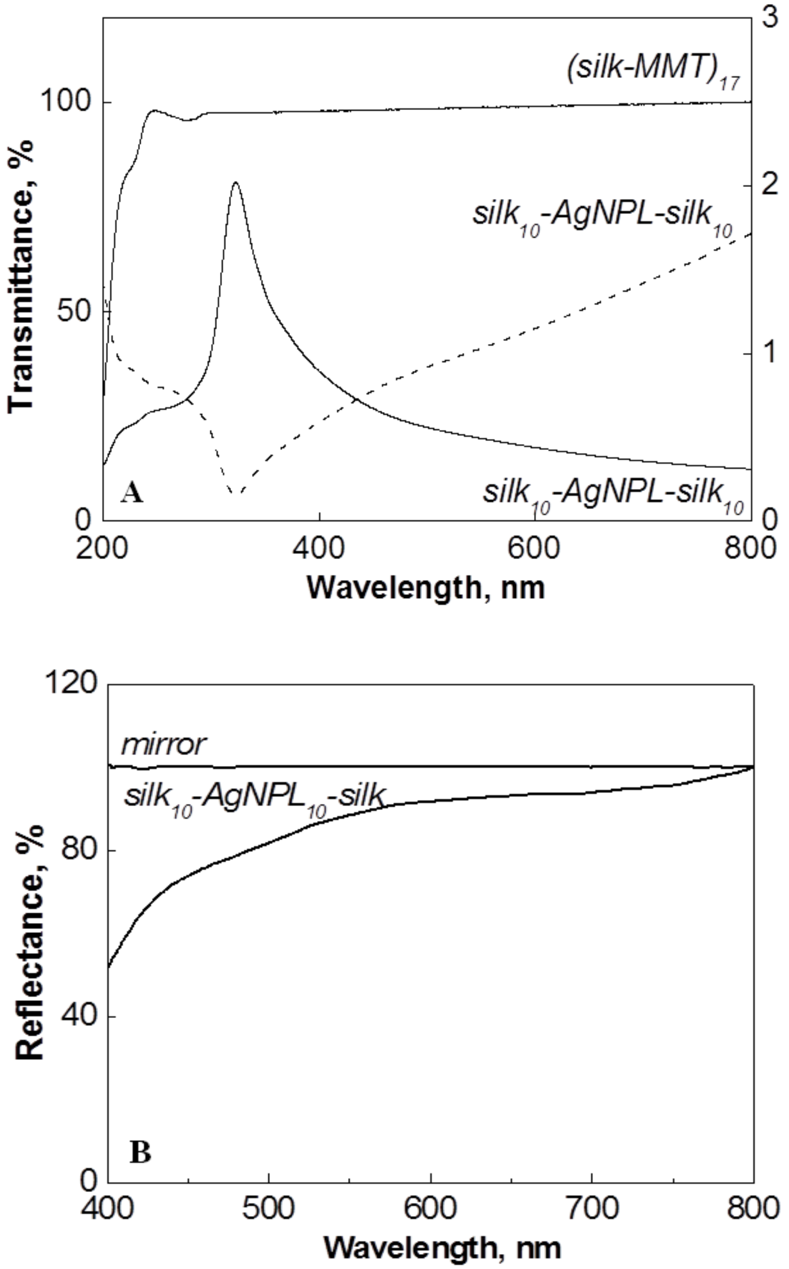

Figure 1.4: UV spectrophotometry transmission of (silk-MMT)$_{17}$ and silk$_{10}$-AgNPL-silk$_{10}$ films (solid lines). The absorbance of the silk$_{10}$-AgNPL-silk$_{10}$ film is shown as a dashed line (A). Reflectance of a silk$_{10}$-AgNPL-silk$_{10}$ film. A common mirror was taken as the reference. From E. Kharlampieva et al., *Adv. Funct. Mater.*, (2010) 20, 840.

1.1.5 Silk Secondary Structures

The unique properties of silk materials are caused by their order-disorder multidomain structure resulting from silk fibroin consisting of alternating hydrophobic and hydrophilic domains. Silk protein is rich in glycine and alanine residues, and the presence of GAGAGS, where G = glycine, A = alanine, and S = serine, amino acid repeats are responsible for the formation of α-helices and β-sheet crystalline regions separated by random coiled segments (Figure 1.5).[60] Silk protein experiences intra- and inter-chain folding during an irreversible transformation, from meta-stable random coil secondary structure (silk I) to silk crystalline ordering (silk II) *via* organized anti-parallel β-sheet structures dominated by hydrophobic amino acids. The β-sheets are crystalline domains providing reinforcement to the silk material through a physically cross-linked structure, thus increasing the strength and toughness.[22]

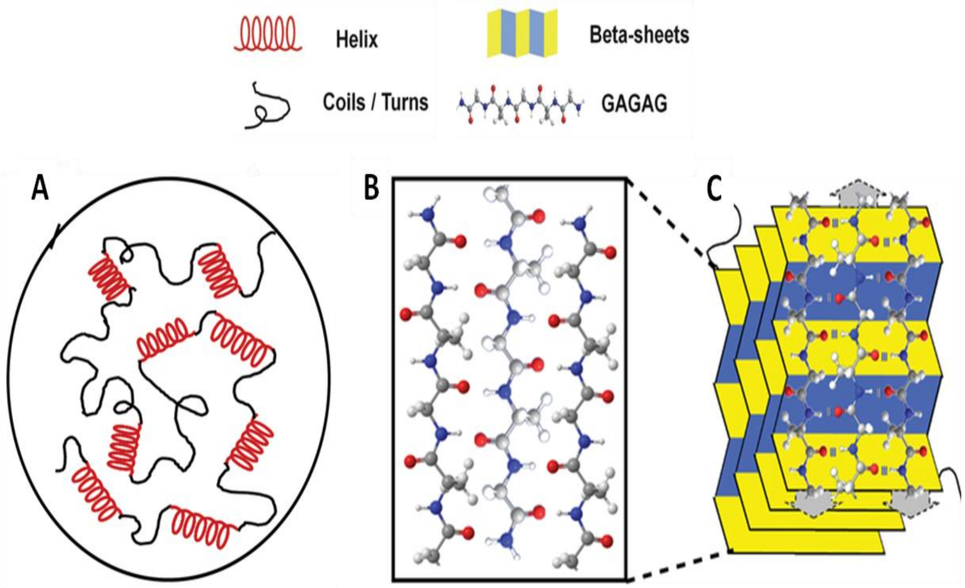

Figure 1.5: Representation of silk I secondary structure with random coils, turns, and α-helices (A), a three-chain silk sequence based on the amino acid hexamer, GAGAGS, with anti-parallel molecular chain axes (B). The chain comprises atoms of carbon (gray), nitrogen (blue), oxygen (red), and hydrogen (white), which have intermolecular hydrogen bonding (represented as three short vertical lines). The molecular chains stack together to form the 3D β-sheet crystals of silk II (C). From P. Cebe et al., *Scientific Reports*, (2013) 3, 1130.

The silk I to silk II transformation can be induced by exposure to heat, organic solvents, dehydration, and mechanical stress.[22,61,62] As more thermal energy is applied into the system, and the temperature is above the transition temperature, the intramolecular hydrogen bonds are broken, thereby, freeing the molecules to rearrange themselves into stable β-sheet secondary structure. As shear force is introduced to silk fibroin solution, the protein strands tend to elongate in the direction of the shear resulting in reduction of the inter- or intramolecular distance so that the β-sheet transition and crystallization becomes facile through formation of strong hydrogen bonds between hydrophobic segments. A cross-linking agent was utilized in Chapter II, and a time-dependency associated with this transition mechanism was discovered (Figure 2.6). Moreover, the use of methanol (MeOH) to induce the dehydration transition mechanism was applied for the study detailed in Chapter IV. Control over the secondary structure of silk films through processing conditions and heat treatment provides a possibility for more organized property assessments to be made.

A balance of assorted forces including van der Waals, electrostatic, entropic, steric, hydrogen bonding, and hydrophobic interactions determines the secondary structure of silk molecules adsorbed at interfaces.[63] Various characterization methods such as osmotic stress[64], intrinsic fluorescence[65], and attenuated total reflection-Fourier-transform infrared spectroscopy (ATR-FTIR)[23] have been employed for investigating and monitoring associated structural changes of silk fibroin. The osmotic stress method provided quantitative results that the silk I structure must contain water of hydration, and utilization of intrinsic fluorescence enabled non-invasive monitoring of silk matrices' secondary structures. Results on *in situ* ATR-FTIR, a surface-sensitive technique allowing for resolution of protein secondary structures in ultrathin films, provided structural characterization in silk films. In Chapter II, the employment of ATR-FTIR was used to increase understanding of silk secondary structures before and after cross-linking.

Although the overall behavior of silk fibroin in solution and in bulk is fairly well understood, secondary silk structures in close proximity to surfaces remain a significant technical challenge. For example, the formation of helical structures at air-liquid interfaces as a polymorph of silk have been reported.[66,67] These studies demonstrated that the crystalline structure, silk III, involves a left-handed, threefold helical chain secondary structure with hexagonal packing of silk molecules. Side chain character influences the stabilization of an interfacial structure, suggesting that hydrophobic/hydrophilic interactions and partitioning drive the silk conformation at the air-liquid interface. Investigation of silk secondary structures in relation to their proximity to different interfaces is detailed in Chapter III.

1.1.6 Surface Patterning

The increasing need for multifunctional high-performance organic materials has spurred research focused on development of the ability to spatiotemporally pattern and control the structure of organic templates, resulting in enhanced management of the functional properties of bionanocomposites. When designing bionanocomposites, the control of spatial distribution and the rate of nucleation and growth of different entities (i.e. biomolecules, inorganic moieties) are important factors due to the dependence on functional coupling of these composite additives to the surface. Patterning of organic surfaces to provide nanoscale features enhances the degree of control over those factors, increases the total surface area, and provides dimensional similarity between the additive entities and the organic scaffold. This enhanced control of functional properties also allows for preferential attachment of cells for use as a cellular scaffold[11], or attachment of biological entities for biosensor applications.[8]

Several fabrication methods have been implemented in patterning films, including simple solution-casting, dip-casting, spin-casting, SA-LbL, self-assembled monolayer formation, Langmuir-Blodgett film formation, spraying, electrochemical deposition, photolithography, and soft lithography.[68,69] The range of templating methods provides the ability to manipulate the function of singular films, as well as enabling creation of complex composite structures with a hierarchy of function and order.[4] The patterning of organic surfaces provides a pathway for the controlled tunability of desired material properties in two-dimensions (2D) and three-dimensions (3D), principally for applications in the fields of optics, biosensing, and bioengineering, where surface-to-volume ratio plays an integral role.[19] The novel, all-aqueous processing approach to the fabrication of silk fibroin films has driven recent research to implementation of the material as a biosensor that can be easily characterized and biochemically functionalized. Biosensors can be utilized to detect the presence of biological entities (molecules, cells, pathogens, toxins, etc.) and a key operation in a biosensor is to attach these entities to the surface of the sensor, which can be accomplished through functionalization of the surface. For example, the incorporation of optics within a biosensor has been conceptualized previously through ordered molecular surface arrays for use as a fluorescent pH sensor.[70] In this example, sensor patterning led to increased sensitivity to variations in pH due to contrast between functionalized and non-functionalized areas, thus demonstrating the usefulness of nanopatterning biosensors.

In particular, silk fibroin has created a surge of research interest for use as a patterned organic material due to its optical transparency, biocompatibility, biodegradability, ease of functionalization, and excellent physical properties.[9,11,39,41,42,45] The topography of silk patterned films is of key interest, since the focal point concerns the effect on material properties after the introduction of a surface array. Engineered surfaces enable tailoring of material properties, such as adhesion, elasticity, hydrophobicity, and refractivity. Control and design of nanostructured surface patterning allows for the formation of silk-based optically diffractive devices such as diffraction gratings, pattern generators, and lenses constructed through 3D micropatterning and casting of silk fibroin solution.[8,9]. Optical waveguides to manipulate and transport light in a controlled manner have also been constructed with silk[71], and the consistent transverse dimensions, lack of discontinuities, and smoothness of the silk waveguides contributed to their facile ability to guide light. Silk fibroin is a specifically interesting candidate for integration of optical and biological function in a single device and various research has been conducted to this extent.[8,9,17]

Recently, an area of research has emerged involving the sensing of blood glucose, an important analyte for diabetic healthcare. Immobilization of glucose oxidase and peroxidase in silk fibroin membranes has proven to be a novel approach for sensing of blood glucose concentrations.[18,19,20] Moreover, the entrapment of enzymes, void of the presence of harmful cross-linking chemicals, was demonstrated to be useful in maintaining the enzymes' desired activity.[19] Peroxidase enzyme immobilization during fabrication of silk diffraction gratings was shown as a route to retain activity of entrained molecules, while providing added functionality and selectivity to optically active silk films.[8] Periodically nanopatterned lattices on silk-based films have been developed to generate spectral signatures as a function of the lattice spacing used on the film surface.[17] These films were implemented within a colorimetric sensor functioning on the photonic crystal lattices which created different wavelength signatures for detection of glucose concentration (Figure 1.6). The patterned optical surfaces for manipulation of light within a biological matrix provided an integrative approach for application in probing biological function.

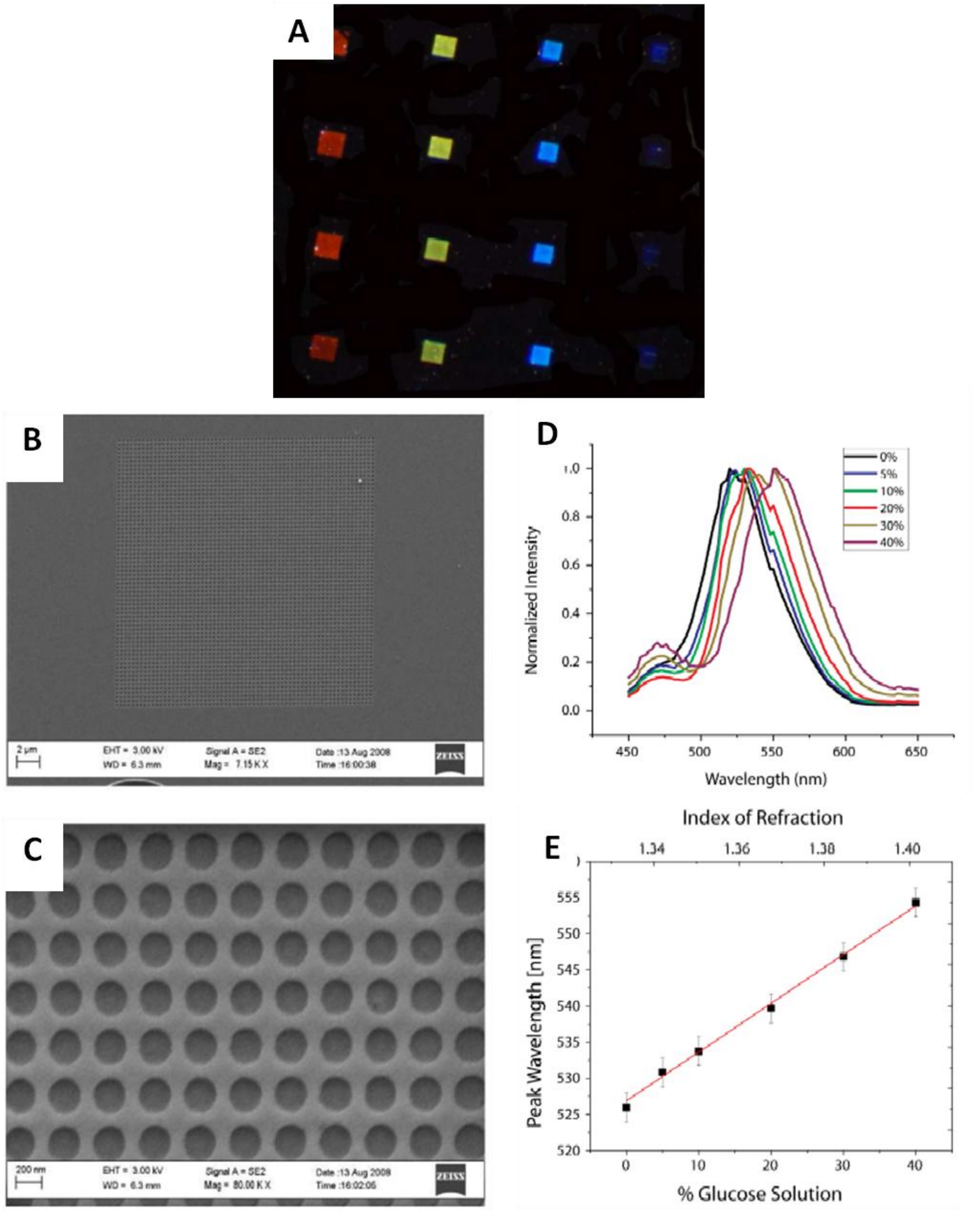

Figure 1.6: Periodic nanoholes in silk illuminated with light from a dark-field condenser (A). The lattice constants are from left to right 700, 600, 500, and 400 nm. The distance between the rows of colored squares is 200 μm. SEM images of periodic nanoholes in silk (B & C). The nanoholes are 200 nm in diameter, 30 nm deep and separated by 300 nm. Spectra of the 400 nm lattice constant structure illuminated with supercontinuum with different concentrations of glucose (D) and plot of the peak intensity vs. glucose concentration and index of refraction (E). From J. Amsden et al., *Optics Express*, (2009) 17, 21271.

Biomaterial design is a crucial element in the field of bioengineering, and patterned biomaterials with localized variability in surface chemistry, physical features, and degradation properties allows for incorporation of chemical, physical, and biological cues to enhance flexibility in controlling the adhesion, growth, shape, orientation, and gene expression of adherent cells.[10,42,72] Associated applications include cell culture substrates for cell adhesion, tissue engineering scaffolds with biocompatible and biodegradable properties, drug delivery, and cell patterning.[73] This flexibility is of specific interest for fabrication of cellular scaffolds, in which a given cell population is seeded, proliferated, and differentiated with the introduction of functional cell types.[74] The non-immunogenicity of aqueous silk solution allows for its utilization in biomaterials for wound dressings, tissue repair material, and artificial skin.[43]

One interesting application of patterned silk biomaterials exists due to their inherent optical clarity providing a new pathway to produce valuable surfaces for directing cellular function and matrix deposition, while harmonizing both mechanical and optical functional needs for corneal tissue engineering.[11] Cell alignment on patterned silk films occurred through contact guidance producing aligned cellular matrices, while remaining robust and transparent to support native tissue regeneration. The alignment of cells on these circular, grooved surfaces provides an example of how cell alignment is influenced by the silk film topography (Figure 1.7).[11] In another study, fibroblasts appeared to have different morphology on a patterned surface, with nanoscale pillars acting as physical barriers restraining cells from spreading, guiding cell migration in unusual directions, and eventually changing their shape.[75] This behavior is in contrast to cells on non-patterned, planar films which do not display any preferential orientation.[42] A possible explanation for this cellular growth trend is due to alignment of cells being energetically preferential along the grooves of the pattern rather than having to cross over the pattern boundaries which requires displacement over a greater distance. The variations in the orientation, migration, and shape of the cells on these pillars were evident, and depended closely on the height of the pillars. Fabrication of silk-based films with similar features as the aforementioned examples is demonstrated in Chapter IV.

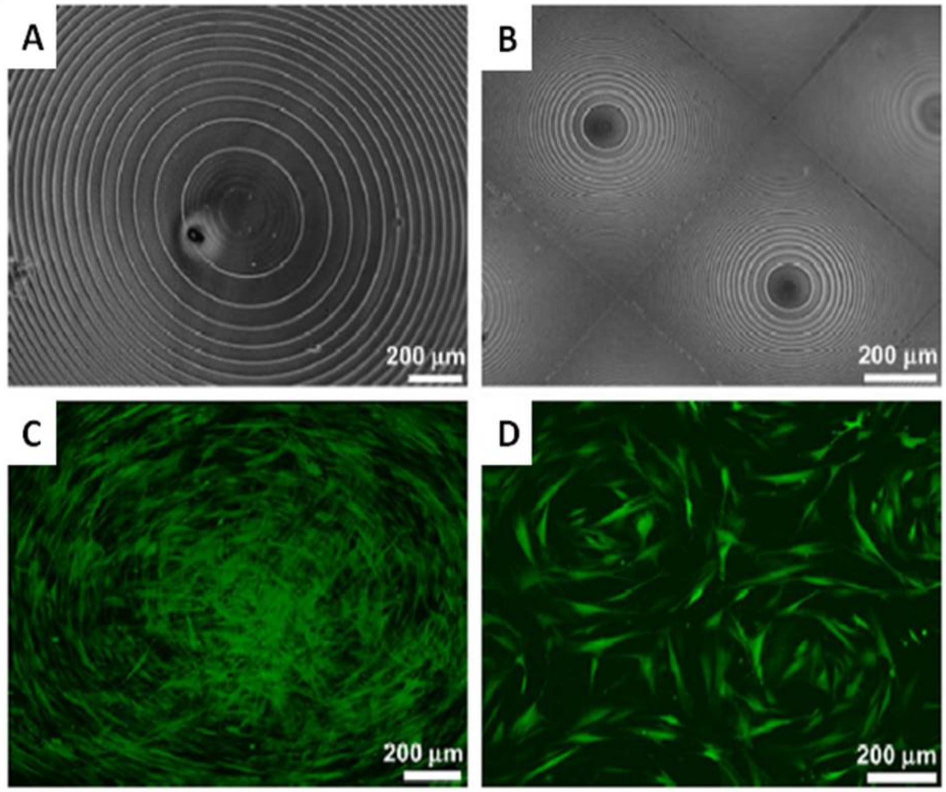

Figure 1.7: Phase contrast image of 1 cm diameter (A) and multiple 700 µm diameter concentric circle silk film patterns (B). Fluorescent images of GFP-rCFs seeded on respective concentric film patterns at day 4 in culture (C & D). From B. D. Lawrence et al., *Biomaterials*, (2009) 30, 1299.

1.1.7 Biomineralization

Biomineralization can be described as the utilization of proteins containing several moieties affording covalent functionalization with biological molecules, or to conduct reduction of inorganic nanoparticles.[72] Found in nature, biomineralization occurs through either a biologically induced route, or by boundary organized biomineralization. The biologically induced route to mineralization more closely relates to organic and inorganic material interaction occurring within the bulk of a mixture and facilitates the precipitation of mineral phases. On the other hand, the boundary organized route develops inorganic particles on the surface of an organic template *via* functional surface interaction, providing preferential sites for nucleation and growth. Increased control over the size, morphology, and crystallographic orientation of the mineralized particles is a distinct advantage of the boundary organized mechanism.[76]

The employment of biomolecules as templates for the synthesis of inorganic nanoparticles has the potential to enable precise control over these particles' size, aggregation state, and spatial arrangement, and has attracted interest for research areas in bioengineering and materials science with prospective application in photonic devices, chemical and biosensor arrays, and other optical systems.[12,29] Organized deposition of inorganic particles can be achieved with biomolecules utilized for the control of nucleation and growth through entrapment, immobilization, or reduction of the inorganic nanoparticles at the surface of the biomolecular template, thus forming an organic-inorganic surface. Utilization of an active layer for nanoparticle reduction and direct growth of the inorganic phase, enables modification of surface functionality for tailoring optical properties, reactivity, mechanical strength, hydrophobicity, biocompatibility, sensing ability, and photovoltaic capability.[4,77,78] Such organic-inorganic nanocomposites can be designed either by adding inorganic nanofillers during fabrication of organic matrices (Chapter II), or by making use of the active biological molecules with proper functionalities which support the reduction of inorganic compounds directly from solution onto the surface (Chapter IV).[77]

One type of nanoparticle of specific interest is TiO_2 due to the associated broadness of applicability as photocatalyst, UV blocker, material for solar cells, and oxygen sensor.[79] It has been recently shown that these TiO_2 nanoparticles can be confined in a uniform and disperse manner within nanoscale protein surface domains.[29] The confinement then limits the nanoparticle growth to a critical radius dependent on the area of the domain, and prevents the formation of larger aggregates. The approach provided regulated growth of the TiO_2 nanoparticles, thus opening control over the dimensions and surface distribution, and demonstrating a pathway for incorporation of a variety of other similar nanoparticles.

Similar to surface patterning, recent research has uncovered silk fibroin as a leading biomolecular template candidate for implementation of bioenabled surface mineralization of nanoparticles, based on several properties of silk protein including biocompatibility, biodegradability, transparency, outstanding mechanical properties, and ease of functionalization.[37,39] Creation of silk-based architectures with patterned surfaces enables tailored control of adsorption, and directs nanoparticle nucleation, growth and organization.[29] The silk fibroin surface or structure can be used for deposition of a variety of inorganic nanoparticles, allowing for increased tunability of the surface properties and enhanced functionality of the overall composite. A recent study has been conducted regarding to the bioassisted growth of gold nanoparticles (GNPs) onto silk matrices[23], and the study outlined in Chapter IV employs a similar approach.

1.2 Reasoning for Tests

Despite significant progress in designing silk-based bionanocomposites, many challenges remain in synthesis of bioenabled and bioderived multifunctional materials with well-organized structure, homogenous composition and distribution of nanofillers, and nanoscale control over film thickness for ultrathin (below 200 nm) films. The ability to precisely construct silk-based architectures at the nanoscale could provide a means for producing biocompatible and biodegradable nanomaterials for advanced applications with requirements of miniaturization, lightweight, excellent toughness and flexibility, and optical functionality. Control over the uniformity of microstructure and properties, robust mechanical behavior, fast and energy efficient fabrication procedures in ambient conditions, and facile system integration are issues that, once resolved, will greatly increase the potential application of silk-based bionanocomposites.

1.2.1 Integration of Processing Approaches & Effect of Different Fillers

The evaluative comparison of conventional SA-LbL deposition of alternating layers comprised of different materials versus a one-step mixed solution route, demonstrated in the Chapter II studies, could provide a unique opportunity to overcome major obstacles for developing high-performance silk-based nanocomposites. Premixing of components combined with silk cross-linking affords improved solubility and compatibility of the silk and inorganic materials and, therefore, a more homogeneous materials deposition in a single step. The latter issue is a significant challenge in traditional SA-LbL assembly with alternating deposition of silk and inorganic nanostructures.[59] At the same time, the one-step one-solution approach holds advantages over the traditional SA-LbL such as a nanoscale control over deposition into hierarchical structures and scaling up to higher film thicknesses. Thus, in contrast to previous studies on organic-inorganic composites fabricated by conventional SA-LbL assembly or casting solution mixtures[53], the integration of approaches might afford a higher degree of materials uniformity and enhanced physical properties. These prospective products will be critical for designing ultrathin biocompatible nanocomposites with advanced mechanical properties for potential applications in biomedical science such as biosensors and selective membranes.

1.2.2 Interfacial Configuration & Silk Structural Conformation

The lack of knowledge about secondary structure and properties of ultrathin silk films at interfaces (both silk-silk and silk-inorganic) can be mostly attributed to experimental difficulties in probing secondary structures for nanometer thick films. Neutron reflectivity (NR) measurements, as a route to overcome these difficulties, were conducted to investigate details regarding the internal structure of SA-LbL deposited silk films in the direction perpendicular to the surface, as reviewed in Chapter III. For comparison, a $(\text{silk})_1$ monolayer film as well as a $(\text{silk})_7$ multilayer film were prepared and tested in both a dry-state and a swollen-state in heavy water (D_2O). The fundamental understanding of the self-assembly process of silk and other biological macromolecules is still uncertain, and investigation of the intermolecular interactions and structural changes associated with intimate contact with an inorganic surface is required to gain insight into these processes.

In a recent study, ATR-FTIR spectroscopy of silk on silicon substrates was conducted and revealed that spin-assisted deposition immediately induced crystalline silk II from silk I secondary structure (random coil) in ultrathin films.[23] This transformation is believed to be facilitated *via* exposure of the ultrathin silk layer (~ 5 nm) to air in combination with shear forces, causing rapid dehydration of the film. Depiction of the subjected effects of spin-coating during silk layering is shown in Chapter III (Figure 3.1). In contrast, a relatively thick (~ 100 nm) dry spin-cast film displayed a predominantly random coil structure under ambient conditions.[21] The result is indicative of different structures pertaining to the ultrathin film versus the thicker one, and the occurrence of significantly segregated interfacial structures. X-ray investigation of the silk II structure has been reported[80], and conclusions were drawn that the fibroin structure possesses a twofold screw axis. Also from this evidence, it was suggested that the space group for silk II is $P22_12_1$ and the unit cell is orthorhombic with lattice parameters of $a = 9.29$, $b = 9.44$, $c = 6.95$ Ǻ.[80] However, these studies provide only information on average microstructure of silk molecules in particular films and cannot address the question of localized and propagating segregated phenomena and the effect of the interfacial confinement along the surface normal. Information is still lacking regarding how increasing distance from the interface affects the silk chain conformation. The importance of the side chain character is noted and can be employed as a determinant for secondary structure at different interfaces. Furthermore, the behavior of silk films in liquids, as well as their ability to swell after tethering to interfaces, remains uncharted.

1.2.3 Nanopatterned Surfaces & Surface Mineralization

Selective nanopatterning of various, and sometimes multiple, components on the surface of an organic material has been a challenge for patterned templates. Bionanocomposites consist of a broad range of component materials, unlike most traditional thin films, thus displaying the need for a versatile fabrication approach as critical to successful implementation. Moreover, the cost of processing such composites needs to be kept low for maintaining the attractiveness of the chosen approach, while the approach must also be amenable with existing technologies. Photolithography has been the traditional method for patterning surfaces; however, adding an inorganic component to the precursor or adsorbing the inorganic material onto fabricated structures is not readily applicable due to interference with photopolymerization, capillary-induced collapse, and clogging of nanoscale pores.[81] Also, photolithographic chemistries are often harsh and toxic which restricts the use of biological macromolecules. Even though 2D and 3D composite nanostructures based on silk fibroin have been developed, the full potential for novel mechanical, optical, biodegradable, and biocompatible properties has not been attained.[73]

The major challenge associated with boundary organized biomineralization of inorganic particles is precise control of adsorption, stability, and resulting interfacial structure. The adsorption process is key to successful biomineralization, and can be affected by protein hydrophobicity, surface chemistry, hydration states, non-covalent interactions, and conformation of polymer chains.[82] Another challenge related to biomineralization with silk templates includes the need for increased understanding of the roles of silk protein's interfacial structure, assembly conditions in silk secondary structure transition, and main amino acid groups present at the surface for silk I and silk II.[82] Lack of understanding of many systems of interest, including the detailed role of interfaces between organic templates and inorganic components, failure mechanisms, and new strategies to control interactions currently inhibit widespread utilization of silk biomineralization.[12] In order for the challenge of homogeneously nanostructured materials synthesized with biological templates to be overcome, control over silk secondary structure and interfaces and its effect on reduction of inorganic particles is required.

Formation of silk fibroin films with precisely controlled 2D or 3D nanopatterns, comprised of sub-30 nm transverse features, have been demonstrated through utilization of a soft lithography-based, simple-casting technique at ambient conditions from an aqueous silk solution.[5,9] Some of the benefits associated with this technique include broadening the variety of fabricated patterns, precise lateral and vertical molecular design of nanostructural composites, simplicity, and absence of harsh chemicals, salts, or high pressures typically related to other nanofabrication methods. In spite of the goals reached with the LbL method for differentiating layered structures along the surface normal, fabrication of differentiated laterally patterned structures has become a major limitation.[47] One of the soft lithography approaches implemented in Chapter IV, micro-transfer printing, involves the construction of a deposited film onto an elastomeric "stamp", and its complete transfer to the surface of a different substrate. Utilization of an elastomeric stamp provides the advantage of strong adhesive interactions and conformal nature for patterning of polymer films to achieve mechanically stable arrays. Control of adhesive interactions between the deposited layer and the stamp, as well as polyions at the interface of the stamp and at the interface of the desired substrate, are important factors for successful implementation of this approach.[4]

Fundamental studies of these factors and how to enact control through ionic strength, pH, and regulation of Van der Waals' interactions will increase understanding needed for enabling the construction of devices with specifically patterned surfaces for applications in optics, biosensing, and bioengineering.[83] These applications require finely tuned surfaces and interfaces for control of adhesion, elasticity, friction, chemical, and optical properties, and will likely benefit from augmented development of nanoscale patterning.[73,83] Combining the ability to tailor the composition of nanostructured materials with inexpensive patterning routes through printing, molding, and templating could present a key pathway to commercialization.[4] Therefore, a fabrication route to achieving patterned silk films as an organic template utilized for further tailoring of functional properties *via* biomineralization of GNPs was explored in Chapter IV. Detailing of research on this area is critical for developing knowledge on silk interfacial behavior, and will provide important information relating to the design of novel bionanocomposites uniting valuable characteristics of silk with those of the nanoparticles.

1.3 General Conclusions

The basic properties and behavior of materials at the bulk scale have been widely investigated throughout the history of scientific research; however, fundamental study of how these same materials behave at the nanoscale has been enacted only within the past several decades. Such study is intriguing and paramount to advancement of composite properties due to the unique catalytic, electrical, and optical properties of nanomaterials, provided from their high surface to volume ratio, allowing for development of nanocomposites with novel characteristics and multifunctional capacity.[3] Analysis of biological structures and systems found in nature has demonstrated the value of nanoscale features, which in turn, has led to the incorporation of nanomaterials for biocomposite fabrication.[72] Biocomposites have great potential in bioengineering, optics, and sensing applications, but often lack the necessary mechanical robustness for these demanding applications. The mechanical strength of biomaterials can be enhanced *via* traditional cross-linking of polymer chains, or through addition of various nanomaterials. Silk fibroin protein is an attractive biomaterial for implementation as a matrix in hybrid bionanocomposites due to favorable biological and optical properties, ease of processing in aqueous solutions, ability for fabrication into a myriad of various geometries, and capability to self-assemble into more mechanically robust β-sheets.[10,11] Although native silk fibers are known as one of the strongest natural fibers, engineered analogs possessing broader application in biologically related fields have inferior modulus, toughness, and elongation. The key factor attributing to this discrepancy is the removal of sericin, a glue-like glycoprotein that provides mechanical strength at the cost of immunogenic and inflammatory responses.[39] For these reasons, inorganic nanofillers are often utilized with a silk solution fabrication approach to reinforce and provide additional functionality to silk-based bionanocomposites.[24,25]

While most studies on silk-based composites have primarily focused on characterization of structures at the microscale, the studies detailed in this work are completed at the nanoscale to fill the need for structural characterization of silk-based composites at multiple scales of dimensions. Utilization of AFM, SEM, NR, etc. enabled for multiscale characterization for generation of data helpful for successful multiscale fabrication, enabling control of silk secondary structure and hierarchical arrangement of nanofillers. Confinement and environmental effects were also investigated to supplement needed development of material modeling and a universal fabrication approach with known effects of chemicals and solvents on resulting structural formation and properties. MMT and POSS nanofillers were integrated for reinforcement of silk membrane nanostructure. Investigating the relationships between the selected nanofillers and the silk matrix, involved in the resulting composite properties, will assist in fabrication of hybrid bionanocomposites exhibiting novel synergistic properties based on the individual features of the respective constituents.

Focus of the studies detailed in Chapters II, III, and IV was on silk-inorganic interfaces, and includes the fabrication of silk-based nanocomposites in a variety of designs for characterization of interfacial phenomena associated with synthetic nanostructures and natural matrices. Enhanced interfacial strength is a critical factor in achieving synergetic properties of advanced performance nanocomposites with reinforcing nanofillers for both enhanced robustness and added functionality. Nanofiller shape, dimensions, and surface chemistry are important characteristics for selective incorporation as composite materials, and detailed knowledge of how structure can be controlled is also critical for fabrication of desired hierarchical physical properties of the overall bionanocomposite. Mechanical, optical, and swelling properties were investigated for increased understanding of how the interaction between nanofillers and silk matrix affect physical properties of silk-based nanocomposites. Furthermore, investigation of silk-inorganic interfaces will provide understanding of how interactions between silk and inorganic particles is affected by initial silk secondary structure, and how silk secondary structure is affected by deposition conditions.

The resulting properties of bionanocomposites are not only dependent on the type of nanofiller and its interaction with the surrounding matrix, but also on the chosen assembly techniques and conditions. Therefore, comparison of conventional LbL assembly with a novel one-step mixed solution assembly technique was accomplished to fill a current research gap related to enhanced control over the deposition of hierarchical structures for achievement of a higher degree of materials uniformity and augmented mechanical properties. The novel assembly technique may provide a pathway to overcome major challenges for bionanocomposites, such as development of highly homogenous films with precisely designed morphology, structure, and composition at the nanoscale. More specifically, GA cross-linking agent was added in the mixed solution resulting in a previously unrealized structural control afforded by a combination of cross-links and beta-sheets. The transition from amorphous silk I to silk II crystalline ordering *via* known routes such as exposure to heat, organic solvents, dehydration, and mechanical stress has been well documented[22,61,62]; however, a new route for obtaining silk II bionanocomposites was demonstrated without the need for post-deposition treatment. Traditional techniques for fabrication of hybrid bionanocomposites are limited by precise control of secondary structure, interfacial effects, and overall structural organization. Novel approaches have potential to afford nanomaterials with tailored composition, enhanced interfacial strength, and tunable thickness at the nanoscale.

Lack of detailed understanding of the mechanism involved with formation of silk-inorganic interfaces was addressed by probing the secondary structures for nanometer thick films *via* neutron reflectivity, in Chapter III. The arrangement of protein chains is a critical factor for nanoscale control over molecular organization during fabrication of hybrid bionanocomposites, and is not well understood. Although ATR-FTIR and X-ray analysis of silk-based nanoscale films has been conducted and provides information on compositional changes[23], neither analytical method can address the questions of localized and propagating segregated phenomena. Neutron reflectivity measurements were implemented to afford investigation of details regarding to the internal structure of films in the direction perpendicular to the surface, and moreover, enables charting of the behavior of silk films in liquids and their ability to swell after tethering to an inorganic interface. An encompassing theme of the studies reported is focused on understanding of silk secondary structures: before and after cross-linking, in close proximity to inorganic surfaces, and effect on structural features after rearrangement of protein chains.

Soft lithography based replica molding via micromolding in capillaries was utilized to design micropatterns from hybrid nanomaterials, and demonstrated the broad range of possibilities for fabrication of silk-based functional structures with low cost of processing and absence of harsh chemicals that usually limit the use of biomaterials during conventional nanocomposite fabrication techniques such as photolithography. The chosen fabrication technique could provide a route for laterally differentiated patterned structures with specific and localized control of properties, valuable for numerous sensing, bioengineering, and optical applications, and has been a major challenge for nanocomposites. Introduction of nanopatterned features could increase the control of desired properties, and allows for addressing the role of interfacial confinement effects on assembly behavior, morphology, and dynamics of protein chains. Further probing of the fabricated templates for *in-situ* growth of metal nanoparticles in a patterned manner was implemented to afford simplicity and versatility based on a predesigned matrix.

The control of structural organization of proteins, internally and at interfaces with inorganic materials, is crucially important for the design of bionanocomposite materials, and the studies detailed in this paper will increase understanding needed for construction of silk-based materials and devices with specific properties for applications in optics, biosensing, and bioengineering. These studies aim to further develop a further develop a fundamental understanding of silk interfacial phenomena and importance of silk secondary structure, and to introduce novel design strategies for silk-based bionanocomposites.

CHAPTER II

CO-CROSS-LINKING SILK MATRICES WITH SILICA NANOSTRUCTURES FOR ROBUST ULTRATHIN NANOCOMPOSITES

2.1 Introduction

In this study, a novel assembly approach is introduced for bottom-up fabrication of ultrathin, robust, freely standing, silk-based nanocomposite membranes with significantly enhanced mechanical properties. One of the most popular inorganic reinforcing components for polymer and natural nanocomposites is clay platelets (Figure 2.1A) because of their outstanding mechanical values, high surface area, high aspect ratio, and compatibility with polymeric materials.[84,85] Incorporation of clay nanoplatelets by either blending or by LbL assembly resulted in clay-organic nanocomposites with significantly enhanced thermal and mechanical properties and reduced permeability.[86] It has recently been shown that reinforced silk-clay nanocomposite films can be obtained by SA-LbL assembly of a silk fibroin matrix with clay MMT nanosheets.[59] The silk-clay nanocomposites exhibited significantly higher toughness and Young's modulus then those of pristine LbL silk membranes studied in previous work.[22]

Another promising candidate for multifunctional and lightweight nanocomposites is polyhedral oligomeric silsequioxane (POSS) nanoparticles (Figure 2.1). Introduced as a new functionalized inorganic compound, POSS has attracted interest because of its facile preparation, low polydispersity, high transparency, high yield, and multiple functionalities. Moreover, POSS is inert, optically transparent, and stiff, with the Young's modulus reaching 7.5 GPa.[87] Moreover, it is a low-cost and easily scalable material if a one-pot synthetic route is used to create modestly polydispersive POSS. The POSS material has several unique features: (1) the chemical composition is a hybrid, intermediate ($RSiO_{1.5}$) between that of SiO_2 and silicone (R_2SiO) and (2) the POSS nanoparticles (2-4 nm) are comparable to common polymer dimensions and domains in silk materials.[88] Therefore, POSS has an organic-inorganic core structure, which provides rigidity while covalently bonded reactive functionalities make POSS compatible with interfaces.[89] As a result, the POSS compound has served as a reinforcing agent for polymer matrices, resulting in improved bulk thermal and mechanical properties.[90,91] The reinforced nanomaterials were obtained by integrating POSS nanoparticles and MMT nanoplatelets with silk matrices which were premixed with glutaraldehyde (GA) as a cross-linking agent to increase matrix and interfacial strength. To achieve this goal, a novel one-step fabrication approach is introduced which involved step-by-step spin-assisted deposition of the three-component mixture of silk, cross-linking agent, and a nanofiller, and compared the results with conventional SA-LbL assembly which is usually employed for the fabrication of laminated nanocomposites.

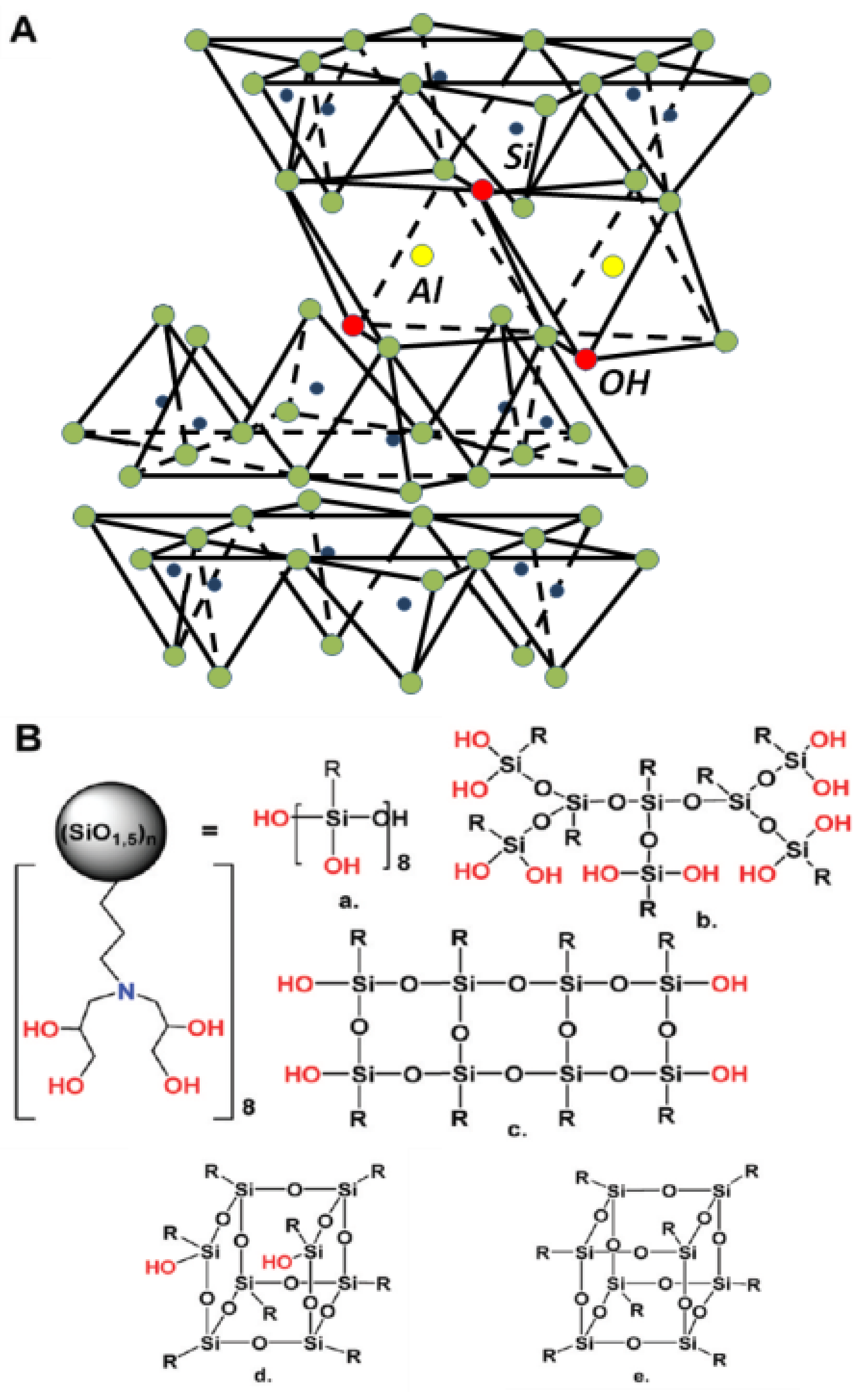

Figure 2.1: Schematic presentation of MMT (A) and POSS structures (B). POSS is presented as a mixture of linear (a), branched (b), ladder-type (c), incompletely condensed polyhedral (d), and completely polyhedral structures (octahedral as an example) (e). The MMT structure A is redrawn from http://serc.carleton.edu/NAGTWorkshops/mineralogy/clay_mineralogy.html.

2.2 Results and Discussion

2.2.1 Nanocomposite Assembly

MMT clay exploited in this study belongs to the class of 2:1 phyllosilicates, nominally one-dimensional crystals comprising covalently bonded, aluminosilicate layers, ~0.96 nm thick and separated by a van der Waal interlayer, gallery containing charge-compensating alkali metal or earth cations (Figure 2.1A).[92] The charge per unit cell (generally between 0.5 and 1.3 for swellable smectites) originates from isomorphous substitution within the aluminosilicate layer (*e.g.*, tetrahedral Si^{4+} by Al^{3+} or octahedral Al^{3+} by Mg^{2+}). The number of exchangeable interlayer cations, the cation exchange capacity (CEC), generally ranges between 60 and 140 mequiv/100 g. Cloisite Na has a nominal unit cell formula of $Na_{0.66[}Si_{7.8}Al_{0.2}O_{16}][Al_{2.96}Fe_{0.45}Mg_{0.44}Ca_{0.02}O_4(OH)_4]$ and a CEC of 95 mequiv/100 g.[92]

POSS used in the study has different compositions of hydroxyl and tert-amine groups at their peripherals as illustrated in Figure 2.1B. POSS has an empirical formula of $[RSiO_{1.5}]_n$ (where n = ~14 and R represents organic functional group $CH_2CH_2CH_2N[CH_2CH(OH)\text{-}CH_2OH]_2$) and is composed of a mixture of linear, branched, ladder-type, completely polyhedra, and incompletely condensed polyhedra structures. Nanoparticles are very uniform in size and have average dimensions of 2.5 nm.[89] Moreover, each POSS molecule contains a reactive organic shell for solubility and compatibility of the POSS segments with the various matrices.

It was found that traditional SA-LbL assembly of silk and POSS resulted in linearly grown (silk-POSS)$_n$ nanocomposite films with a bilayer thickness of 4.2 nm (Figure 2.2). The result correlates well with the bilayer thickness for silk-MMT films.[59]

Further exposure of the (silk-POSS)$_n$ and (silk-MMT)$_n$ matrices to GA solutions resulted in no change in film thicknesses. In contrast to the traditional method of SA-LbL deposition of different components, the one-step approach involved premixing silk and GA solutions followed by adding nanofiller dispersions (Figure 2.3). Indeed, both three-component films of (silk + GA + POSS) and (silk + GA + MMT) showed linear growth, indicating persistent and robust assemblies, similar to the two-component silk-POSS and silk-MMT systems. However, the (silk + GA + MMT) system possessed an increment 5.35 nm per layer which is thicker than that for a (silk-MMT) film of 4.1 nm/bilayer. The (silk + GA + MMT) nanocomposites exhibited similar linear growth with the layer thickness of 4.7 nm. The control experiment with a (silk + GA) film demonstrated that films of pre-cross-linked silk were thicker than those for the non-cross-linked one-component (silk) films showing layer thicknesses of 4.5 and 3.9 nm, respectively (Figure 2.2).

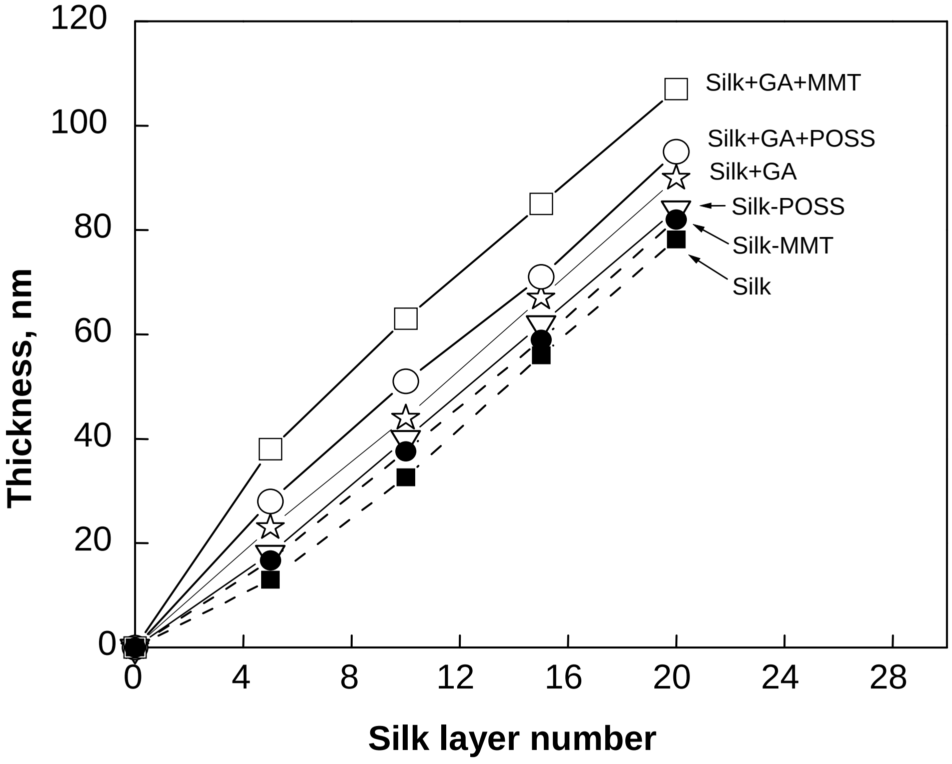

Figure 2.2: An increase in thickness of different silk SA-LbL films with increasing numbers of deposited layers as measured by ellipsometry.

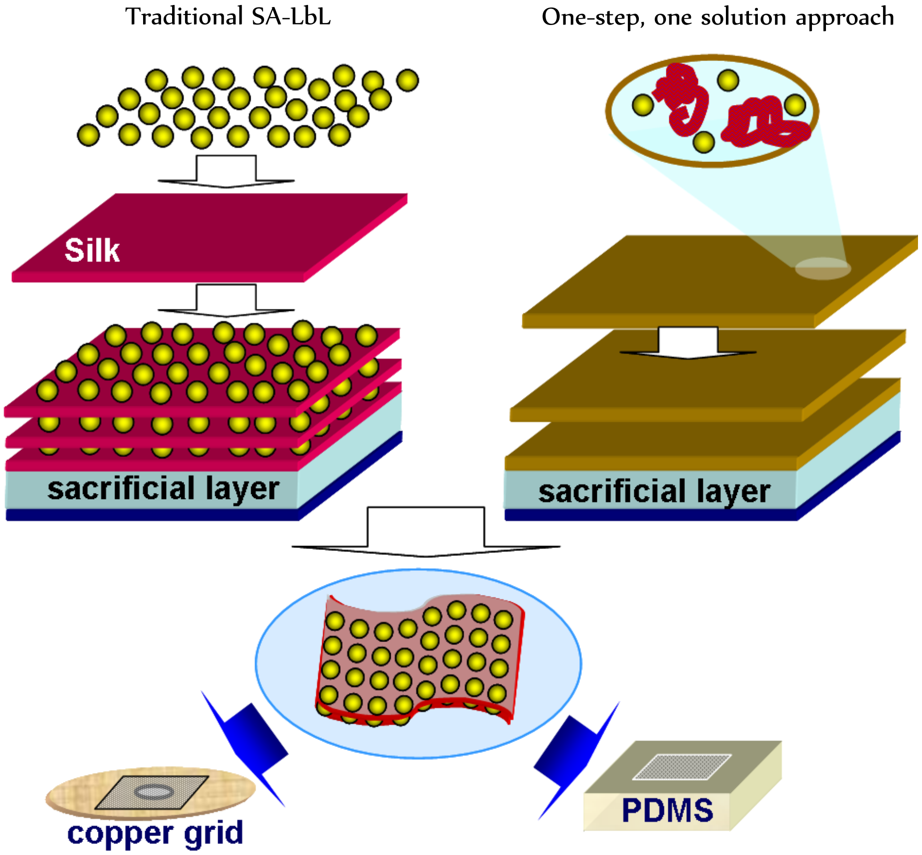

Figure 2.3: Representation of two SA-LbL approaches for the fabrication of reinforced silk nanocomposites: traditional SA-LbL assembly (left) and one-step, one-solution SA-LbL approach (right).

2.2.2 Surface Morphology

Figure 2.4 presents atomic force microscopy (AFM) topographical images of a single-layer silk film and a (silk + GA) film deposited from non-cross-linked and pre-cross-linked silk, respectively. AFM analysis of the images showed that both films have light-grainy morphology with a surface microroughness (RMS) of 1.3 ± 0.2 nm and 1.2 ± 0.2 nm (within 1 X 1 μm^2 surface area) for the silk and (silk + GA) films, respectively. The surfaces were relatively smooth which is indicative of silk deposited from aqueous solutions on hydrophilic surfaces.[23,72] Slightly increased RMS of ultrathin silk films (usually below 1 nm) can be attributed to grainy and nanoporous morphology caused by localized polymerization of silk chains similarly to that observed for highly cross-linked ultrathin polymer and amino acid films as observed in recent studies.[77]

On the other hand, the difference in thickness for the silk and (silk + GA) films revealed that GA provides some changes in the silk secondary structure which promoted thicker film formation (Figure 2.2). However, surface morphology of the three-component (silk + GA + POSS), obtained by adding POSS into a pre-cross-linked silk solution, remained similar to that observed for the pristine silk film with a similar RMS of 1.1 ± 0.2 nm (Figure 2.5A,B). In contrast, incorporation of clay into a solution mixture resulted in more heterogeneous, much rougher, and more porous surface films with a RMS of 3.9 ± 0.2 nm (Figure 2.5C,D).

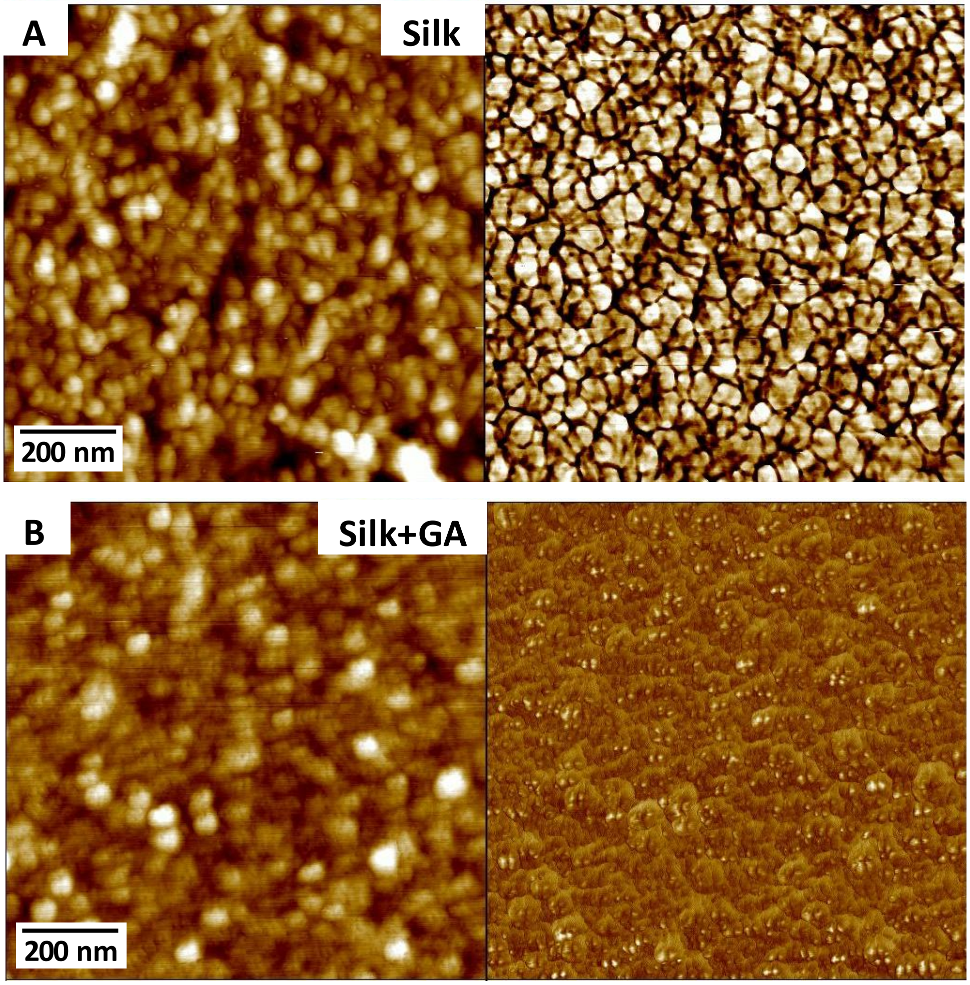

Figure 2.4: AFM topographical (left) and phase images (right) of silk surfaces with silk layers deposited from solution without cross-linking (A) and pre-cross-linked in solution before deposition (B).

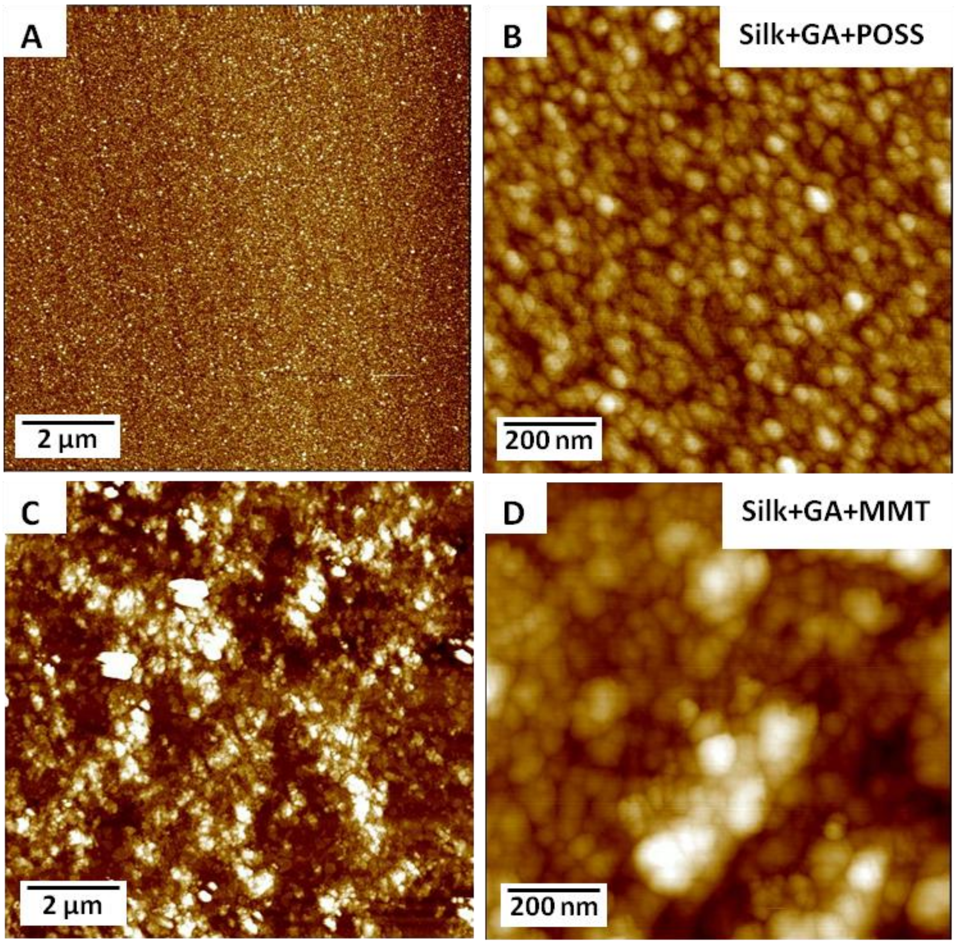

Figure 2.5: AFM topographical images of a single layer deposited from (silk + GA + POSS) (A,B) and (silk + GA + MMT) solutions (C,D).

The difference in surface morphology in (silk + GA + POSS) and (silk + GA + MMT) systems can be attributed to the difference in nanofiller nature. Apparently, the smaller dimensions of 2-nm POSS nanoparticles and their spherical nature does not significantly affect surface morphology of silk. In contrast, clay nanoplatelets are highly polydisperse and have irregular sheet-like structures which are ~1 nm thick and up to 200 nm wide.[59,92] Despite that the clay nanoplatelets are well-dispersed and do not form large microscopic aggregates in solution, they are not ideally oriented on a surface in a (silk + GA + MMT) film, leading to the high RMS. This random structure is in contrast to the almost ideal planar orientation of clay nanoplatelets observed in a conventional SA-LbL assembly of clay and silk.[59] Overall, the smoother (silk + GA + POSS) films are thinner in contrast to the (silk + GA + MMT) films.

2.2.3 Mechanical Properties

A typical buckling instability pattern under compressive stress illustrates that the film is uniform with periodic and equally spaced wrinkles, which can be exploited for the calculation of the compressive elastic modulus (Figure 2.6A). Figure 2.6 panels B and C also show the representative interference patterns of the silk-nanocomposite films under various pressures and stress-strain curves from bulging experiments, which enables the determination of the tensile mechanical properties.[37,93] The stress-strain data from the pressure-deflection measurements were obtained according to the usual approach for converting experimental parameters, Equation 1[51]

$$\sigma = \frac{Pa^2}{4hd} \quad \text{and} \quad \varepsilon = \frac{2d^2}{3a^2} \qquad (1)$$

where σ is the stress and ε is the strain. For this approach, the Young's modulus can be derived as the slope of the initial linear part of the stress-strain curves, which is associated to the reversible elastic deformation of the material. The toughness is the material's resistance to fracture when stressed, and can be determined by taking the integral underneath the stress-strain curves. It was shown that mechanical values increased with increase in film thickness until reaching a plateau.[86,94] In previous work on thin silk nanocomposites (<100 nm in thickness), the plateau was reached at ~70 nm.[59] On that basis, films of comparable thickness with the average range of 80 ± 10 nm were taken for the mechanical testing and presented in Tables 2.1 and 2.2.

As clear from this data, a significant enhancement of the mechanical properties is observed. First, it is worth noting that additional cross-linking of the $(\text{silk-MMT})_{20}$ films with GA leads to minor changes in mechanical properties with a 15% increase in Young's modulus (Table 2.1). In contrast, $(\text{silk + GA + MMT})_{15}$ films showed a 6-fold, improved Young's modulus, reaching 25 ± 2 GPa (Table 2.2). Correspondingly, the toughness for the films increased 3.5 times to 700 ± 80 kJ m^{-3}.

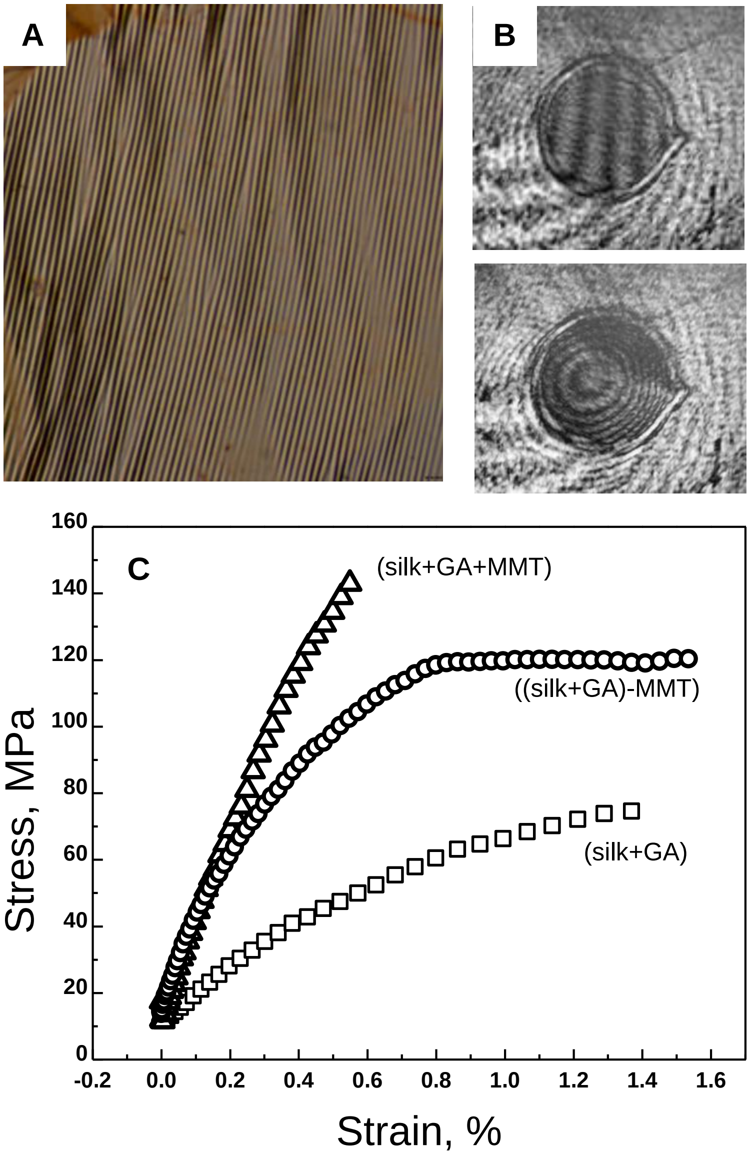

Figure 2.6: Optical image of a compressed (silk + GA + POSS)$_{20}$ film during buckling measurements (A). An interference pattern of the (silk + GA + POSS)$_{20}$ film suspended over a 150 μm opening under 0 Pa (top) and 3000 Pa (bottom) in a bulging experiment (B). Stress-strain data for the silk containing pre-cross-linked films (C).

Table 2.1: Mechanical Properties of Silk Nanocomposite Films Prepared by the Traditional SA-LbL Assembly

silk & clay composites	film thickness (nm)	bulging Young's modulus (GPa)	buckling Young's modulus (GPa)	toughness (kJ m^{-3})
$silk_{20}$	80 ± 1.5	4.1 ± 1.0	3.2 ± 1.5	200 ± 50
$(silk)_{20}$, GA*	80 ± 2.0	5.0 ± 1.0	4.5 ± 1.5	250 ± 50
$(silk\text{-}MMT)_{20}$	85 ± 1.5	12 ± 2.0	10.7 ± 1.5	950 ±100
$(silk\text{-}MMT)_{20}$, GA*	85 ± 2.0	14 ± 2.0	12.1 ±1.0	800 ±100
$(silk\text{-}POSS)_{20}$	83 ± 1.5	10.3 ± 1.5	8.9 ± 1.5	850 ± 50

GA* = films exposed to GA solutions after assembly.

Table 2.2: Mechanical Properties of Silk Nanocomposite Films Prepared by Utilizing the One-Step, One-Solution Approach

silk & clay composites	film thickness (nm)	bulging Young's modulus (GPa)	buckling Young's modulus (GPa)	toughness (kJ m^{-3})
$(silk + GA)_{20}$	90 ± 1.5	6.8 ± 2.0	5.7 ± 0.5	700 ± 80
$(silk + GA + MMT)_{15}$	80 ± 1.5	25 ± 2.0	21 ± 1.5	700 ± 100
$((silk + GA)\text{-}MMT)_{15}$	72 ± 1.2	20 ± 2.0	16.8 ± 2.0	1600 ± 150
$(silk + POSS)_{20}$	86 ± 1.5	12 ± 1.5	10 ± 1.5	800 ± 50
$(silk + GA + POSS)_{20}$	95 ± 1.5	18 ± 2.0	15.4 ± 1.5	1000 ± 100
$((silk + GA)\text{-}POSS)_{15}$	71 ± 1.5	10 ± 2.0	7 ± 1.5	1420 ± 150

Moreover, a drastic, 8-fold increase in toughness was achieved for ((silk + GA)-MMT)$_{15}$ systems obtained by sequential assembly of (silk + GA) solution with clay particles which afforded 1600 ± 100 kJ m^{-3} (Table 2.2). It was also found that even in the nanofiller-free (silk + GA)$_{20}$ films, obtained by assembly of silk premixed with GA, mechanical properties improved with almost a 2-fold increase in the elastic modulus and 3-fold increase in toughness. These results are in contrast to those for the (silk)$_{20}$ films exposed to GA after the film fabrication which showed no significant effect of the cross-linking on mechanical properties, indicating modest diffusion of the cross-linking agent into the silk matrix (Table 2.1). The improved mechanical properties of films produced from the cross-linked blend correlates well with previous work by Kotov et. al.[104], where GA cross-linking increased strength and toughness of both pure poly(vinyl alcohol) (PVA) and a PVA/MMT composite. For the silk-based nanocomposites in this study, expected underlying mechanisms responsible for such improvement in mechanical properties include a high degree of ordering of the MMT nanoplatelets combined with dense hydrogen bonding, covalent bonding, and stiffening of the polymer chains *via* GA-mediated cross-linking, resulting in effective load transfer between the MMT nanofiller and the silk matrix.

It is worth noting that in previous work a (silk-MMT)$_{17}$ film exhibited a 3-fold increase in elastic modulus to 12 ± 2 GPa and a 4-fold increase in toughness to 950 ± 100 kJ m^{-3}.[59] Therefore, by applying new silk processing method, a 2-fold increase in both mechanical strength and toughness has been achieved in this study. A similar trend was observed for POSS-containing silk nanocomposites. Incorporation of POSS by conventional SA-LbL assembly with silk resulted in a significant enhancement of mechanical properties for (silk-POSS)$_{20}$ as indicated by a 2-fold increase in Young's modulus and 4-fold increase in toughness to 10.3 ± 1.5 GPa and 850 ± 50 kJ m^{-3}, respectively (Table 2.1). An alternative assembly of the premixed (silk + POSS) solutions led to further increased elastic moduli up to 12 ± 1.5 GPa (Table 2.2). Further exposure of the (silk-POSS)$_{20}$ or (silk + POSS)$_{20}$ systems to the cross-linking solution did not affect mechanical values of the films (data not shown). In contrast, the drastic increase in mechanical properties was observed for the cross-linked blend (silk + GA + POSS)$_{20}$ systems which showed elastic modulus and toughness of 18 ± 1.5 GPa and 1000 ± 100 kJ m^{-3}, respectively (Table 2.2).

Finally, the effect of nanofiller volume fraction on composite performance was tested by varying the concentration of POSS solutions. The optimum concentration of POSS solution used to fabricate (silk-POSS) and (silk + POSS) films was found to be 0.2%. Up to this point, mechanical strength was in direct correlation with concentration, but a further increase in concentration to 1% resulted in brittle films. For example, 0.05% POSS solution afforded a 2-fold increase of both elastic modulus and toughness for (silk-POSS)$_{20}$ films, as compared to the pristine silk films (data not shown). The results on nanofiller concentration correlate well with those previously observed for (silk-MMT) composites.[59]

2.2.4 Silk Structural Conformations Followed by ATR-FTIR

To further investigate the mechanism of cross-linking-induced enhancement of mechanical properties, silk fibroin was adsorbed on a silicon surface in a liquid cell followed by introducing the GA cross-linking agent into the liquid cell. The ATR-FTIR spectrum in Figure 2.7 shows that the silk has a random coil secondary structure with the major peak centered at 1644 cm^{-1}, which correlates well with previous results on a hydrogenated silk layer adsorbed on surfaces.[78] However, a drastic difference in the spectrum was observed in the presence of GA. Cross-linking resulted in a gradual decrease in random coil silk I content (band at 1645 cm^{-1}) with an appearance of two peaks at 1688 and 1623 cm^{-1} attributed to significant presence of crystalline β-sheets of silk II.[95,96] The transition is time-dependent with silk II features appearing in the spectrum in 5 min until the final transformation was completed in 60 min (Figure 2.7). In contrast, the hydrogenated silk film (~80 nm) retained its random coil structure for at least 4 days in the absence of GA (data not shown). Previous results have also confirmed ATR-FTIR spectra for silk-only films (~100 nm) do not change over a time period of several weeks.[23] GA has been used extensively in the biomedical field as a cross-linking agent for proteins, because it can react with amino groups as well as hydroxy groups.[97] The associated chemical reactions are so complicated that a solid agreement on the main reaction mechanism has not been achieved, however, the mechanism involved may be a result of cyclization, dehydration, and internal redox reactions of Schiff bases formed with aldehydes and amine groups.[97] The dehydration, and expected formation of covalent acetal bridges between -OH groups of the silk chains, is a possible mechanistic explanation for GA causing formation of β-sheets within the silk secondary structure.[104]

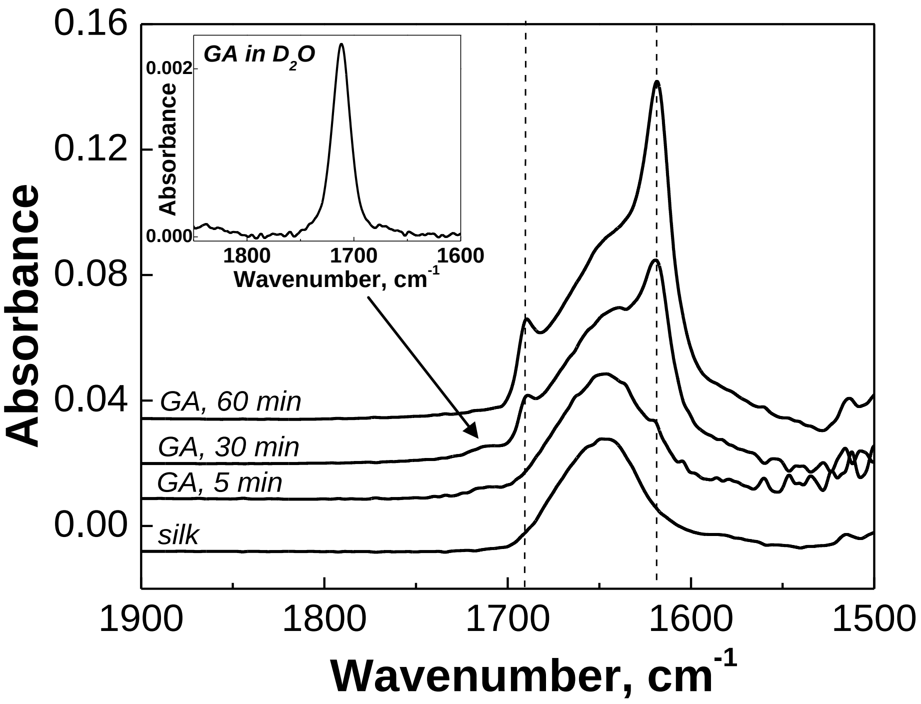

Figure 2.7: *In-situ* ATR-FTIR spectra of a silk layer before cross-linking (bottom spectrum) and after exposure to GA for different amounts of time. Silk was deposited *in situ* in a liquid cell from D_2O solutions on a Ge ATR crystal. Inset shows a GA spectrum in a D_2O solution.

2.2.5 Optical Properties

Transparency of silk-based nanocomposite films was measured in a wavelength range between 190 and 800 nm (Figure 2.8). Both POSS- and MMT-containing nanocomposites were highly transparent in the visible region (400-800 nm) with a slight decrease at 228 and 260 nm[98] as a result of clay and silk absorbance, respectively.

However, the transparency in the UV region (190-350 nm) consistently decreased for (silk + GA + POSS) and (silk + GA + MMT) systems. The more pronounced loss in (silk + GA + MMT) transparency can be attributed to the higher scattering of the films when compared to the highly transparent (95%) conventional silk-MMT films observed earlier.[59] As supported by the AFM results, the surface microroughness of (silk + GA + MMT) nanocomposites was higher than that for the (silk + GA + POSS) materials because of the large dimensions and random orientation of clay platelets at the interface.

The refractive index and absorption coefficients for silk and silk composites are shown in Figure 2.9. The refractive indices for the silk, silk-POSS, and silk-MMT samples, at a wavelength of 543 nm, are unexpectedly low at 1.23, 1.29, and 1.37, respectively (Figure 2.9A). The measured thicknesses of the samples were 22.8, 32.8, and 74.8 nm for silk, (silk + GA + POSS), and (silk + GA + MMT), respectively. The results designate that both POSS and MMT nanofillers induced an increase in the refractive index. The data correlate well with the previously reported increases in the refractive index of a material with increasing density and cross-linking of nanofillers within thin films.[69] The fact that the silk-MMT sample represents the highest value suggests that the MMT platelets contribute more in composite refractive index than very fine POSS nanoparticles, which correlates well with the optical density data.[99]

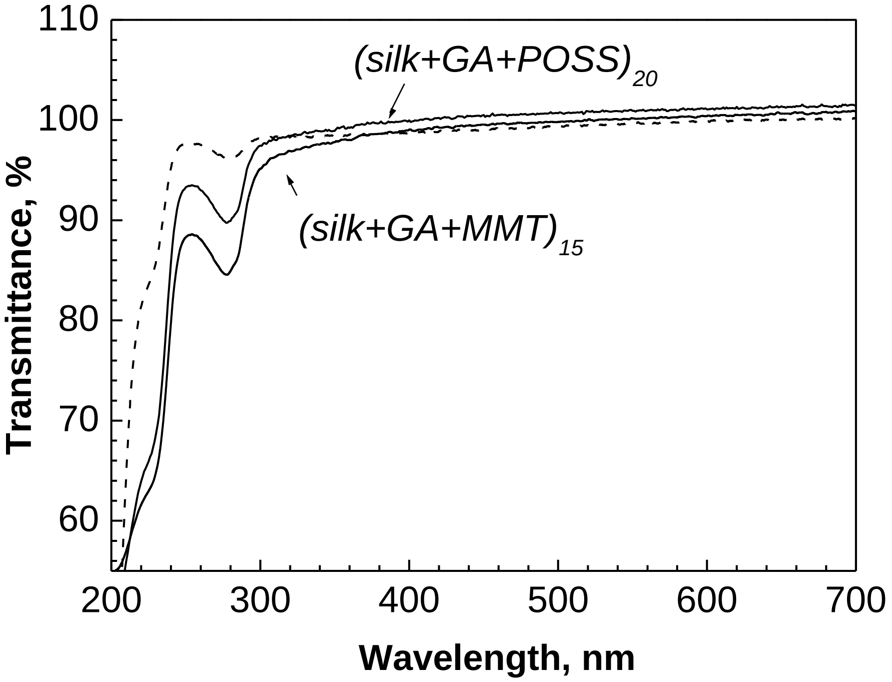

Figure 2.8: Transmission of (silk + GA + MMT)$_{15}$ and (silk + GA + POSS)$_{20}$ films. Transmission of a pristine (silk)$_{20}$ film is presented as a dashed line. Data for a quartz substrate was taken as background.

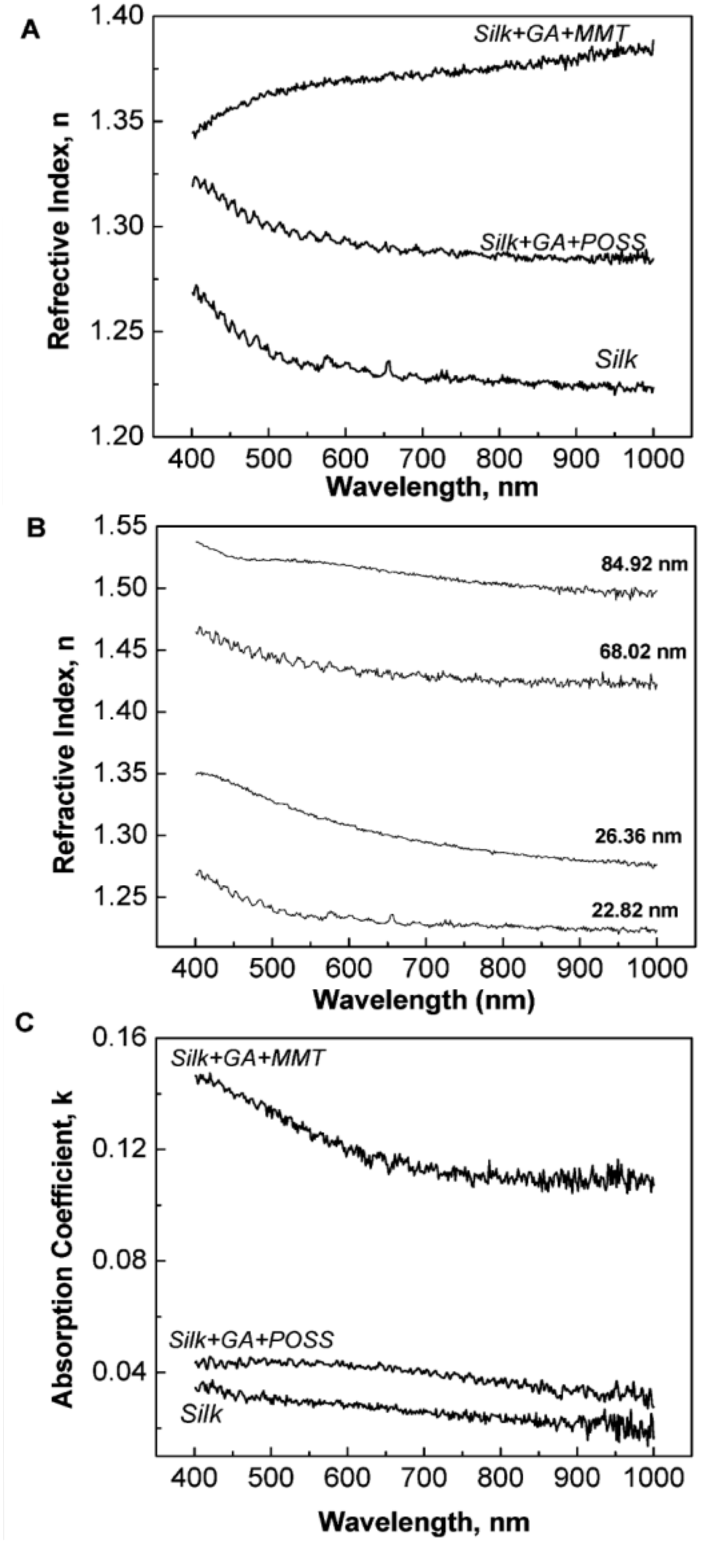

Figure 2.9: Refractive indices (A,B) and absorption coefficients (C) obtained for silk, (silk + GA + POSS), and (silk + GA + MMT) films. Thickness of silk films was of 22.82 nm, 26.36 nm, 68.02 nm, and 84.92 nm as measured by ellipsometry (B).

The refractive index value for the silk films are much lower than previous results for the refractive index of silk fibers, *n* = 1.538.[100] Another study determined the refractive index of silk fibroin filament to be 1.34.[101] The differences may be within the aqueous processing approach used for the films, compared to silk fibers in their native form. However, the most probable cause is highly grainy surface morphology and developed porosity of highly cross-linked silk matrices with nanometer thickness in contrast to that of silk films obtained *via* conventional spin-casting with uniform surface morphology.[37] The excessive porosity at nanoscale does not bring excessive light scattering but reduces effective refractive power of polymer films. Considering that the highest porosity should concentrate along the substrate-film and air-film interfaces due to excessive interfacial stresses, one should expect this effect to be much more pronounced for smaller film thicknesses and diminished for thicker films. To test this suggestion, a set of multilayered silk films with an increasing thickness up to 85 nm was fabricated (Figure 2.9B). For these pure silk films with increasing thickness, indeed a gradual increase in an overall level of the refractive index without significant changes of the wavelength variation was observed. For the thickest silk films tested here, which started reaching regular “bulk” state, refractive index values approaching 1.52 were observed, a common value for dense bulk silks.[100] This trend indicates that decreasing interfacial porosity brings the refractive properties in line with expected bulk values.

The absorption coefficients were found to be around 0.03, 0.04, and 0.13 for the silk, (silk + GA + POSS), and (silk + GA + POSS) samples, respectively (Figure 2.9C). The values were relatively low indicating that the films exhibited low optical absorption and were relatively transparent, confirming the aforementioned conclusion. The trend observed for the absorption coefficient, *k*, reveals that both types of nanofillers increased the amount of light scattering for the silk films, indicating that an increase in density of the silk films occurred after nanofiller inclusion. However, the use of fine silica POSS nanoparticles resulted in a much lower value for *k*, comparable to the original silk matrices.

2.3 General Discussion and Conclusion

The data provided in this study indicates that the one-step, one-solution fabrication SA-LbL route with inclusion of silk matrix cross-linking appears to be more efficient for obtaining reinforced nanocomposite films with enhanced mechanical properties than the traditional SA-LbL assembly route explored in earlier studies.[22] Both methods allowed for the introduction of nanofillers which significantly improved mechanical properties; however, the one-step mixed-solution approach afforded an additional 2-fold increase in mechanical strength due to the concurrent cross-linking. The highest elastic moduli were observed for (silk + GA + MMT) films, which showed 6-fold and 5-fold enhancements, respectively, when compared to the pristine silk matrix, reaching a remarkable 25 GPa for elastic modulus, 1.6 MJ/m^3 for toughness, and 150 MPa for ultimate strength.

In situ ATR-FTIR revealed that the GA cross-linker reacted successfully with amorphous silk solutions, inducing gradual silk crystallization. It has been previously reported that silk fibroin undergoes structural transitions from random coil silk I into crystalline silk II as a result of dehydration induced by a treatment with organic solvents, elevated temperatures, or by simple drying.[102] Results of this study indicate that such transformations can also be induced by covalent cross-linking as well. Indeed, silk has hydroxyl and amino groups such as serine, lysine, and arginine capable of chemical reactions with the GA cross-linking agent.[7,23] The results on silk conformational changes correlate well with the previously published data on cross-linking silk-chitosan blends with genipin, which also induced formation of β-sheet structures in initially amorphous silk.[103] In the latter case, ester groups of genipin interact with the amino groups of chitosan and silk, which leads to the formation of secondary amide linkages. In the case of this study, the change in the silk secondary structure provides an increase in film thickness observed in Figure 2.2. Indeed, β-sheet-rich silk is more hydrophobic than random silk and promotes thicker films when deposited on a surface. Moreover, silk transformation into a partially crystalline structure is responsible for the improved mechanical properties of the films.

In this study, the silk-based nanocomposite films assembled by the traditional route cannot be further reinforced by exposure to the cross-linking agent. The results are in contrast to the previously observed cross-linking of SA-LbL polyelectrolyte films with incorporated MMT particles.[104] In that case, GA was utilized to covalently cross-link hydroxyl groups of MMT and PVA in the preassembled polyelectrolyte-MMT matrices, which significantly improved mechanical properties (Table 2.3).[104] For this study, it is suggested that exposure to GA results in no significant enhancement in the preassembled silk films, because of limited diffusion of GA into the bulk silk. Indeed, dried silk is partially crystalline and adopts a β-sheet-rich structure (silk II) when assembled by SA-LbL, as a result of chain dehydration during spinning.[78] In contrast, when silk is in the random coil form and soluble in aqueous solutions the functional groups are easily accessible for the cross-linker, and efficient covalent cross-linking occurs in mixed solution. Moreover, the solution of partially cross-linked silk is clear, which favors stable aqueous dispersions with uniformly distributed components.

For comparative purposes, Table 2.3 lists several similar films reported in the literature along with their respective mechanical properties (i.e. Young's modulus and toughness). All film types were fabricated *via* the SA-LbL assembly technique, with the exception of the silk/AgNPL films where a Langmuir-Blodgett technique was used in addition to the spin-assisted deposition.[59] Furthermore, all nanocomposite films, independent of material type, benefited mechanically from the incorporation of nanofillers as reinforcing agents to the material bulk. The first "block" of sample types is associated with PVA and poly(diallydimethylammonium) (PDDA) polymer matrices and the effect of MMT integration and GA cross-linking on the stiffness of fabricated nanocomposites. The thicknesses of these films range from 1.0 - 1.5 µm, while the thickness values for the other films listed range from 50 - 110 nm. As noted earlier, it was shown that mechanical values increased with an increase in film thickness until reaching a plateau at ~70 nm.[59] Comparing the mechanical values for the (silk-MMT)$_n$ samples demonstrates this finding since the values increase with respect to a film with 50 nm thickness, (silk-MMT)$_{12}$, to those for (silk-MMT)$_{17}$ and (silk-MMT)$_{20}$ nanocomposites with thicknesses of 70 nm and 80 nm, respectively, and almost identical property values. The Young's modulus and toughness values reported in previous studies for pristine silk films corresponded very well to those measured in this study. Also, a similar ~2-fold increase in Young's modulus was recorded for when these films were either subjected to MeOH post-deposition, or when GA is utilized in the one-step, one-solution approach. Such a finding indicates formation of β-sheets was achieved by two different routes, and is further support of ATR-FTIR results representing significant presence of crystalline β-sheets of silk II induced by GA.

Table 2.3: Comparison of Mechanical Properties of Silk Nanocomposite Films to Similar Types of Films from the Literature

sample type	Young's modulus (GPa)	toughness (kJ m^{-3})	reference
PVA	1.7	not reported	105
PVA, GA*	2.0	not reported	105
PDDA	0.2	not reported	105
PDDA-MMT	11	not reported	87
PVA-MMT	13	not reported	105
PVA-MMT, GA*	106	not reported	105
silk$_{12}$	3.8	200	22, 59
silk$_{12}$, (MeOH)	7.5	not reported	22
(silk-MMT)$_{12}$	9.0	400	59
(silk-MMT)$_{17}$	11.5	950	59
(silk-MMT)$_{17}$, (MeOH)	17	720	59
silk$_{10}$-AgNPL-silk$_{10}$	13	500	59
silk$_{10}$-AgNPL-silk$_{10}$, (MeOH)	16	330	59
silk$_{20}$	3.7	200	This work
(silk+GA)$_{20}$	6.2	700	This work
(silk-MMT)$_{20}$	11.4	950	This work
(silk-MMT)$_{20}$, GA*	13	800	This work
(silk+GA+MMT)$_{15}$	23	700	This work
(silk+GA+POSS)$_{20}$	17	1000	This work

GA* = films exposed to GA solutions after assembly.

Comparison of nanocomposites with POSS versus MMT reinforcing agents shows that (silk + GA + POSS) films revealed slightly lower mechanical properties than (silk + GA + MMT) nanocomposite films (Table 2.2). Considering that POSS nanoparticles are comparable with dimensions of the silk random coils (5-10 nm) structure, one can expect a significant effect on mechanical properties.[21] Moreover, the recent theoretical studies on the dimensions of crystalline domains in silk fibroin showed the nanocrystals to be of 1-2 and 2-3 nm in length and height, respectively.[105] This means that the nanocrystals, which are responsible for the strength characteristics of silk and formed by either hydrogen-bonded β-sheets as physical cross-links or by chemical cross-linking, have dimensions similar to those of POSS nanoparticles, thus reducing the entropic barrier for mixing with the silk matrix. The observation that the Young's modulus in the case of POSS-containing films was still lower than that for those with MMT can be explained by the initially lower elastic modulus of POSS itself (7.5 GPa)[87] as compared to that of the clay (270 GPa)[106], thus reducing the overall reinforcing effect.

In order to compare the mechanical property results of the nanocomposite films to a simple rule of mixtures calculation, the volume % of nanofiller within the composites is needed. For example, a composite with 50 volume % MMT and 50 volume % silk would theoretically have a weighted mean of their respective Young's modulus values (270 GPa and 4 GPa) to result in an expected value of 137 GPa for the overall composite. The volume % of nanofiller present in the $(\text{silk-MMT})_{20}$ and $(\text{silk-POSS})_{20}$ composites was not determined in this study, but could be of interest for future studies. One possible route for determination of volume % of nanofiller within the composites is to use transmission electron microscopy (TEM) or AFM imaging for use in statistical image analysis by calculating the volume of the nanofiller particle (from known diameter) and multiplying by either the number of particles per area over the surface area of the image scan size for AFM, or by the number of particles per film volume (from film thickness and scan size) for TEM. Another possible route, which would have less associated observational error, would be utilization of thermogravimetric analysis for determination of weight % of the nanocomposite sample still present after subjecting the sample to temperature above the thermal degradation temperature of silk. The weight % still present at this temperature would correspond to the weight % of nanofiller present in the composite, and could be used for calculation of the volume % of nanofiller (from known density).

Although the volume % of nanofiller in the composite was not determined, a general comparison to the rule of mixtures can still be made from the mechanical property results. Using the average of the Young's modulus values determined by bulging and buckling tests for (silk-MMT)$_{20}$ of 11.4 GPa (Table 2.1) in a simple rule of mixtures calculation, results in a calculated MMT volume % value of 2.8%. This volume % of MMT in the composite is significantly less than expected from the 0.2% silk and 0.2% MMT concentrations used during SA-LbL assembly. Such a finding relates well to previous results on PVA/MMT composites[104], and can be explained as a result of the clay being incorporated as intercalated structures, rather than homogenously completely dispersed silicates, into the polymer matrix because of the strong tendency of the clay to aggregate and phase separate. On the other hand, using the mechanical property results in Table 2.1 for the (silk-POSS)$_{20}$ composite in a simple rule of mixtures calculation leads to a calculated POSS volume % value of 160%. Such a value is obviously impossible, but indicates a synergistic effect between silk and POSS since the averaged Young's modulus value of 9.6 GPa for (silk-POSS)$_{20}$ is greater than that of silk or POSS alone. This synergism can be explained by the previously mentioned similarity of the POSS nanoparticle dimensions and that of the silk fibroin nanocrystals, thus suggesting the mechanical enhancement of POSS-modified nanocrystals.

Optical properties were also affected by nanofiller incorporation. The inclusion of nanofillers did not compromise transparency of the films in the visible region, but the refractive index of MMT-silk nanocomposites was higher than that for the POSS systems. This relationship correlates well with the ellipsometric results on the absorption coefficients showing that the MMT-containing film scatters more light (higher k) than the POSS-containing samples. Furthermore, much smaller POSS nanoparticles uniformly distributed in the silk matrix more efficiently reduce overall fluctuations of the refractive index between the less-ordered phase and β-crystalline domains thus resulting in minimized optical losses in POSS-silk nanocomposites.

2.4 Experimental Section

2.4.1 Materials

A silk fibroin solution was prepared from *Bombyx mori* silkworm cocoons as described previously.[107] Briefly, cocoons were boiled for 30 min in an aqueous solution of 0.02 M Na_2CO_3 for 45 min to extract sericin, rinsed thoroughly with distilled water, and dried. The dry fibroin bundle was then dissolved in a 9.3 M aqueous solution of lithium bromide at 60 °C for 4 h and dialyzed against distilled water at room temperature for 3 days to remove the salt. The resulting solution was extracted from the dialysis cassettes (Slide-a-Lyzer, Pierce, molecular weight cutoff (MWCO) 3500) and remaining particulates were removed through centrifugation and syringe-based microfiltration (5 mm pore size, Millipore). This process enables the production of 8-10% w/v silk fibroin solution which was dissolved with Nanopure water to a 0.2% solution and used for LbL assembly. Nanopure water with a resistivity of 18.2 M cm was used in all experiments.

MMT (Cloisite Na) was supplied in powder form by Southern MMT Products (Figure 2.1). POSS-M, denoted as POSS in the manuscript, refers to mixed silsesquioxane cores (polyhedra, incompletely condensed polyhedra, ladder-type structures, linear structures, and all the possible combinations), in contrast to the geometrically specific POSS compounds (Figure 2.1). The POSS cores were synthesized by hydrolytic condensation of the precursor on a base of 3-aminopropyl triethoxysilane with a 2-fold molar excess of glycidol according to a well established procedure.[108] GA (70% in H2O, Aldrich) was diluted to 2% solution with water.

2.4.2 Instrumentation

AFM images were collected in the tapping mode with silicon tips with a spring constant of 50 N/m on a Dimension 3000 AFM microscope (Digital Instruments) according to usual procedure.[109,110] Transmittance spectra of the composite films were obtained on quartz substrates using a UV-2450 spectrophotometer (Shimadzu).

Ellipsometry was utilized to determine both the thickness and optical properties of the silk-nanocomposite films. A Woollam M2000U variable-angle spectroscopic ellipsometer system was used, and the reflected polarization states were acquired over the range 400-1000 nm at 1.59 nm intervals and at angles of incidence equal to 65°, 70°, and 75°. All data analyses were performed using Windows version WVASE32 software. The dispersion in the refractive index was modeled using a Cauchy fit and determined from the polarization data of the thin film samples and derived refractive indices. The complex refractive index is given by the equation ($n = n + ik$), where n is associated with the real part and corresponds to the refractivity of the material.[111] The ik is the imaginary part and corresponds to the light absorption of the material. The absorption coefficient, k, is a measure of the light scattering within a medium and absorption, with low values designating high optical transparency.

2.4.3 Buckling

Buckling tests were conducted to evaluate the compressive elastic modulus of composite membranes from the elastic buckling instability.[37] Buckling was achieved by the compression of the films deposited on PDMS substrate in accordance with a prior approach.[112] This method uses the strain-induced elastic buckling instability and can be applied to thin films.[94] For an isotropic thin membrane, a uniform buckling pattern with a characteristic wavelength, k, is observed when it is subjected to a critical compressive stress.[93] The spacing of this pattern is directly related to the elastic modulus. To initiate the buckling pattern, a 2 mm X 2 mm membrane piece was placed over a 0.6 cm X 0.6 cm X 0.4 cm PDMS substrate, which was slowly compressed with micrometer-sized increments. The compression was monitored in differential interference contrast (DIC) mode adjusted for maximum contrast. Optical images were captured with a Leica MZ16 microscope in reflection mode.

2.4.4 Bulging

Bulging tests were performed using a custom-made interferometer equipped with a charge coupled device (CCD) camera (Logitech) and a He-Ne laser (k = 632.8 nm). Pressures up to 5000 Pa were exerted using a 60 mL syringe regulated by an automatic pump (Kent Scientific, Inc.) and monitored with an automatic pressure gauge, DPM 0.1 (SI Pressure Instruments). The bulging test data were analyzed using a model for the elastic deformation of circular membranes, according to procedures described previously.[113] The SA-LbL membranes freely suspended over a copper substrate with a 150 µm hole were first inspected under an optical microscope, and a minimal pressure was exerted to check for symmetrical Newton's ring patterns that indicate membrane homogeneity before full load.

2.4.5 Construction of Nanocomposite Films

Figure 2.3 demonstrates two main fabrication approaches utilized in the study. In the first route, silk composites were obtained by traditional SA-LbL assembly from silk and nanofiller solutions. The method represents a traditional two-step approach which utilizes two different solutions in an alternating manner as previously applied to the systems of synthetic polyelectrolytes and clay nanosheets. First, multilayer silk and composite films were produced through deposition by the SA-LbL method as described elsewhere.[37] The depositions were performed either by the traditional alternating layers of silk and nanofiller particles (POSS or MMT)[7,114] or by using a one-step, single solution approach. For the traditional SA-LbL assembly, 30 µL of 0.2% silk aqueous solutions and nanofiller dispersion were sequentially dropped on silicon substrates pre-coated with sacrificial cellulose acetate and rotated for 20 s with a 3000-rpm rotation speed, rinsing twice with Nanopure water between the deposition steps. Thus, *n*-bilayer silk-MMT or silk-POSS films denoted as (silk-MMT)$_n$ or (silk-POSS)$_n$, respectively, were constructed. To perform cross-linking with different densities of cross-linking, the films were exposed to GA for 2, 5, 10, or 20 h.

In the one-step assembling approach, a mixed, three-component (silk, nanofiller, and GA) solution was sequentially deposited on a silicon substrate (Figure 2.3). The final concentrations of silk, nanofiller, and GA in the solution mixture were 0.5%, 0.2%, and 2%, respectively. The films were denoted as (silk + GA + MMT)$_n$, or (silk + GA + POSS)$_n$.

2.4.6 *In-situ* ATR-FTIR

Silk deposition and cross-linking were monitored by infrared spectroscopy using ATR-FTIR.[78] A Bruker FTIR spectrometer (Vertex 70) was equipped with a narrow-band mercury cadmium telluride detector. The internal compartment of the FTIR spectrometer containing the liquid cell was purged with dry nitrogen. The ATR surface was rectangular trapezoidal multiple reflection of a Ge crystal of dimension 50 mm X 10 mm X 2 mm (Harrick Scientific) whose beam entrance and exit surfaces were cut at 45 deg. Interferograms were collected at 4 cm^{-1} resolution, and the number of averaged scans was 120. Each interferogram was corrected on the corresponding background, measured for the same ATR cell with the same D_2O. To eliminate overlap of the IR bands in the 1700-1500 cm^{-1} region with the strong water band, D_2O with 99.9% isotope content was utilized.

For silk deposition *in situ*, 0.2% silk solutions in D_2O were adsorbed onto the surface of an oxidized Ge crystal for 10 min within the custom-made flow-through ATR-FTIR liquid cell (Harrick Scientific). After silk adsorption, the silk solution was replaced with pure D_2O. Use of multiple-reflection ATR along with a flow-through liquid cell allowed *in situ* deposition and compositional monitoring of ultrathin films (~several nm in thickness).[78] Cross-linking was performed *in situ* by filling the cell with 2% GA in D_2O solution, keeping the crystal exposed to the solution for various amounts of time, followed by extensive rinsing with a pure D_2O solution. The individual spectrum of GA was obtained in D_2O solution by taking the clean crystal as background. It is worth noting that on the basis of the ATR results silk was allowed to be partially cross-linked for 30 min before performing self-assembly from the silk-containing solution mixtures. The longer cross-linking time hindered film deposition because of silk gelation.

CHAPTER III

SILK LAYERING WITHIN MOLECULAR FILMS AS STUDIED WITH NEUTRON REFLECTIVITY

3.1 Introduction

As is known, X-ray and NR techniques are capable of probing phenomena throughout thin films and revealing how interfacial interactions affect gradient of ordering along the surface normal[115,116,117,118], with a spatial resolution at length scales ranging from submicrometers to that of intermolecular distances.[119] Several studies have been conducted using the combination of X-ray and NR techniques to investigate protein adsorption at interfaces[120,121,122,123], while various others focus solely on NR measurements to obtain desired adsorption information.[124,125,126,127] Furthermore, NR has shown promising results for characterization of multilayer polymer films with inhomogeneous distribution of components.[128,129,130,131]

However, most studies on silk fibroin have involved X-ray diffraction measurements of bulk materials to determine the structural characteristic of its three known secondary structures (random coil, silk I, and silk II) and do not provide insight into internal structuring of deposited silk layers.[132,133,134,135] Moreover, X-ray reflectivity does not provide the necessary contrast since the electron density contrast for biological systems is generally low[136,137,138], and the overall film microstructure composition is similar. On the other hand, NR examines length scales relevant for investigation of interactions of proteins and polymers, and adsorption of these molecules at liquid and solid surfaces.[119] An additional advantage of NR for this study is that the neutron scattering contrast between different isotopes of hydrogen, protium (^{1}H) and deuterium (^{2}H), can be exploited for examination of the swelling effect in ultrathin silk films. The high contrast of the absorption distribution across the interface is critical for obtaining rich structural information from nanostructured biopolymer-inorganic interfaces in the swollen state.[139] It is important to note that NR from silk swollen in contrasted solvent is the only way to reveal any inhomogeneities related to interfacial reorganization in secondary structures such as β-sheet crystallization.

NR studies were conducted on ultrathin, molecular-level silk films (< 30 nm) in combination with AFM imaging, spectroscopic ellipsometry studies, and previous FTIR data. Ultrathin films were fabricated using reconstituted silk fibroin solution and SA-LbL assembly. (Figure 3.1) Details regarding the interfacial behavior of silk macromolecules are revealed and depict a direct influence of the silicon oxide surface on structural organization within the films. The ability to tailor the structural density of these films by creating a silk template that becomes more dilute at the film-air interface at a certain distance from the substrate was demonstrated *via* multiple silk layer deposition. In addition, the effect of swelling of the films with D_2O solvent is presented in order to provide information regarding film organization and stability at the solid-liquid interface.

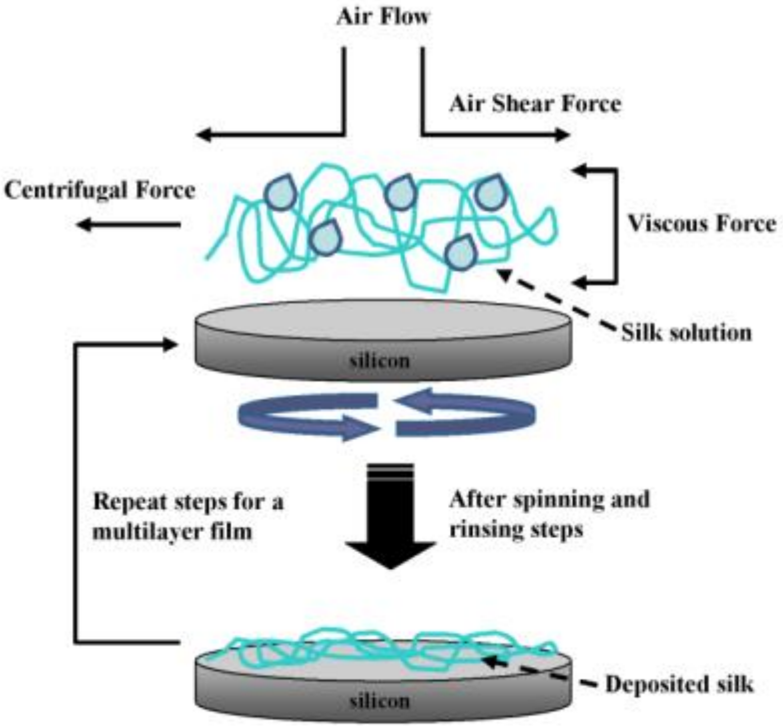

Figure 3.1: Schematic representation of the SA-LbL assembly process.

3.2 Results and Discussion

AFM and spectroscopic ellipsometry measurements were taken for independent verification of the film morphologies, roughness, and different layer thicknesses in the dry state (Table 3.1).

Table 3.1: Total Film Thicknesses and Microroughnesses (AFM and ellipsometry) for Dry Silk Films. Total Film Thickness Measured by Neutron Reflectivity for both Dry and Swollen Silk Films is shown for comparison

SA-LbL system		ellipsometry thickness (nm)	total film thickness by NR (nm)	AFM roughness (nm)
SiO_2		2.0	1.2	0.1
$(silk)_1$	dry	4.4	6.0	3.2 ± 0.4
	swollen	--	9.0	--
$(silk)_7$	dry	27.8	31.0	2.4 ± 0.5
	swollen	--	--	--

The film parameters determined from modeling the measured neutron reflectivity data: thickness, scattering length density (N_b), and internal roughness (σ), are summarized in Table 3.2.

Table 3.2: Neutron Reflectivity Model Parameters for Dry and Swollen Films

SA-LbL system	modeled film structure	$N_b \times 10^{-6}$ (nm^{-2})	d (nm)	roughness (nm)
SiO_2	SiO_2	376	1.2	0.5
$(silk)_1$ dry	silk monolayer	210	6.0	2.0
$(silk)_1$ swollen	dense silk (substrate)	185	5.5	0.9
	slightly swollen/expanded silk	110	3.5	2.5
	D_2O	638	--	--
$(silk)_7$ dry	densely packed silk (substrate)	100	6.0	5.5
	loosely packed silk (air interface)	44	25.0	20.0

3.2.1 Dry Silk Films

AFM imaging of silk films in the dry state indicates relatively smooth, uniform surfaces over large areas without the presence of large microscale defects, a common feature for SA-LbL films from silk materials. Some nanofibrillar components with open porous morphology were visible for both silk films, a common feature for SA-LbL silk films.[140] Some larger-scale surface segregation becomes visible for thicker silk films, which may cause dissolution and delamination of the surface elements after long term storage in liquid environments as will be discussed below.

At higher magnification, the characteristic fine domain texture was observed with domain dimensions below 50 nm, which are organized into elements of nanofibrillar structures as has been observed and discussed for ultrathin silk films earlier (Figure 3.2).[78,140] The domains are smaller in the thicker film and show a higher tendency to form random nanofibrillar structures and highly porous morphology. This is likely caused by the longer exposure to wet conditions during multiple depositions which promotes the formation of nanofibrillar structures at hydroxyl-terminated silicon oxide surfaces.[140] A distinct feature of both surfaces is extremely high porosity with pore sizes below 50 nm and high estimated surface coverage which can easily reach 50% for the top most layer.

The surface microroughness of the silk films calculated over a 1 x 1 μm^2 surface area resulted in similar RMS values of 3.2 ± 0.4 nm and 2.4 ± 0.5 nm for the $(silk)_1$ and $(silk)_7$ films, respectively, reflecting the similarity of the domain texture of the topmost silk layer. Through modeling of the NR data, the global surface roughness can be determined for comparison to AFM data by using the σ value associated with the modeled layer nearest the air interface (Tables 3.1,2). The external roughness values obtained from NR increase to 20 nm for dry $(silk)_7$ films, reflecting a rough and diffuse surface for thicker films with segregated surface nanofibrils, open pores, and domains across the whole silicon wafer.

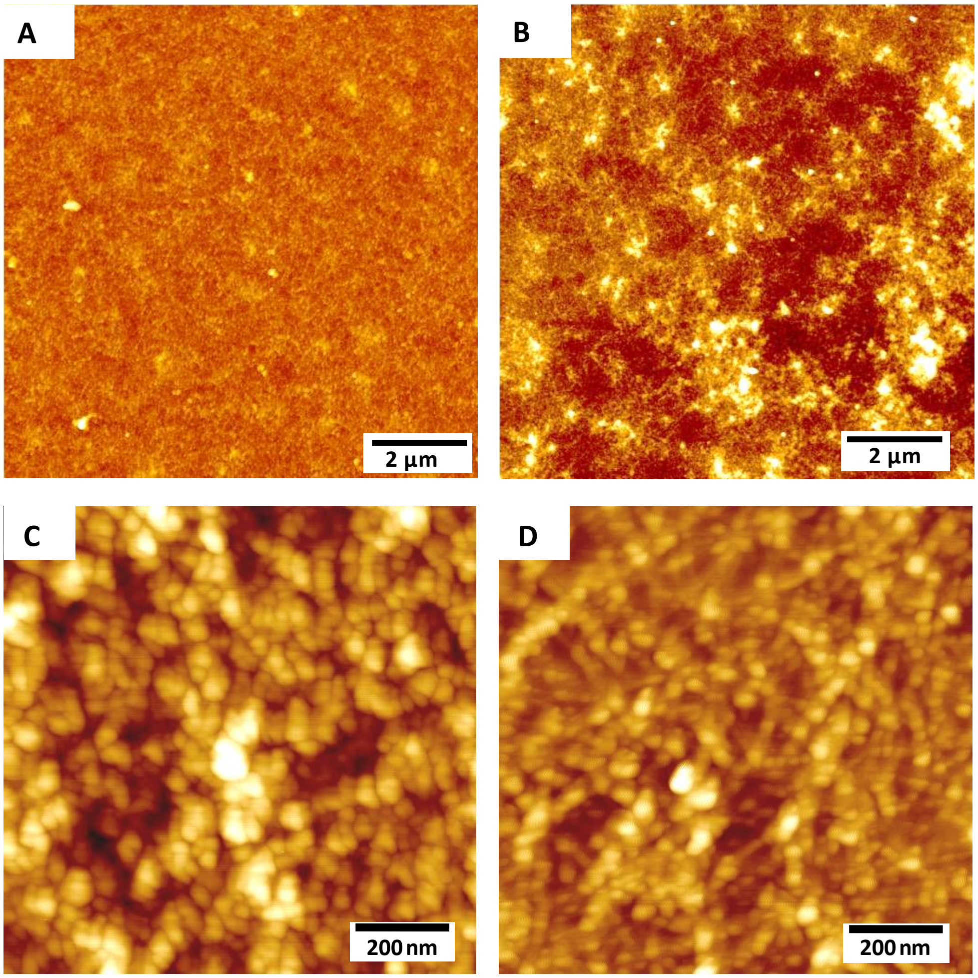

Figure 3.2: Topographical AFM images at different scales of (A,C) $(silk)_1$ monolayer and (B,D) $(silk)_7$ multilayer films.

Before NR measurements, the film thicknesses were measured with ellipsometry (Table 3.1). These thicknesses [$(silk)_1$ = 4.4 nm and $(silk)_7$ = 27.8 nm] correspond well to those reported in earlier results.[22] The following neutron reflectivity models provide similar but slightly larger thickness values, $(silk)_1$ = 6.0 nm and $(silk)_7$ = 31.0 nm, reflecting the overall uniformity of the silk films as probed with very different wavelengths (Tables 3.1,2). For simplicity, these films are referred as thin and thick for $(silk)_1$ and $(silk)_7$ films, respectively.

In Figure 3.3, logR (reflectivity) is plotted as a function of momentum transfer, Q. For both silk films there were no distinct Bragg peaks present indicating an absence of periodic stratification.[129,141,142] Critical Q values were similar for both films and the overall shape in mid-Q range can be used to model the overall film thickness as well as the internal vertical distribution for silk films. The fitting enabled minimum deviations between the modeled reflectivity profile and the measured data (see experimental data points along with solid fitting curves in Figure 3.3).

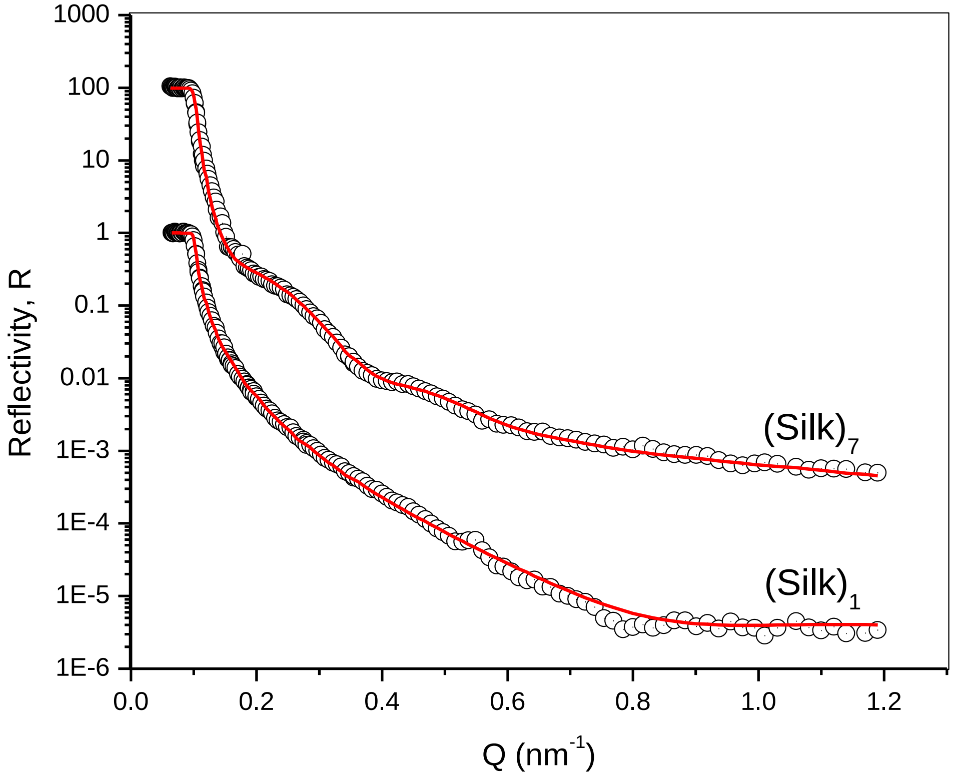

Figure 3.3: Neutron reflectivity data for dry (silk)$_1$ and (silk)$_7$ films where symbols and solid lines in the plot represent the experimental data and fit, respectively. The (silk)$_7$ curve is displaced vertically by a factor of 100 for clarity.

The scattering length density (SLD) profiles obtained from the fitting procedure show the density distribution along the direction normal to the film surface (Figure 3.4). The SLD profile for the dry (silk)$_1$ monolayer indicates that a single, relatively dense and probably partially crystalline silk monolayer of 6 nm thickness forms on the silicon oxide surface under these spin-cast deposition conditions. The interface between the silicon oxide layer and the silk film itself was determined to be 2.0 nm, in good agreement with the AFM experimental data (Tables 3.1,2).

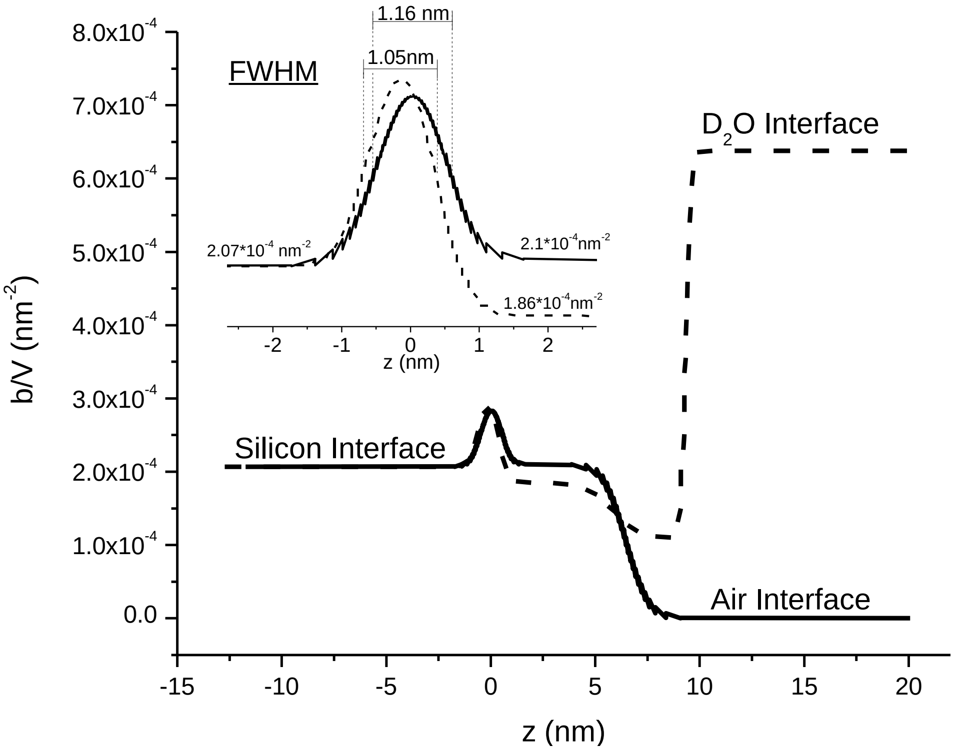

Figure 3.4: Neutron SLD profiles for (silk)$_1$ in both dry (solid) and swollen (dashed) states. Inset shows profile at the SiO$_2$-silk interface.

It is well-known that the driving force for the assembly of silk fibroin in a layered manner is related to hydrophobic, ionic, and hydrogen bonding interactions.[143] The interface formed between silk molecules and surface hydroxyl groups on the silicon substrate acts to form and stabilize nanofibril bundles formed by silk backbones in β-sheet conformation *via* minimization of interaction of these hydrophobic domains with highly hydrophilic surface.[67,144,145] Sequential hydrophobic and hydrophilic blocks are thus an important design feature for the assembly of silk at interfaces. [146,147] Extensive hydrophobic glycine-alanine repeats, with tyrosine present, facilitate hydrophobic interactions and dewetting of β-sheet domains in wet environments and thus intense formation of organized nanofibrillar structures in close proximity to the silicon surface.[82,146,148] On the other hand, the extensive hydrogen bonding of amino acids (such as glycine, alanine, and serine) stabilize the overall morphology of silk surface layer.[78,141,145,149]

Indeed, as has been already demonstrated by detailed FTIR studies on mono- and multilayered silk films, the dehydration of the silk surface layer during the spin-casting promotes hydrogen-bonding and β-sheet formation.[28,78,129,135] These FTIR results on the secondary structure of dry silk monolayers indicated conversion of silk layers to the crystalline β-sheet silk II structure with higher density as well as preservation of unorganized, random coil silk in thicker films with β-sheet content reaching 40-50%. Therefore, it is suggested that the silk monolayer is predominantly composed of denser silk in a β-sheet secondary structure as segregated nanofibrills and pores.

The modeling of the reflectivity data for the thicker $(\text{silk})_7$ film indicates a much more complex internal film structure, requiring a two-component model to account for drastically different scattering at the silicon-silk interface versus the air-silk interface (Figure 3.5). In this case, the SLD profile obtained from the best fit is composed of two layers with a thin (6 nm) layer with higher SLD level at the silicon-silk interface and a more loosely packed and much thicker (25 nm) topmost silk layer with lower SLD (Figure 3.5).

The presence of two distinct regions of low and high densities indicates different secondary structures of thicker silk films. The thickness of the higher SLD region of about 6 nm coincides with the thickness of the monolayer silk, although the SLD is lower by about half compared to that determined for the dry (silk)$_1$ monolayer, and therefore, the (silk)$_7$ interfacial layer is much less dense. This density reduction can be directly related to highly porous inner microstructure and a stronger tendency to form nanofibrillar structures resulting in higher porosity after multiple wet depositions as revealed by AFM. Large scale surface segregation and probably partial removal of the topmost silk material during consequential deposition and washing cycles facilitate much lower density of the thick (25 nm) topmost layer.

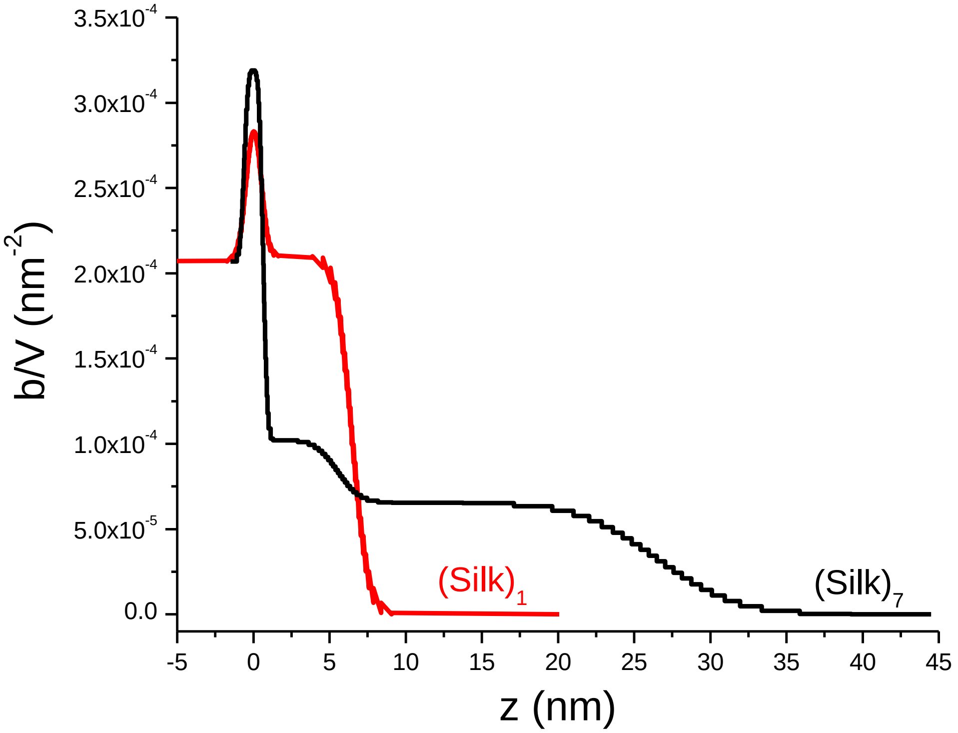

Figure 3.5: Neutron SLD profiles for (silk)$_1$ and (silk)$_7$ films in the dry state. Data for swollen film is not presented. As discussed in the text, a large portion of the swollen (silk)$_7$ film are delaminated, resulting in an extremely rough and reflectivity curve that could not be modeled.

3.2.2 Swollen Silk Films

The reflectivity curves for both $(\text{silk})_1$ and $(\text{silk})_7$ films swollen in D_2O become smeared in the swollen-state when compared to the dry state (Figure 3.3,6). The effects of swelling are most apparent in the case of the $(\text{silk})_1$ films, particularly when comparing the SLD profiles of dry silk to swollen $(\text{silk})_1$ as shown in Figure 3.4. Overall, the $(\text{silk})_1$ film exhibited dramatic expansion with swelling ratio of about 1.6 after immersion in D_2O with the non-uniform SLD distribution. It might be expected that diffusion of D_2O within the silk layers causes an increase in apparent density for those layers relative to a loosely packed region in the dry $(\text{silk})_7$ film. It is worth noting that no signs of increased SLD level were observed, which can be associated with H-D exchange.

However, surprisingly, an interfacial region of approximately 5 nm (in the vicinity of silicon oxide surface) remains virtually unswollen and densely packed, as indicated by an SLD that is only slightly lower than that of the dry $(\text{silk})_1$ monolayer probably. The SLD did not increase drastically as would be expected for swelling and uptake of D_2O, which is in agreement with the fact that this interfacial region is composed of the porous morphology with a network of hydrophobic nanofibrillar structures. The contact angle of silk surface of about 70^o corresponds to hydrophobic surface and open porous morphology is favorable for the formation of air nanobubbles at the liquid-solid interface.[150,151] It is speculated that air nanobubbles can be trapped in the region in open nanopores which prevents the penetration of liquid into the highly porous morphology with the network of nanofibrillar hydrophobic asperities similar to those observed for porous hydrophobic synthetic and biological surfaces in different fluid environments.[152] The presence of trapped air bubbles should lead to increased porosity and the reduction of the effective density of the silk layer after immersion in liquid environment.

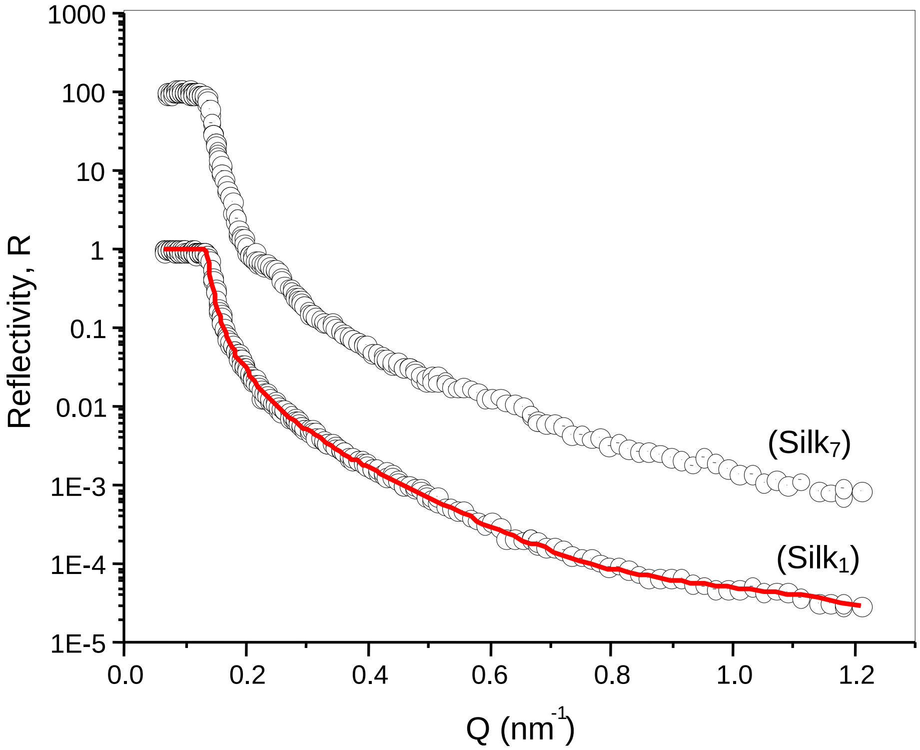

Figure 3.6: Neutron reflectivity data for (silk)$_1$ and (silk)$_7$ SLD profiles for (silk)$_7$ films in D_2O medium where symbols and solid lines in the plot represent the experimental data and fit, respectively. Modeled reflectivity curve is only presented in the case of swollen (silk)$_1$ because of delamination of thicker film in swollen state. The (silk)$_7$ curve is displaced vertically by a factor of 100 for clarity.

To quantify this non-uniform expansion, the “swelling ratio” profile was calculated for the $(\text{silk})_1$ film to reflect the local change in linear expansion of specific structural elements within silk monolayers (Figure 3.7). Similar calculations were not performed for the swollen $(\text{silk})_7$ film due to the loss of silk material into the D_2O swelling medium during measurement and the inability to quantitatively describe the film using an SLD profile.

The swelling profile of the monolayer silk film confirms highly non-uniform swelling and the formation of distinct two-tier swollen structures for the silk monolayers (Figure 3.7). The swelling profile has been calculated by direct comparison of thickness which can be assigned to different characteristic elements of the SLD profile: onset of SLD plateau, mid-point of the SLD plateau, onset of the transition region, mid-point of transition region, and the film surface. As this analysis shows, a fraction of the interfacial monolayer retains virtually unchanged and the apparent swelling ratio remains close to 1.0 (Figure 3.7).

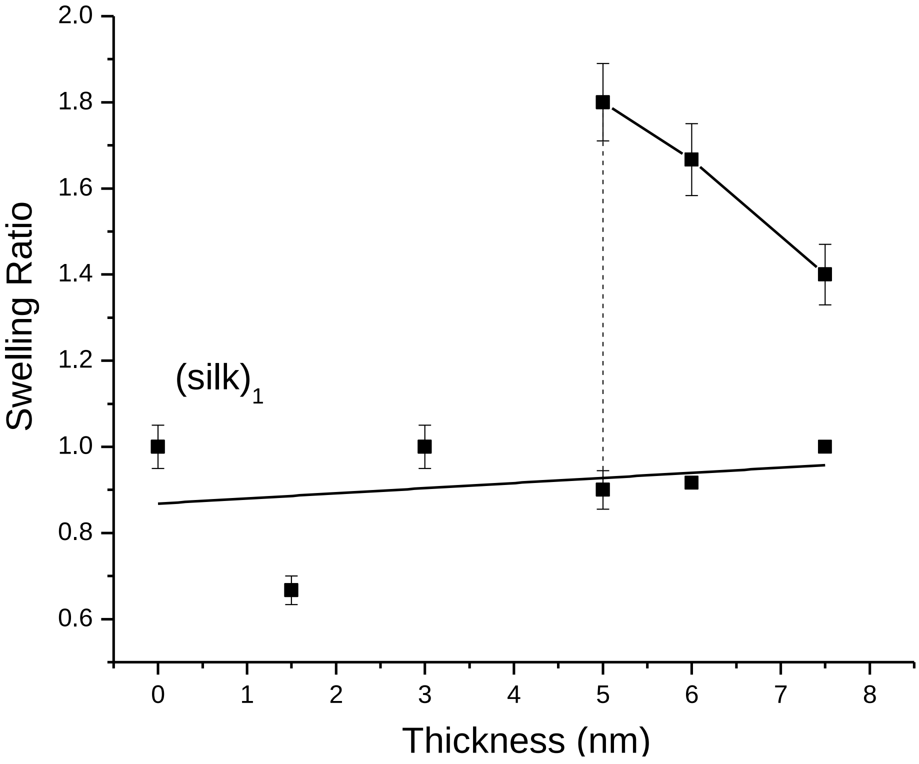

Figure 3.7: "Swelling ratio" profile for (silk)$_1$ film as determined by comparing SLD profiles in dry and wet states. Each data point represents ratio of expanded/initial thicknesses for characteristic points in the profile.

Then, the upper fraction of the monolayer becomes expanded by about 60%, forming the more loosely packed nanofibrillar structures with relatively limited water intrusion in this hydrophobic region due to trapped bubbles as suggested above and depicted in Figure 3.8. Such a surprising finding reveals that even a single monolayer of solid silk material which is partially transformed into the silk II phase in segregated nanofibrillar structures in the vicinity of the silicon surface can be expanded due to trapped air bubbles but not per-se highly swollen after addition of liquid.

In the case of $(\text{silk})_7$ films, the analysis is significantly more complicated. As shown in the reflectivity curve for the multilayer film in D_2O the reflectivity does not go to 1 below the critical edge (Q_c) but instead slopes downward steeply in Q (Figure 3.6). This is signature of an extremely rough surface that cannot be treated with the optical model used to model reflectivity data for uniform films. The highly rough surface is likely formed due to a large portion of the silk films and surface aggregates delaminating during measurements which has also been confirmed with AFM measurements (not shown).

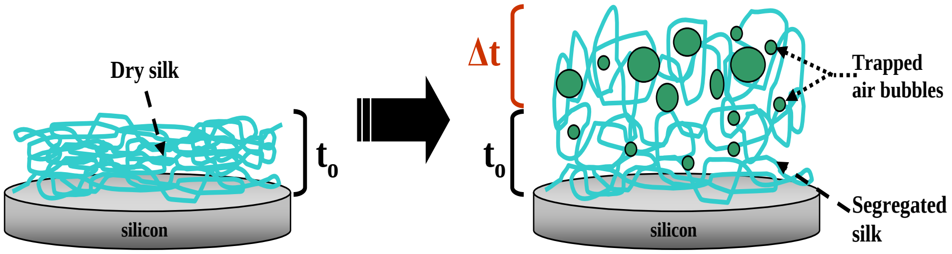

Figure 3.8: Two-tier swollen morphology of ultrathin silk films where the t_0 region indicates mostly interfacial segregated silk II nanofibrills and air nanobubbles, and Δt represents the expanded region of expanded silk and trapped air bubbles.

3.3 Conclusions

In conclusion, the neutron reflectivity studies conducted here have focused on (1) the depth profile of the layer organization within SA-LbL films as a function of film thickness and (2) the effect of swelling within the silk film structure as measured *in situ*. Under dry state conditions, the multilayer film resulted in a complex internal structure with two separate regions of SLD representing a denser microstructure near the SiO_2-silk interface brought on by the chosen deposition process and the formation of nanofibrillar morphologies. The surface-initiated segregation in proximity to the substrate (within the first 6 nm) can be associated with the interfacial crystallization in the β-sheet domains and nanofibrillization, with less dense random morphologies far from the interface.

Such a vertically segregated structure of solid silk films, which can be described by a two-layered model, explains their complex non-uniform swelling behavior in the presence of water. In the case of silk monolayers, the non-uniform swelling resulted in the formation of a two-tier expanded layer with a highly segregated and completely surface layer below 6 nm with trapped air bubbles. The expanded topmost layer is composed of random silk with trapped air bubbles with the integrated swelling ratio of the initial layer reaching 1.6. These studies indicate complex layering of silk in contact with silicon oxide surfaces in both dry and hydrated environments which have never been observed in earlier studies and can be critical for processing and design of silk-filler interfaces in composite biomaterials.

3.4 Experimental Section

3.4.1 Reconstituted Silk Fibroin Solution

For all experiments, 18.2 MΩ·cm Nanopure water was utilized. Silk was obtained from *Bombyx mori* silkworms raised on a diet of Silkworm Chow (Mullberry Farms, Fallbrook, CA). Live pupae were extracted from the cocoons prior to sericin removal. Cocoons were boiled for 30 min in an aqueous solution of 0.02 M Na_2CO_3 and then rinsed thoroughly with distilled water to extract the glue-like sericin proteins. The extracted silk fibroin was then dissolved in 9.3 M LiBr solution at 60 °C for 4 h, yielding a 20% (w/v) solution. The solution was dialyzed using Slide-a-Lyzer dialysis cassettes (Pierce, MWCO 3500) at room temperature for 3 days to remove the LiBr. After dialysis, the solution was centrifuged three times, each at 20 °C for 20 min, to remove impurities and the aggregates that occurred during dialysis. The final concentration of aqueous fibroin solution was 8.0% w/v, determined by weighing the remaining solid after drying. This solution was then diluted to obtain the desired 0.2% (w/v) silk concentration used for solution deposition.

3.4.2 Film Formation

Silk solution was spin-coated on <100> silicon wafers with a diameter of 5 cm, thickness of 10 mm, and one polished side (purchased from the Institute of Electronic Materials Technology, Poland). A schematic demonstration of the deposition procedure is illustrated in Figure 3.1. The SA-LbL deposition method was performed by sequentially dropping silk onto the silicon substrate using 3 mL shots of silk solution, rotating for 60 s at 3000 rpm on a spin-coater (Laurell Technologies), rinsing once with Nanopure water to remove unbound silk, followed by deposition of the next layer in accordance with usual procedure.[143] After film fabrication, the films were dried in ambient conditions for neutron reflectivity measurements.

3.4.3 Film Characterization

The morphology of the pristine silk films was first characterized with a Dimension 3000 instrument (Digital Instruments) by conducting AFM imaging in the light tapping mode according to the established procedure using silicon tips with a cantilever spring constant of 50 N m^{-1}.[109,110] Ellipsometry measurements of film thickness were performed with a Woollam M2000U multiangle spectroscopic ellipsometer with measurements at three different angles: 65°, 70°, and 75°. Thicknesses of dry films were determined using a data fit with the Cauchy model over the range of wavelengths, λ, of 250-1000 nm.

3.4.4 Neutron Reflectivity

NR measurements were conducted on dry and hydrated SA-LbL films at the Spallation Neutron Source Liquids Reflectometer (SNS-LR) at Oak Ridge National Laboratory (ORNL). The SNS-LR collects specular reflectivity data in a continuous-wavelength band at several different incident angles. Measurements were conducted in three independent series to ensure the reproducibility of the experimental data.

For the data presented here, the wavelength band of $0.2 \text{ nm} < \lambda < 0.55 \text{ nm}$ was used and reflectivity at angles of $\theta = 0.15, 0.25, 0.40, 0.75$, and 1.20° was measured, thereby spanning a wide total wavevector transfer range of $0.06 \text{ nm}^{-1} < Q < 1.2 \text{ nm}^{-1}$ where $Q = (4\pi \sin \theta)/\lambda$ where θ is the incident angle and λ is the neutron wavelength. The data was collected at each angle with incident-beam slits set to maintain the wavevector resolution constant at δQ/Q = 0.05, which allowed for stitching the five different angle data sets together into a single reflectivity curve. NR data, from dry films as well as in a liquid environment, was collected by placing specimens in a liquid-cell with the top surface in contact with D_2O. Isotopic substitution of protium with deuterium, known as the contrast variation method, is frequently implemented due to the large SLD contrast between the two when compared to hydrogen, thus enabling clear distinction between structural inhomogeneities in the liquid state which cannot be otherwise revealed.[128,130,134,142,153]

The data was analyzed using a model developed at ORNL with conventional NR data fitting techniques.[154] To fit the data, an idealized film structure featuring sharp interfaces between adjacent layers was started with. This model was then modified to accommodate the physically measured structures by adjusting layer thicknesses, SLD, and roughness to best model the measured data in both dry and swollen states.[154]

Initial individual layer thicknesses for simulations were taken from ellipsometry measurements and then adjusted to the data. The neutron scattering density is defined as $\Sigma = b/\mathrm{V}$, where b is the monomer scattering length (sum of the scattering lengths of constituent atomic nuclei) and V is the monomer volume.[154] The value of $(b/\mathrm{V})_n$ can be related to the molecular properties of the film through:

$$(b/V)_n = \frac{N_A \rho_b \sum b_i}{MW} \tag{2}$$

where N_A is Avogadro’s number, ρ_b is the mass density in the volume of interest, b_i is the scattering length of *i*th element in the repeat unit summed over all atoms in the repeat unit, and MW is the molar mass of a representative repeat unit of the polymer.

Therefore, the SLD varies as a function of the mass density of the film as well as the local composition in the film.[153] Standard SLD values were used for common materials including D_2O (6.38×10^{-6} Å^{-2}) and silicon oxide (3.76×10^{-6} Å^{-2}) unless otherwise noted. Layer intermixing was simulated by error function density profiles (Gaussian roughness).[109] The swelling profile for $(\text{silk})_1$ was calculated as a ratio of all characteristic dimension points (e.g., midranges of transition zones and zones with constant SLD) in dry and in-fluid states.

CHAPTER IV

NANOSTRUCTURED INTERFACES OF BIOCOMPATIBLE SILK FIBROIN FILMS

4.1 Introduction

Robust patterned ultrathin silk-based frames were fabricated using a combination of interference lithography (IL), soft lithography, and spin-coating techniques. The approach taken exemplifies construction of novel material systems achieved through combination of inexpensive patterning and templating routes affording the ability to custom tailor the composition, and hence, the overall functionality. IL is promising for fast microfabrication of complex 2D and 3D nanostructures, and enables nanoscale features (i.e. pores and pillars) with 2D and 3D lattices containing micro- to nanometer spacing, unachievable by traditional photolithography.[81] Fabrication of silk films involved replica molding *via* micromolding in capillaries, an efficient soft lithography method for duplication of structure present in the surface of a mold, allowing for creation of an elastomeric PDMS stamp for repeatable usage.[156,155] This approach provides a route for accurate replication of master molds with sub-micron topographical features in the absence of additional chemicals, salts, or high pressures which sometimes accompany nanofabrication techniques and limits the use of biological macromolecules.[40] Use of a soft lithography-based casting technique with silk fibroin solution has been previously reported[78,156], and resulted in films having intricate nanopatterns of at least 30 nm transverse features.

Template-assisted fabrication is an increasingly significant method for fabrication of porous networks obtained by a negative replica of a second desired material.[73] Porous polymer templates constructed with inorganic nanoparticles, *via* modification of the templates with functional groups such as thiols, pyridyl, or amino groups, have been reviewed[81], thus demonstrating the ability to create structures with organized variations in properties. GNP nucleation and growth directed by poly-L-tyrosine (pTyr), a synthetic polyaminoacid, for creation of solid, flexible, and patterned surfaces without agglomeration has also been reported.[68] The reducing activity of tyrosine groups in pTyr was activated by immersing a pTyr decorated surface into borate buffer at pH 10.[68] Interest has increased in the utilization of GNPs due to their facile synthesis, known surface chemistry, narrow size distribution, and the significant change in mechanical, optical, and electrical properties imparted to the template material. More specifically, interactions of GNPs with polymer templates affect color, reinforce structures, enable certain optical detection methods, and bestow light-responsive behavior.[50] The nanomechanical properties of micropatterned membranes containing GNP microarrays have been investigated, and a two-stage wrinkling was observed with spatially correlated instabilities dependent on alternating regions of different elastic properties induced by the encapsulation of the micropatterned array of GNPs.[93]

Random coil secondary structure (silk I) is produced after direct processing from aqueous silk solution; however, silk I experiences an irreversible transition to a crystalline material with a high content of anti-parallel β-sheets (silk II) after treatment with MeOH to induce dehydration.[71] The amino acid repeat in silk protein is responsible for the formation of β-sheets and consists of the sequence GAGAGSGAAG[SGAGAG]$_8$Y, where G = glycine, A = alanine, S = serine, and Y = tyrosine.[71] Tyrosine groups in silk reduce metal ions from aqueous solution without the need of additional reducing agents, and enables *in situ* synthesis of metal nanoparticles at ambient conditions(ref 41). The tyrosine residue effectively reduced Au$_{(III)}$ ions to Au colloids due to the amine functional groups displaying strong electron donating properties. Ionized at high pH, the cresol components of tyrosine is transformed partially to phenoxide anions, thereby, increasing the electron density in the π-π* transition and leading to electron transfer from tyrosine residue to Au$_{(III)}$).(ref 41) A previous study revealed both silk I and silk II facilitate gold nanoparticle formation, indicating tyrosine groups are available for metal ion reduction in both forms of silk.[23] β-sheets in silk II facilitates tyrosine ordering thereby resulting in well-dispersed, uniform nanoparticles. It has also been shown that mineralization does not result in transformation of the silk I secondary structure to silk II.[23]

Both types of silk were utilized for two separately patterned frames, porous and pillar, fabricated with nanoscale features (<200 nm). Furthermore, the patterned silk frames were subjected to mineralization using a gold chloride ($HAuCl_4$) / borate buffer solution to obtain inorganic-organic hybrid nanocomposites with patterned surfaces allowing for increased understanding that could lead to controlled tunability of the nucleation and growth rates of secondary particles, such as GNPs. The coupling of GNPs with silk fibroin matrices allows for the production of functionalized surfaces that can subsequently be characterized to analyze their value for prospective application in areas such as optical sensing and bioengineering.[23] Characterization of silk I, silk II, and surface mineralized films was conducted *via* AFM, SEM, and optical microscopy. AFM, SEM, and optical imaging were utilized to collect qualitative information regarding the silk films' topography, while AFM sectioning and 2D FFT imaging were employed to determine the periodicity of the structured arrays and heights of nanoscale features.

4.2 Results and Discussion

4.2.1 Surface Structured Silk Frames

The patterning of silk fibroin frames occurred through a modified soft lithography casting process, where two sets of molding masters were applied. Micromolding in capillaries was selected to replicate a 833 nm bi-lateral periodicity with 280 nm cylindrical features in the initial mold previously formed by IL in a multifunctional epoxy derivative of a bisphenol-A Novolac (SU-8) negative photoresist.[73,155] The original SU-8 master mold was duplicated through use of negative PDMS replicas, allowing for construction of several polystyrene (PS) molds with similar periodicity and height of features to assure protection of the valuable SU8 mold.[73] Compared to rigid molds, molding against elastomeric PDMS provides certain benefits such as a surface with low interfacial energy and increased conformal contact with substrate surfaces, resulting in easier release of small, fragile structures. Furthermore, PDMS can be deformed reversibly and repeatedly without residual distortion and is thermally and chemically stable, nontoxic, inexpensive, and commercially available.[155]

In this study, previously fabricated PS molds attached on silicon wafers were placed in a glass Petri dish with the patterned surface exposed upwards. The container was subsequently filled with a thick layer of PDMS pre-polymer, and vacuum assisted deposition was performed to facilitate filling of patterned grooves on the surface for replication of structural features and to minimize the amount of trapped air which would result in the formation of bubbles. PDMS pre-polymer, liquid at room temperature, was cured on top of the PS mold, thereby converting the pre-polymer *via* cross-linking into a solid elastomer with an inverse pattern of the original master on the surface of the PDMS. After obtainment of the PDMS stamp, the spin-coating method was used to deposit aqueous silk solution onto the mold for formation of silk frames with similar patterned structure as the PS molds. The final fabrication step consisted of transferring the silk frame from the PDMS stamp onto a silicon substrate used for facile characterization. This simple step involved contact of the deposited silk frame, still on the PDMS stamp, with a silicon substrate, followed by applied pressure to release the silk frame from the PDMS stamp due to preferential adhesive interaction of the silk-silicon interface versus the silk-PDMS as a result of silk I hydrophilic surface residues' affinity to hydroxyl groups on the silicon oxide surface opposed to the hydrophobic surface of PDMS. The fabrication steps for creation of the surface structured silk frames are illustrated in Figure 4.1. Additionally, several frames were immersed in MeOH for 1 - 2 min to induce transition of secondary structure from silk I to silk II.

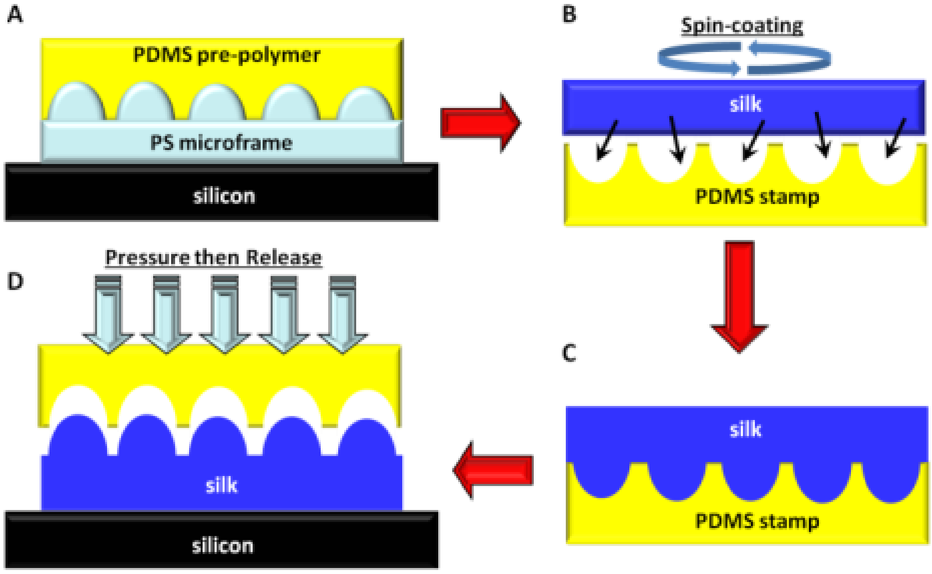

Figure 4.1: Schematic representation of the fabrication approach used to construct the silk fibroin frames (pillar pattern shown). Creation of PDMS negative replica of PS microframe master (A), spin-coating deposition of silk onto PDMS stamp (B), replication of PS master with silk (C), transfer of silk frame onto silicon substrate (D).

4.2.2 Investigation of Structural Features

AFM cross-sectional analysis was conducted for investigation of the pattern periodicity and heights of the nanoscale features present on the surface of the PS mold, PDMS inverse replica, silk I replica, and silk II replica (Figure 4.2). As shown in Table 4.1, the height dimensions trend lower during replication caused by capillary force and surface tension leading to partial filling of the mold cavities. Moreover, this mechanistic effect is exacerbated when replicating from the porous topography to the pillar, as opposed to from the pillar to the porous. For example, the difference between the porous PS mold and the pillar PDMS inverse replica is 87 nm, while the difference between the pillar PS and porous PDMS is only 40 nm. Such a result is also seen during the inverse replication of the PDMS pattern *via* silk I deposition. An explanation for this outcome is the decreased area of the mold cavity present in the pattern. For replication of the porous pattern a small cavity must be infiltrated to produce a pillar feature; on the other hand, a large cavity area is present for the pillar pattern facilitating the generation of porous features as a result of material filling around the pillar features. Moreover, this effect is intensified by the high viscosity of the PDMS pre-polymer. A much larger difference in height dimensions when replicating with PDMS versus silk I was recorded, with the largest difference present in the replication of PS porous pattern to PDMS pillar. These results correlate well with those of the initial fabrication of the PS original molds, where the vertical heights of porous features were SU8 ~ 300 nm, PDMS = 200 nm , and PS = 150 nm.[73] The PS porous structure height recorded in this study (179 nm) is similar to the 150 nm value, and the slight difference can be attributed to variability in the feature replication from one PS mold to another.

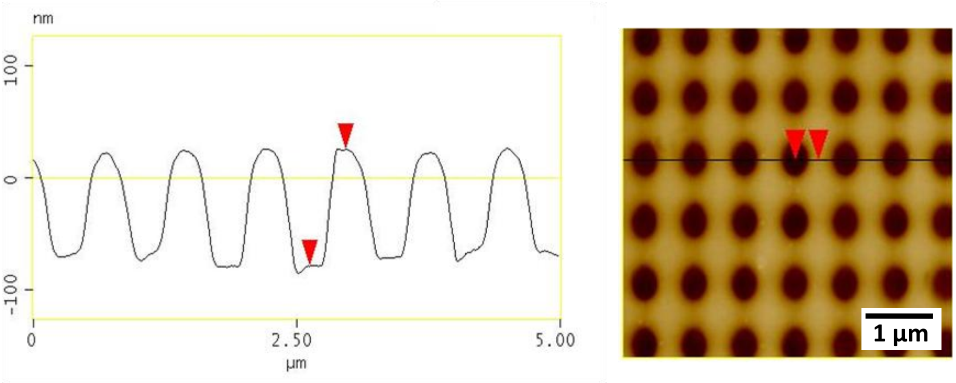

Figure 4.2: Sample of cross-sectional analysis from AFM imaging showing measured height of nanoscale features (porous pattern shown).

Table 4.1: Patterned Features' Heights and bi-directional Periodicity of Original Molds (PS), Negative Replicas (PDMS), and Replicas (Silk I & Silk II) for both Pillar and Porous Pattern Structures

patterned structure	template material	structure height (nm)	lattice spacing (nm)
pillar	PS	205	927
	PDMS	165	833
	silk I	132	850
	silk II	86	863
porous	PS	179	896
	PDMS	92	876
	silk I	95	853
	silk II	86	853

A similar partial filling effect was seen after deposition of silk I onto the PDMS stamp for replication of the features present in the PS mold. The lower volume cavities of the porous PDMS pattern hampered the ability of silk I to completely infiltrate, as depicted by the decrease in height of 33 nm. However, silk I appeared to completely fill the PDMS pillar topography and even had a slightly greater (3 nm) height dimension of the features. The creation of air cavities between the top of the PDMS pillars and the bottom of the silk I pores could be an explanation for this finding. Another possibility is based on the elastic deformation of the PDMS stamp due to compression during transfer of the deposited silk onto a silicon substrate. The porous PDMS stamp has more surface contact during compression compared to the pillar PDMS stamp, which may induce mechanical strain upon silk I causing a decrease in feature height and perhaps even a slight transition to silk II. Furthermore, strain imparted during transfer of the silk frame from PDMS to silicon appeared to produce a more oval-like feature morphology rather than circular. The appearance of these oval-like features can be seen in the AFM topographical images displayed in Figure 4.3, and more evidence to this conclusion is brought to attention by the seemingly bi-directional variability of the periodicity discovered during AFM cross-sectional analysis. Analyzed samples were found to have a noticeable difference in lattice spacing when measured from one direction versus its perpendicular direction (data not shown).

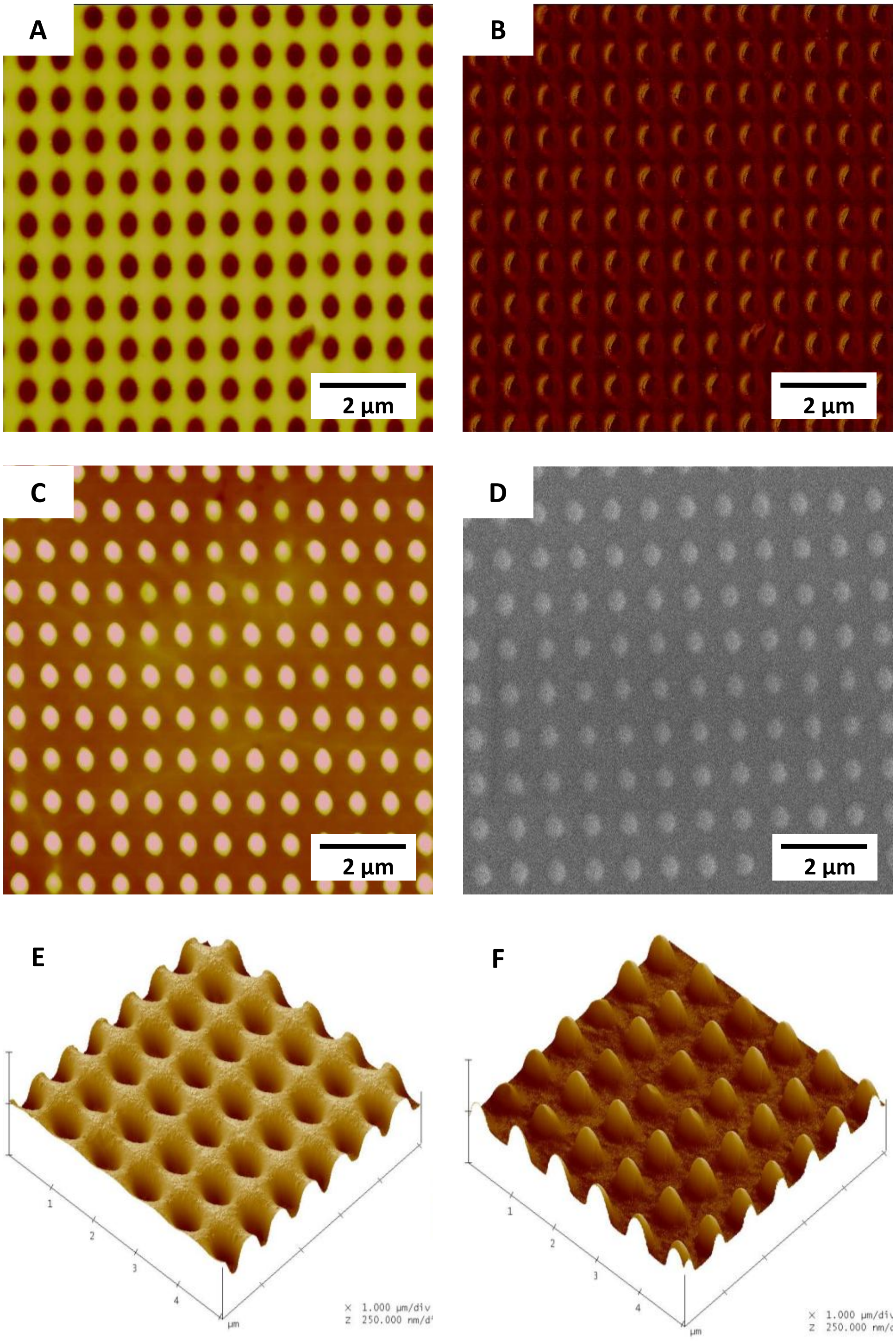

Figure 4.3: AFM topographical (A) and phase images (B) of silk I porous frame. AFM topographical image of pillar frame (C) and SEM image of pillar frame (D), all images were produced over a 10x10 μm^2 scanning area. 3D AFM illuminated surface plots of porous (E) and pillar (F) frames (5x5 μm^2).

For evaluation of tuning dimensions through secondary structure, silk I pillar and porous frames were immersed in MeOH to induce transition to silk II and associated changes were measured via AFM cross-sectional analysis (Table 4.1). A significant 35% reduction in heights of pillars was discovered after silk I transitioned to silk II, along with a slight increase in lattice spacing of these nanoscale features. A lesser reduction of 9.5% for heights of the porous features, with no change in periodicity was recorded. These findings can be likely explained by a decrease in free volume as the surface converts to silk II. Rearrangement of the protein strands occurs as the secondary structure is converted by formation of β-sheets developing the crystalline state of silk II. The more organized structure of silk II results in an increase in density, and thus, a reduction of volume occupied. Furthermore, the greater reduction in heights of pillars versus pores can be attributed to the larger impact this rearrangement has on higher surface area features. The area surrounding pore cavities likely inhibits this reduction as it is the more bulky portion of the pattern. In comparison, the pillar features are only held rigidly at their base and the upper portion experiences an enhancement of this rearrangement effect due to no physical restriction of surrounding material. A small difference in lattice spacing of pattern features was experienced, implying an isotropic rearrangement where the size of features are reduced, but location is unaffected.

Difficulty of precise tip contact location during cross-sectional analysis is possible reasoning for the greater lattice spacing of PS in comparison to the PDMS molds. The sharper features expected to be present in the PS mold compared to the PDMS, due to partial cavity filling during replication, provides a more narrow location for surface contact with the tip of the AFM cantilever. The surface tension and capillary forces present causes a broadening of the nanoscale features to a more plateau-like morphology. This broadening effect facilitates tip contact allowing for more exact analytical data to be obtained. For evaluation of the macroscale bi-lateral periodicity of nanoscale features present on the patterned surfaces, AFM imaging was implemented to attain 2D FFT images of PS molds, silk I frames, and silk II frames (Figure 4.4). In contrast to the varying localized periodicity from one material to the other, determined by AFM cross-sectional analysis at the microscale, all of the images revealed a periodicity of exactly 833 nm. This result shows that the bi-lateral lattice spacing of the nanoscale features were accurately duplicated from the original SU-8 master mold to maintain pattern uniformity across long-range order.

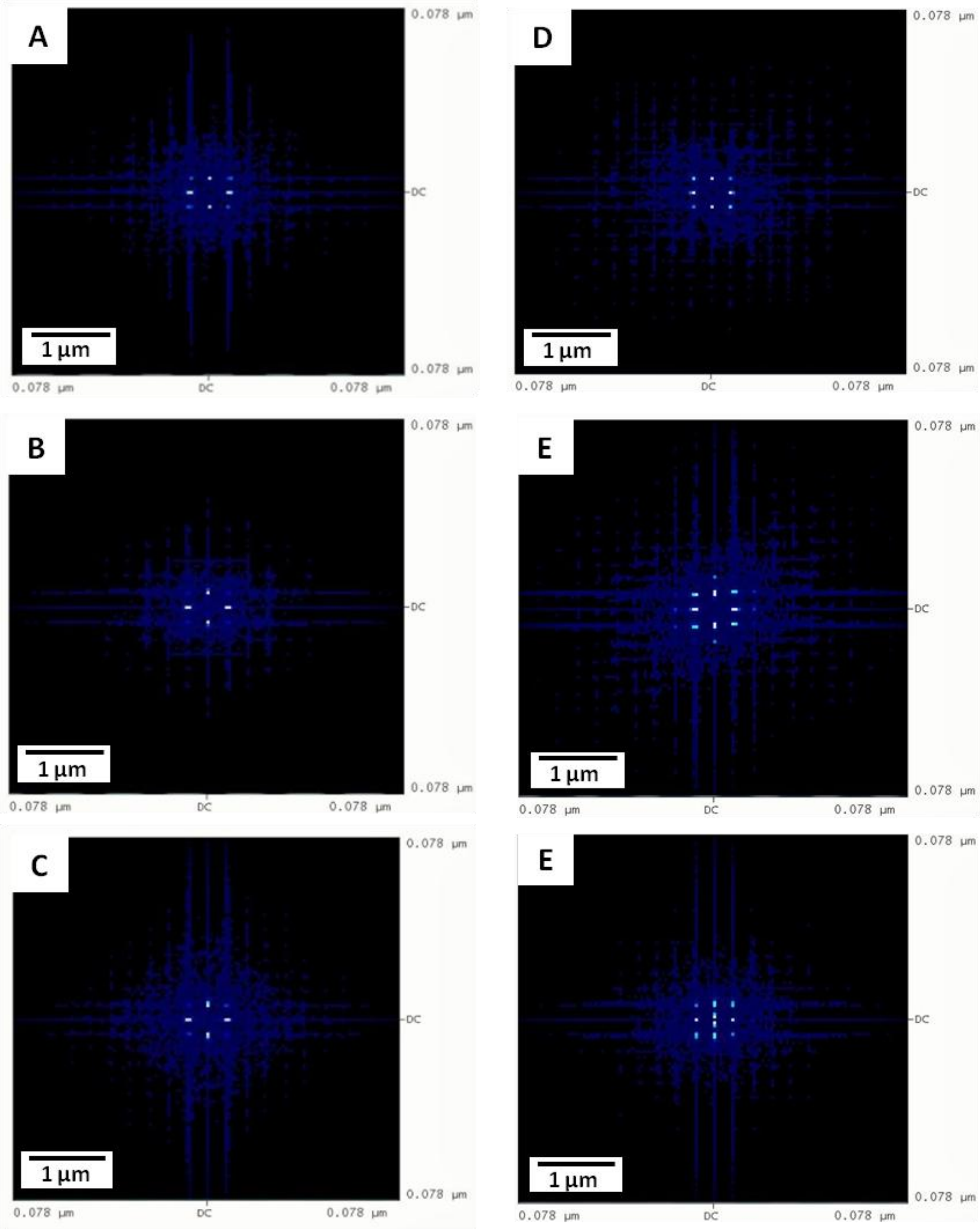

Figure 4.4: AFM 2D FFT images of (A) PS, (B) silk I, and (C) silk II porous frames, as well as (D) PS, (E) silk I, and (F) silk II pillar frames (5x5 µm^2).

To analyze the effect of secondary structure on the bottom thickness of the silk frames, a scratch test was conducted and the height from the silicon wafer to the bottommost area of the frame surface was recorded by again using AFM cross-sectional analysis. A negligible difference between the silk I and silk II frames existed, displaying the greater effect that the MeOH -induced transition had on secondary structure of the frame surface compared to the material bulk (Table 4.2). A possible explanation is the MeOH was unable to diffuse completely through the silk thickness, and the underlying bottom thickness did not undergo structural change. Further analysis to identify secondary structure present would be required for confirmation. From a different perspective, the possibility exists that the bottom bulk material experienced transition during deposition onto the silicon substrate due to mechanical strain. In this case, both silk I and silk II frames would already contain a silk II structured bottom material while the surface features remained different. The RMS of PS can be attributed to the nanoscale grainy morphology of the SU8 material surface, caused by the non-uniform photopolymerization during the IL process used for creation of the master mold[73], which was replicated onto the hard PS mold surface. Partial filling of surface features during silk deposition contributes to a more regular surface due to surface tension, and is displayed by RMS of silk I being lesser than PS (Table 4.2). A consistent trend of increased RMS resulted as silk I frames were transitioned to silk II. This result is expected based on previous studies[92], and can be explained by the rearrangement of protein strands and silk I surface dangling bonds to create β-sheets of silk II during crystallization resulting in the indicative grainy morphology.

Table 4.2: Bottom Thicknesses of Frames (Silk I & Silk II) and RMS Values of Frames and Negative Replicas (PDMS) for both Pillar and Porous Pattern Structures

patterned structure	template material	bottom thickness (nm)	roughness (nm)
pillar	PS	--	7.76
	silk I	165.47	7.18
	silk II	166.25	7.38
porous	PS	--	7.68
	silk I	150.58	4.84
	silk II	154.91	5.10

Optical microscopy was utilized for macroscale qualitative analysis of the pillar and porous patterned surfaces of PS, silk I, and silk II frames, and images are shown in Figure 4.5. The PS mold surface contained several cracks due to localized fluctuations in the degree of PS solution infiltration into the surface cavities of the PDMS inverse mold prior to polymerization. Differing amounts of material present during *in situ* polymerization would result in competition for nearby monomeric material between newly formed polymer chains, thus leading to internal stresses at the surface causing development of cracks. Silk I displayed a more uniform surface with minimal presence of cracks suggesting capillary force and surface tension, involved during deposition of silk solution and spin-casting, affected the silk solution greater than the PS solution and simple solution-casting. An increase of these associated forces experienced as the mold cavities are being filled would produce less strain on the silk as it conforms to the surface pattern, and thereby decrease the propensity for crack formation. Furthermore, the existence of voids on the surface can be attributed to such forces in combination with localized variability in the concentration of silk protein strands in proximity to the mold cavities. A lower concentration of protein strands in a certain region would cause cavity filling by water only which would then be removed by the shear force involved in spin-casting.

As discussed earlier, the rearrangement of protein strands as silk I transitions to silk II results in a decrease of free volume occupied. The optical image in Figure 4.5 of silk II reveals this mechanism through the appearance of a greatly increased amount of cracks and voids present on the frame surface. Moreover, the more uniform surface contrast correlates well with a more uniform material density versus silk I, as expected with a transition from a random coil structure to a crystalline ordering. Analysis of the optical images generated from the porous frames displayed a similar trend between the different materials utilized. However, the presence of cracks and voids were less apparent, providing further supportive evidence for the explanation that capillary force and surface tension play a lesser role during replication of the porous nanoscale features. The larger cavity area of the pillar surface pattern, not only facilitated generation of more closely resembled porous feature heights (Table 4.1), but also decreased the internal stresses within the deposited silk I frame.

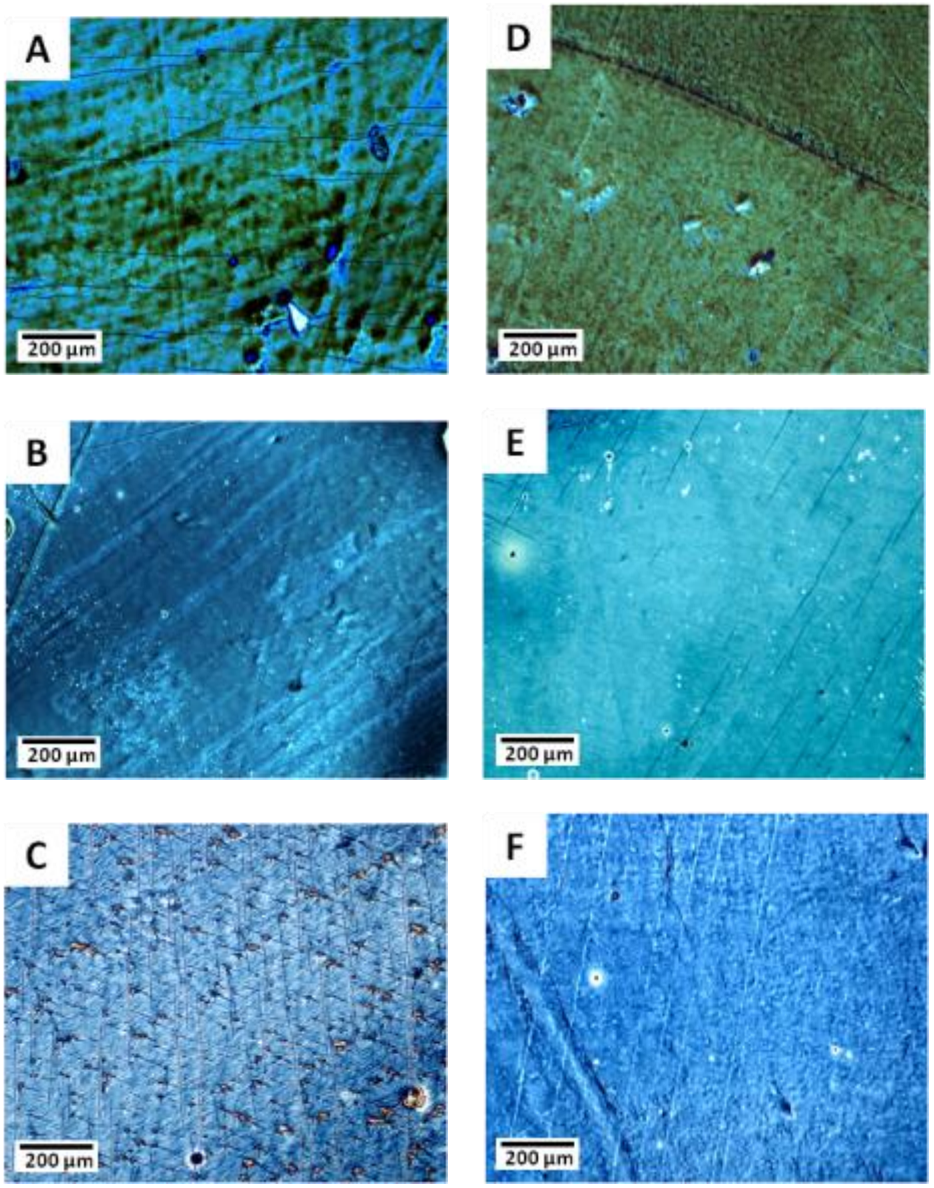

Figure 4.5: Optical microscopy images of (A) PS, (B) silk I, and (C) silk II pillar frames, as well as (D) PS, (E) silk I, and (F) silk II porous frames (1.2x1.2 mm^2).

4.2.3 Surface Mineralized Nanocomposite Frames

As mentioned earlier, the ability of silk to reduce GNPs has been previously shown as an effective route for obtaining organic-inorganic nanocomposites.[23,157] In order to increase understanding regarding this approach, both silk I and silk II frames were employed in this study for boundary organized biomineralization of GNPs. The tyrosine phenolic groups within silk protein strands, ionized at high pH, transfer electrons to the inorganic metal ion directly from solution resulting in metal reduction and adsorption of GNP nuclei.[157] In contrast to an earlier study[23], bioassisted mineralization of GNPs was conducted onto silk templates with patterned surface arrays of nanoscale features, rather than a planar film, for evaluation of the impact to aggregation state, nanoparticle size and surface coverage related to surface patterning. Furthermore, both silk I and silk II were utilized to study the effect of secondary structure on silk's reduction activity.

In the previous study[23], silk I and silk II films aided in successful biomineralization with agglomerated , larger diameter GNPs formed on the silk I surface, and more uniform, smaller particle size relating to the silk II surface. The presence of β-sheets in silk II, providing tyrosine ordering in the surface domains, was suggested to facilitate formation of individual GNPs, prevent agglomeration, and limit particle growth.[23] The capability of silk I to support biomineralization of GNPs directly from a 0.1 M $HAuCl_4$ / borate buffer solution was found to be greatly different in the study detailed here. Silk I frames transferred onto a silicon substrate and then immersed in a mixed solution of $HAuCl_4$ and borate buffer at pH 10.5 for 24 hours resulted in silk dissolution. Optical microscopy revealed degradation of the silk I structure to an extent where the surface pattern was no longer present, and in some regions silk I became completely detached (image not shown).

To develop understanding of this difference in findings, the variables between approaches were identified as the duration of silk I immersion in solution, 24 hours versus 10 hours, and the interface between silk I and its underlying substrate. Due to silk fibroin deposition occurring from aqueous solution, hydrophobic amino acids segregate towards the protein core of the randomly coiled polymer chains, thus resulting in hydrophilic residues located at the air-silk I interface.[92] An increased duration of exposure of these residues to the $HAuCl_4$ / borate buffer solution may allow for sufficient diffusion into the silk I surface necessary to develop swelling of the polymer chains to an extent of dissolution. Moreover, the frames' patterned arrays of nanoscale features greatly augments the surface area, as opposed to planar films, and enables multi-directional diffusion. The enhanced effect of diffusion experienced by the silk I frames, along with meta-stability of randomly coiled protein strands to water, is suggested as an explanation for the occurrence of silk dissolution. Another possible explanation is that the underlying substrate material in the previous study[23] was a 20-bilayer polystyrene sulfonate - polyanhydride (PSS-PAH) film, instead of a silicon oxide surface. Capillary-driven adhesion of silk frames to the Si substrate would most likely result in a lower interfacial strength compared to physically tethered polymer chains between the multilayer PSS-PAH film and the adsorbed silk I film. In order to preserve the silk I structure during biomineralization, the interfacial strength must be substantial enough to overcome the gain of entropy associated with polymer chains distancing themselves from the substrate surface as silk I swells in the $HAuCl_4$ / borate buffer solution. Since the transition to silk

II produces the formation of β-sheets and hydrophobic residues at the surface[92], the swelling effect is of negligible consideration and biomineralization with silk II frames was conducted successfully.

Boundary organized biomineralization of porous and pillar silk II frames resulted in fabrication of organic-inorganic bionanocomposites with patterned surfaces and preservation of the silk template. AFM imaging was used for characterization of GNP mineralized silk II frames and displayed that although the bi-directional periodicity of nanoscale features were unchanged, the local morphology of pattern features changes significantly (Figure 4.6). The organized tyrosine ordering in the surface of silk II, due to formation of beta-sheets, facilitated uniform distribution of GNPs and provided nanoscale protein surface domains for nucleation resulting in a limitation of nanoparticle growth and prevention of agglomeration. Appearance of less GNPs on the tops and sloped areas of pillars versus the pillar bases and surrounding matrix was discovered, in combination with less GNP surface coverage on pillars versus pores. The settling of GNPs after nucleation could explain this finding, and infers a physical mechanism involved with the difficulty of GNP formation on pillars compared to pores, or the decreased presence of tyrosine groups available for metal reduction at the surface of patterned features. The size of GNPs were analyzed *via* cross-sectional analysis, and heights of particles found on pillar features were plotted against those recorded for porous features (Figure 4.7). Difficulty was experienced while distinguishing between GNPs and surface microroughness in the height image, scanned using a triangular tip. A possible solution for future evaluation to utilize a colloidal tip allowing for easier differentiation. Statistical analysis to develop understanding of the relationships between particle growth rate and surface coverage to the number of days mineralized would be an area for further testing.

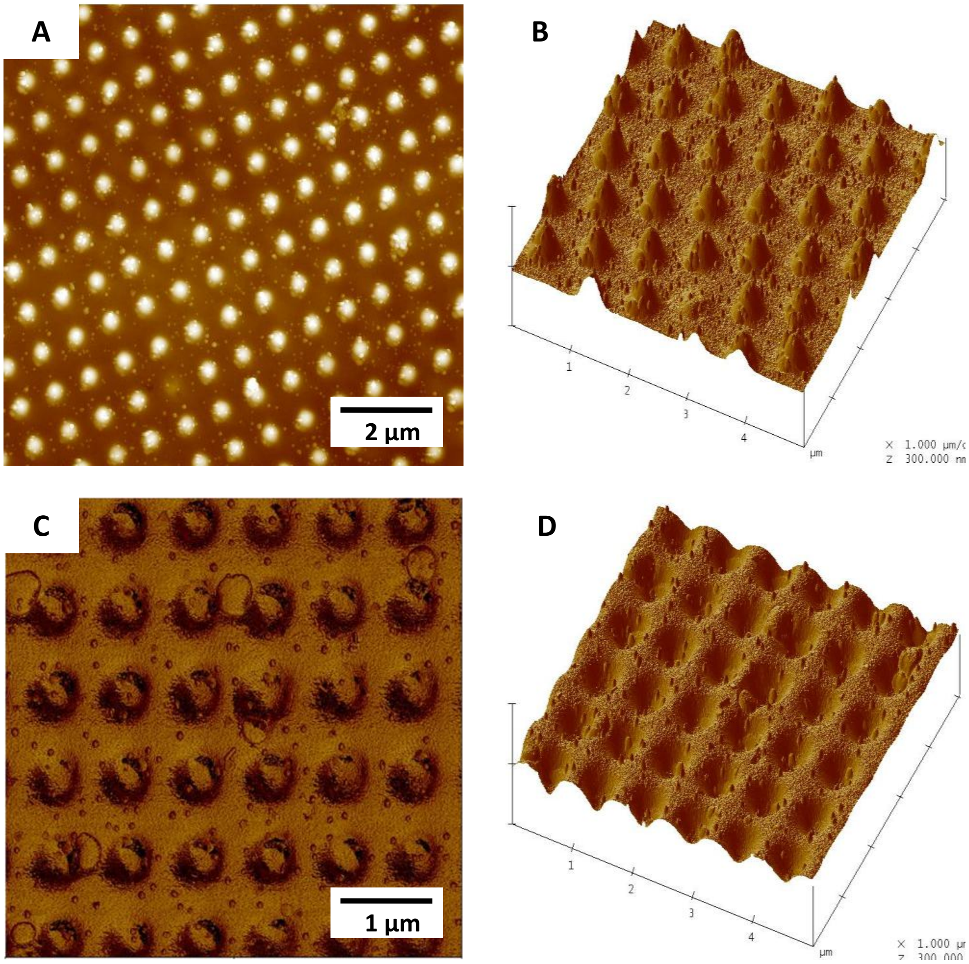

Figure 4.6: AFM topographical image (A) and 3D illuminated surface plot (B) of mineralized silk II pillar frame. AFM phase image (C) and 3D illuminated surface plot (D), of a mineralized silk II porous frame.

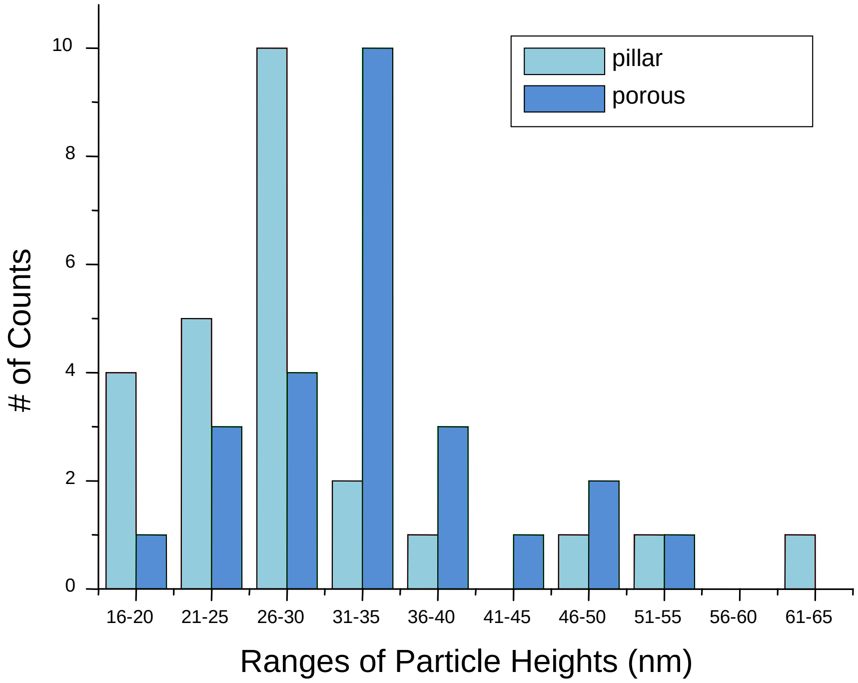

Figure 4.7: Statistical comparison of the particle heights found in pillar and porous structures.

4.3 Conclusions

In summary, spin-coating of aqueous silk solution was employed in conjunction with a soft lithography fabrication technique for allowance of simple and repeatable casting. This strategy exemplifies the ability to fabricate spatially patterned silk materials with regions that can be locally tuned for specific functionality. Furthermore, the silk protein ability to form complex secondary structures and undergo structural changes was utilized to evaluate the variation of bioenabled conditions for obtaining different types of nanostructures at ambient conditions. Replication of bi-directional pattern periodicity was maintained across long-range ordering (Figure 4.4), while microscale analysis showed slight deviation from one material to another (Table 4.1). Capillary forces and surface tension prevented complete filling of surface cavities, and led to differences in heights of nanoscale features present in the different materials used for frame construction. The transition from silk I to silk II also decreased heights of features as explained by the rearrangement of protein strands to adopt a crystalline structure composed of β-sheets. Such a finding provides the ability to tune silk's surface pattern via secondary structure, thus allowing for potential application in stimulus detection. Moreover, if the fabrication approach is implemented for a material with a reversible transition, then repeatable detection could be achieved.

The use of silk frames for boundary organized biomineralization was also achieved for growth of GNPs onto a patterned silk II surface. Investigation into the reasoning why silk I biomineralization was not successful led to increased understanding of the roles that hydrophilic residues and nanoscale features have on diffusion and swelling of silk protein strands, as well as, the impact of surface interaction between the underlying substrate material which silk is deposited onto. Biomineralization of GNPs, using a silk II template and the chosen fabrication approach allowed for preservation of the native template of organized, predetermined structure. This approach is highly suitable for designing functional organic-inorganic bionanocomposites with patterned surface arrays for enhancement of mechanical, optical, electrical, and biological properties of the native template material. Moreover, the approach 1) can be easily expanded to a wide variety of microstructures, 2) allows for implementation of biological macromolecules, non-planar structures, and sub-µm features, and 3) provides a route that is simple, robust, nontoxic, cost-effective, and completed at ambient conditions.

Increased understanding of the mechanism of boundary organized biomineralization on tailored surfaces compared to in solution will assist in development of general procedures for controlled bioenabled metal mineralization on template surfaces as well as bulk solutions. In this study, frames obtained with one set of specific parameters were generated to decrease the number of associated variables, allowing for focus on involved mechanisms. Modification of spin-coating conditions, such as silk solution concentration, spin speed, and time, would allow for investigation into how such parameters affect thickness, RMS, surface periodicity, and morphology of nanoscale features. Other possible further work includes statistical analysis for determination of GNP diameter and surface coverage dependent on mineralization time. Also, evaluation of mechanical properties of silk frames mineralized with GNPs could be conducted through utilization of AFM force-volume measurements. The approach detailed here allows for direct modification of surface properties via surface patterning and biomineralization, and provides a basis for development of novel bottom-up fabrication techniques to achieve enhancement of surface properties.

4.4 Experimental Section

4.4.1 Reconstituted Silk Fibroin Solution

For all experiments, 18.2 MΩ·cm Nanopure water was utilized. Silk was obtained from *Bombyx mori* silkworms raised on a diet of Silkworm Chow (Mullberry Farms, Fallbrook, CA). Live pupae were extracted from the cocoons prior to sericin removal. Cocoons were boiled for 30 min in an aqueous solution of 0.02 M Na_2CO_3 and then rinsed thoroughly with distilled water to extract the glue-like sericin proteins. The extracted silk fibroin was then dissolved in 9.3 M LiBr solution at 60 °C for 4 h, yielding a 20% (w/v) solution. The solution was dialyzed against distilled water using Slide-a-Lyzer dialysis cassettes (Pierce, MWCO 3500) at room temperature for 3 days to remove the LiBr. After dialysis, the solution was centrifuged three times, each at 20 °C for 20 min, to remove impurities and the aggregates that occurred during dialysis. The final concentration of aqueous fibroin solution was 8.0% w/v, which was determined by weighing the remaining solid after drying. This solution was then diluted to obtain the desired 3.0% (w/v) silk concentration used for solution deposition.

4.4.2 Fabrication of Patterned Molds

2D patterned templates comprised of Epon-SU8 (Miller Stephensen) as a photoresist were previously fabricated using multibeam IL according to the usual procedure.[158] Creation of the PS molds was conducted during an earlier study[73], and involved the preparation of a negative PDMS replica, infiltration of the PS solution into the surface cavities of PDMS, in situ polymerization of PS, and transferring the PS structure onto a silicon substrate. For fabrication of the PDMS molds a mixture of pre-polymer and curing agent (10:1) was poured onto the PS 2D structure, followed by vacuum degassing, to remove trapped air bubbles in the liquid and microchannels, and curing in a furnace at 60 °C for 4 hours. Subsequently, the PDMS was cut along the silicon wafer edge with a razor blade and peeled from the PS to create a negative replica of the organized porous and pillar structures.

4.4.3 Silk Deposition

PDMS stamps with channels fabricated from patterned masters were used as micromolds for creating patterned silk films. Prior to silk deposition, the PDMS stamps were sonicate in toulene for 2 min to remove residual organic material on the patterned surface and left to air-dry overnight. The spin-coating deposition method was performed by dropping silk solution onto the top of the PDMS mold, followed by rotating for 60 s at 3000 rpm on a spin-coater (Laurell Technologies). The silk frames were then released from the PDMS mold via conformational contact with a silicon substrate and pressed for 1 min, per usual procedure.[42] Silicon substrates were pre-cleaned with concentrated sulfuric acid (98%) and NOCHROMIX powder (GODAX Laboratories, Inc.), rinsed with Nanopure water, and dried with a stream of N_2 before silk frame transfer. Several silk frames were submerged in MeOH for 10 min to induce secondary structure transition to silk II, resulting in crystallization of the silk frames.

4.4.4 Mineralization

GNP mineralization onto silk II patterned frames was conducted at room temperature by immersing the silk frames into a mixed solution composed of 33 µL of 0.1 M $HAuCl_4$ and 2 mL of 0.1 M borate buffer at pH 10.5 for 24 h followed by extensive rinsing with Nanopure water.

3.4.5 Film Characterization

The morphology of the pristine silk films, as well as the GNP biofunctionalized silk II structures, was characterized with a Dimension 3000 AFM instrument with a Nanoscope IIIa controller (Digital Instruments). AFM imaging was performed in air with a light tapping mode using silicon triangular cantilevers (MikroMasch) consisting of a spring constant of 50 N/m according to the established procedure.[109,110] Field-emission SEM with a LEO 1530 instrument was used for further qualitative investigation of the frames' surface structure. The optical images were captured with a Leica MZ16 microscope in reflection mode.

CHAPTER V

GENERAL DISCUSSION

In summary, freely standing ultrathin nanocomposite membranes with remarkable mechanical properties were generated by using a novel single-solution assembly approach (Chapter II). In contrast to traditional LbL, the approach introduced is (1) simpler, (2) more efficient, and (3) affords the assembly of homogeneous dispersions resulting in significantly reinforced composites. The reinforced nanomaterials were obtained by integrating silica nanoparticles with POSS nanoparticles or clay MMT nanoplatelets with silk matrices which were premixed with a cross-linking agent. It was found that covalent cross-linking induced silk crystallization into β-sheet domains, the effect previously found for dehydrated silk films as a result of formation of physical cross-links between neighboring silk segments. Structural control of the silk protein, gained through cross-links and β-sheets, provided a reinforced microstructure. Silk membranes reinforced with POSS and MMT using the SA-LbL one-step mixed solution route led to enhanced mechanical properties as compared to traditional silk-based nanocomposites reported previously.[22] Up to 6-fold and 8-fold increase in elastic modulus and toughness, respectively, were found for these nanocomposites (Table 2.2). In contrast, traditional LbL-assembled nanocomposites showed only a 3-fold increase in mechanical strength.

The properties of the composites are attributed to the strong inter- and intramolecular interactions induced by physical and chemical cross-linking resulting in crystallization, and to the excellent dispersion of nanofiller particles in the silk matrix. A computational analysis of the reinforcing phenomena, applied recently by Buehler *et al*. to the spider silk crystallization[159], could be one of the future directions to elaborate on the work detailed in Chapter II. The facile and simplified fabrication method with the pre-cross-linked silk matrix can be further tailored by applying different assembly conditions and incorporating inorganic moieties of various functionalities into the silk matrix to obtain thin films with unique properties. The combination of enhanced mechanical and good optical properties suggests the perspective utility of the silk-based nanocomposites as inexpensive, nontoxic, and easily scalable reinforced biomaterials to meet demanding applications with mechanical robustness and optical transparency requirements.

NR measurements of ultrathin films (5 and 27 nm) composed of *Bombyx mori* silk fibroin protein were utilized to obtain internal structuring information along the surface normal (Chapter III). Reconstituted aqueous silk solution (0.2% w/v) deposited on a silicon substrate using the SA-LbL technique resulted in a vertically segregated film displaying two different regions of SLD indicating different secondary structures of silk monolayers in direct contact with the inorganic surface. The result reveals that silk has a denser structure in the proximity to substrate (below 5-7 nm) which can be associated with the interfacial crystallization in β-sheet form and preserves random coil secondary structure for following monolayers. Such a vertically segregated structure of solid silk molecular films defined their complex non-uniform swelling behavior with interfacial layer becoming fully swellable (about 70% of water) only for thickness above 7-10 nm. Even for a solid silk monolayer with an initial thickness of 5 nm the non-uniform swelling resulted in the formation of two-tier swollen layer with about the 5 nm topmost layer swollen by 45%. These features are important to understand and control in the context of the function of silk-based biomaterials and devices.

Reconstituted aqueous silk solution deposited on a silicon substrate using the SA-LbL technique resulted in a monolayer silk film composed of random nanofibrils with constant SLD. However, a vertically segregated ordering with two different regions was observed in dry, thicker, seven-layer SA-LbL silk films. The vertical segregation of silk multilayer films indicates the presence of a different secondary structure of silk in direct contact with the silicon oxide surface (first 6 nm). The layered structure can be attributed to interfacial β-sheet crystallization and the formation of well-developed nanofibrillar nanoporous morphology for the initially deposited silk surface layers with the preservation of less dense, random coil secondary structure for the layers that follow (Table 3.2). This segregated structure of solid silk films defines their complex non-uniform behaviour in the D_2O environment with thicker silk films undergoing delamination during swelling. For a silk monolayer with an initial thickness of 6 nm, the increase in the effective thickness by 60% combined with surprising decrease in density was observed. Considering the nanoporous morphology of the hydrophobic silk layer, a suggestion was given that the apparent increase in its thickness in liquid environment is caused by the air nanobubble trapping phenomenon at the liquid-solid interface (Figure 3.8). These studies indicate complex layering of silk in contact with silicon oxide surfaces in both dry and hydrated environments which have never been observed in earlier studies and can be critical for processing and design of silk-filler interfaces in composite biomaterials.

In Chapter IV, unification of aqueous silk solution, spin-casting deposition, soft lithography pattern replication, and bioenabled mineralization of GNPs was utilized to fabricate silk-based films with tailored surface topography. These surface patterned films, denoted as frames, were also characterized *via* AFM imaging, SEM imaging, and optical microscopy for qualitative analysis; as well as, AFM cross-sectional analysis and 2D FFT imaging for quantitative determination of pattern periodicity and dimensions of nanoscale features. The implementation of various patterned constructs increases the range of possibilities for specific and localized control of properties. For example, creation of aperiodic nanopatterned lattices could lead to increased sensitivity for biological sensors or varying degrees of cellular regeneration kinetics within the same tissue scaffold.[11] Future applications for such structures include substrates for cell culture, biomedical-related diffractive optics and optical interfaces, and different mechanistic sensors (i.e. thermal, biological, chemical, and optical). Moreover, functionalization of patterned silk templates *via* incorporation of various composite materials can further expand their scope and value. Patterned silk films were exploited for boundary organized mineralization of inorganic GNPs with specific emphasis placed on the effects of nanopatterning on the selected mineralization technique. The coupling of these entities with silk fibroin matrices allows for the production of functionalized surfaces that can subsequently be characterized to analyze their value for prospective application in areas such as optical sensing and tissue engineering. Incorporation of these entities within the bulk of the material could also be explored by mixing them into the aqueous silk solution prior to film fabrication, similar to the mixed solution route detailed in Chapter II.

A PDMS mold in conjunction with a metal mask for use in patterning both the top and bottom surfaces of a film is one possible approach towards broadening the scope of knowledge related to patterning of freely standing templates. Composite construction through directed assembly of both porous and planar silk films has allowed for construction of lamellae-like, 3D tissue scaffolds[11], and introduction of nanopatterned features could increase the control of desired properties. The method of creating nanoscale features onto silk films, presented in Chapter IV, could be further expanded for the study of surface topography's effect on cell behavior. Further research that may be of value lies within the combination of surface patterning with coupling of bioactive molecules to the silk surface in order to increase control of material-cell interactions, thus imparting a tailored biomaterials approach for implantable medical devices. Labile cell-signaling molecules can be utilized within the cellular scaffold allowing for the study of migration, mobility, morphology, and other various cell functions important to cellular regeneration.[11] Such an approach would enable monitoring of cellular behavior as a function of the patterned scaffold. Surface modification of silk fibroin biomaterials can be implemented to alter cell attachment and impact cell proliferation, and chemical modifications through amino acid side chains can be undergone to adjust surface properties or to immobilize cellular growth factors.[10] An advantage of silk that has yet to be fully explored is within the ability to easily tailor its degradation behavior through the chosen mode of processing.[65] A better understanding of the involvement of silk matrices in specific cell and tissue environments will provide essential insight into how to optimize material-cell interaction.[65]

Comprehensively, the chapters within this paper revolve around the central theme of silk secondary structures and developing understanding of the relationships between associated variables (i.e. fabrication approach, addition of inorganic nanoparticles, introduction of patterned features). Chapter II focuses on incorporation of reinforcing nanoparticles within silk membranes, and a novel one-step single solution assembly approach was implemented for bottom-up fabrication of ultrathin freely standing silk-based nanocomposite membranes. Mechanical properties of these nanocomposite membranes were significantly enhanced, as compared to those fabricated *via* conventional SA-LbL deposition, by premixing composite components to improve solubility and compatibility of the silk and inorganic materials, combined with concurrent covalent cross-linking to induce silk crystallization into β-sheet domains. Deposited in a single step, this combination of reinforcing nanoparticles dispersed homogenously within more mechanically robust crystalline silk secondary structure also provides a simpler and more efficient approach for nanoscale control of structural organization that can be easily scaled-up to higher film thicknesses.

In Chapter III, NR measurements were used for the first time to investigate details regarding the internal structure of SA-LbL deposited silk films in the direction along the surface normal, and to chart the swelling behavior of silk films in liquid after tethering to an interface. Results revealed a vertically segregated film with different secondary structures of silk due to direct influence of the silicon oxide surface on interfacial crystallization and nanofibrillization of the initially deposited silk monolayer, versus additional silk layers assembled with less dense random morphologies far from the interface. These studies indicate complex layering of silk in contact with silicon oxide surfaces in both dry and hydrated environments which have never been observed in earlier studies, and can be critical for processing and design of silk-filler interfaces in composite biomaterials. Construction of a novel material system was achieved in Chapter IV through combination of template patterning and boundary organized surface mineralization. The approach can be easily expanded to a wide variety of microstructures, allows for implementation of biological macromolecules, non-planar structures, and sub-μm features, and provides a route that is simple, robust, nontoxic, cost-effective, and completed at ambient conditions. Moreover, the approach allows for direct modification of surface properties and provides a basis for development of novel bottom-up fabrication techniques to achieve enhancement of surface properties.

APPENDIX A

LIST OF PUBLICATIONS AND PRESENTATIONS

A.1 Publications

[A.1.1] Wallet, B., Kharlampieva, E., Campbell-Proszowska, K., Kozlovskaya, V., Malak, S., Ankner, J.F., and Tsukruk, V.V., "Silk Layering as Studied with Neutron Reflectivity", Langmuir 28, 11481 (2012).

[A.1.2] Kharlampieva, E., Kozlovskaya, V., Wallet, B., Shevchenko, V.V., Naik, R.R., Vaia, R., Kaplan, D.L., and Tsukruk, V.V., "Co-cross-linking Silk Matrices with Silica Nanostructures for Robust Ultrathin Nanocomposites", ACS Nano 4, 7053 (2010).

A.2 Presentations

[A.2.1] Wallet, B., Kharlampieva, E., and Tsukruk, V.V., "Nanostructured Interfaces of Optically Transparent, Biocompatible Silk Fibroin Frames" 2010 Nanotechnology for Defense Conference, Atlanta, GA (2010).

REFERENCES

---

[1] Brutchey, R.L., and Morse, D.E., Chem. Rev. 108, 4915 (2008).

[2] Dickerson, M.B., Sandhage, K.H., and Naik, R.R., Chem. Rev. 108, 4935 (2008).

[3] Lewis, R., Chem. Rev. 106, 3762 (2006).

[4] Hammond, P., Adv. Mater. 16, 1271 (2004).

[5] Jiang, C., Markutsya, S., Shulha, H., and Tsukruk, V.V., Adv. Mater. 17, 1669 (2005).

[6] Kharlampieva, E., Slocik, J.M., Singamaneni, S., Poulsen, N., Kroger, N., Naik, R.R., and Tsukruk, V.V., Adv. Funct. Mater. 19, 2303 (2009).

[7] Buehler, M.J., and Yung, Y.C., Nature Mater. 8, 175 (2009).

[8] Lawrence, B.D., Cronin-Golomb, M., Georgakoudi, I., Kaplan, D.L., and Omenetto, F.G., Biomacromolecules 9, 1214 (2008).

[9] Perry, H., Gopinath, A., Kaplan, D.L., Dal Negro, L., and Omenetto, F.G., Adv. Mater. 20, 3070 (2008).

[10] Vepari, C., and Kaplan, D.K., Prog. Polm. Sci. 32, 991 (2007).

[11] Lawrence, B.D., Merchant, J.K., Pindrus, M.A., Omenetto, F.G., and Kaplan, D.K., Biomaterials 30, 1299 (2009).

[12] Li, C., and Kaplan, D.L., Curr. Opin. Solid. State. Mater. Sci. 7, 265 (2003).

[13] Heim, M., Keerl, D., and Scheibel, T., Angew. Chem. 48, 2 (2009).

[14] Vasconcelos, A., Freddi, G., and Cavaco-Paulo, A., Biomacromolecules 9, 1299 (2008).

[15] Arai, T., Freddi, G., Innocenti, R., and Tsukada, M., Journal of Applied Polymer Science 91, 2383 (2004).

[16] Bettinger, C. J., Cyr, K.M., Matsumoto, A., Langer, R., Borenstein, J.T., and Kaplan, D.L., Adv. Mater. 19, 2847 (2007).

[17] Amsden, J. J., Perry, H., Boriskina, S.V., Gopinath, A., Kaplan, D.K., Dal Negro, L., and Omenetto, F.G., Optics Express 17, 21271 (2009).

[18] Liu, Y., Liu, H., Qian, J., Deng, J., and Yu, T., Fresenius J Anal Chem 355, 78 (1996).

[19] Yu, T., Liu, H., Deng, J., and Liu, Y., Journal of Applied Polymer Science 58, 973 (1995).

[20] Zhang, Y-Q., Biotechnology Advances 16, 961 (1998).

[21] Shulha, H., Foo, C.W.P., Kaplan, D.L., and Tsukruk, V.V., Polymer 47, 5821 (2006).

[22] Jiang, C., Wang, X., Gunawidjaja, R., Lin, Y.-H., Gupta, M.K., Kaplan, D.L., Naik, R.R., and Tsukruk, V.V., Adv. Funct. Mater. 17, 2229 (2007).

[23] Kharlampieva, E., Zimnitsky, D., Gupta, M., Bergman, K.N., Kaplan, D.L., Naik, R.R., and Tsukruk, V. V., Chem. Mater. 21, 2696 (2009).

[24] Blond, D., McCarthy, D.N., Blau, W.J., and Coleman, J.N., Biomacromolecules 8, 3973 (2007).

[25] Lee, S.-M., Pippel, E., Gösele, U., Dresbach, C., Qin, Y., Chandran, C.V., Bruniger, T., Hause, G., and Knez, M., Science 324, 488 (2009).

---

[26] Omenetto, F.G., and Kaplan, D.L., Nat. Photon. 2, 641 (2008).

[27] Caseri, W., Macromol. Rapid Commun. 21, 705 (2000).

[28] Kyprianidou-Leodidou, T., Margraf, P., Caseri, W., Suter, U.W., and Walther, P., Polym. Adv. Technol. 8, 505 (1997).

[29] Kharlampieva, E., Tsukruk, T., Slocik, J.M., Ko, H., Poulsen, N., Naik, R.R., Kroger, N., and Tsukruk, V.T., Adv. Mater. 1, 9999 (2008).

[30] Shchepelina, O., Drachuk, I., Gupta, M.K., Lin, J., and Tsukruk, V.V., Adv. Mater. 23, 4655 (2011).

[31] Martel, A., Burghammer, M., Davies, R.J., Cola, E.D., Vendrely, C., and Riekel, C., J. Am. Chem. Soc. 130, 17070 (2008).

[32] Jin, H., and Kaplan, D., Nature 424, 1057 (2003).

[33] Zhu, J., Zhang, Y., Shao, H., and Hu, X., Polymer 49, 2880 (2008).

[34] Chen, X., Shao, Z., Knight, D., and Vollrath, F., Proteins: Struct., Funct., Bioinf. 68, 223 (2007).

[35] Martel, A., Burghammer, M., Davies, R., and Cola, R.D,. Biomicrofluidics 2, 024104 (2008).

[36] Zhu, Z.H., Ohgo, K., and Asakura, T., eXPRESS Polm. Lett. 2, 885 (2008).

[37] Ye, C., Shchepelina, O., Calabrese, R., Drachuk, I., Kaplan, D.L., and Tsukruk, V.V. Biomacromolecules 12, 4319 (2011).

[38] Nogueira, G.M., Swiston, A.J., Beppu, M.M., and Rubner, M.F., Langmuir 26, 8953 (2010).

---

[39] Meinel, L., Hofmann, S., Karageorgiou, V., Kirker-Head, C., McCool, J., Gronowicz, G., Zichner, L., Langer, R.,Vunjak-Novakovic, G., and Kaplan, D.K., Biomaterials 26, 147 (2005).

[40] Kearns, V., MacIntosh, A., Crawford, A., and Hatton, P.V., "Silk-based Biomaterials for Tissue Engineering. Topics in Tissue Engineering", Vol. 4, Chap 1 (2008).

[41] Unger, R.E., Wolf, M., Peters, K., Motta, A., Migliaresi, C., and Kirkpatrick, C.J., Biomaterials 25, 1069 (2004).

[42] Gupta, M.K., Khokhar, S.K., Phillips, D.M., Sowards, L.A., Drummy, L.F., Kadakia, M.P., and Naik, R.R., Langmuir 23, 1315 (2007).

[43] Liu, T.-L., Miao, J.-C., Sheng, W.-H., Xie, Y.-F., Huang, Q., Shan, Y.-B., and Yang, J.-C., Biomed. & Biotechnol. 11, 10 (2010).

[44] Lu, S., Wang, X., Lu, Q., Hu, X., Uppal, N., Omenetto, F.G., and Kaplan, D.K., Biomacromolecules 10, 1032 (2009).

[45] Makaya, K., Terada, S., Ohgo, K., and Asakura, T., Journal of Bioscience and Bioengineering 108, 68 (2009).

[46] Dey, D., Islam, M.N., Hussain, S.A., and Bhattacharjee, D., Int. J. of Pure and App. Sci. 4, 39 (2008).

[47] Zamarreno, C.R., Goicoechea, J., Matias, I.R., and Arregui, F.J., Thin Solid Films 517, 3776 (2009).

[48] Decher, G., and Hong, J.D., Int. J. Phys. Chem. 95, 1430 (1991).

[49] Stuart, M.C., Huck, W., Genzer, J., Müller, M., Ober, C., Stamm, M., Sukhorukov, G., Szleifer, I., Tsukruk, V.V., Urban, M., Winnik, F., Zauscher, S., Luzinov, I., and Minko, S., Nat. Mater. 9, 101 (2010).

[50] Jiang, C., and Tsukruk, V. V., Adv. Mater. 18, 829 (2006).

---

[51] Markutskaya, S., Jiang, C., Pikus, Y., and Tsukruk, V.V., Adv. Funct. Mater. 15, 771 (2005).

[52] Cho, J., Char, K., Hong, J.-D., and Lee, K.-B., Adv. Mater. 13, 1076 (2001).

[53] Lutkenhaus, J., and Hammond, P., Soft Matter 3, 804 (2007).

[54] Decher, G., and Schlenoff, J.B., "Multilayer Thin Films: Sequential Assembly of Nanocomposite Materials", Wiley-VCH (2002).

[55] Hiller, J.A., Mendelsohn, J.D., and Rubner, M.F., Nature Mater. 1, 59 (2002).

[56] Schlenoff, J.B., Rmaile, A.H., and Bucur, C.B.J,. Am. Chem. Soc. 130, 13589 (2008).

[57] Lvov, Y., Decher, G., and Möhwald, H., Langmuir 9, 481 (1993).

[58] Lvov, Y., Ariga, K., Ichinose, I., and Kunitake, T., Langmuir 12, 3038 (1996).

[59] Kharlampieva, E., Kozlovskaya, V., Gunawidjaia, R., Shevchenko, V.V., Kaplan, D., Vaia, R., Naik, R.R., and Tsukruk, V. V., Adv. Funct. Mater. 20, 840 (2010).

[60] Xu, M., and Lewis, R.V., Proc. Natl. Acad. Sci. U.S.A. 87, 7120 (1990).

[61] Drummy, L.F., Phillips, D.M., Stone, M.O., Farmer, B.L., and Naik, R.R., Biomacromolecules 6, 3328 (2005).

[62] Ki, C.S., Um, I.C., and Park, Y.H., Polymer 50, 4618 (2009).

[63] Yano, Y.F., Uruga, T., Tanida, H., Terada, Y., Takagaki, M., and Yamada, H., Langmuir 25, 32 (2009).

[64] Sohn, S., Strey, H.H., and Gido, S.P., Biomacromolecules 5, 751 (2004).

[65] Georgakoudi, I., Tsai, I., Greiner, C., Wong, C., DeFelice, J., and Kaplan, D., Optics Express 15, 1043 (2007).

[66] Valluzzi, R., Gido, S.P., Muller, W., and Kaplan, D.L., Intl. J. Bio. Macro. 24, 237 (1999).

[67] Valluzzi, R., He, S.J., Gido, S.P., and Kaplan, D., Intl. J. Bio. Macro. 24, 227 (1999).

[68] Kharlampieva, E., Slocik, J.M., Tsukruk, T., Naik, R.R., and Tsukruk, V.V., Chem. Mater. 20, 5822 (2008).

[69] Anderson, K.D., Slocik, J.M., McConney, M.E., Enlow, J.O., Jakubiak, R., Bunning, T.J., Naik, R.R., and Tsukruk, V.V., Small 5, 741 (2009).

[70] Martinez-Otero, A., Evangelio, E., Alibes, R., Bourdelande, J.L., Ruiz-Molina, D., Busque, F., and Hernando, J., Langmuir 24, 2963 (2008).

[71] Parker, S. T., Domachuk, P., Amsden, J., Bressner, J., Lewis, J.A., Kaplan, D.L., and Omenetto, F.G., Adv. Mater. 21, 2411 (2009).

[72] Gupta, M., Singamaneni, S., McConney, M., Drummy, L.F., Naik, R.R., and Tsukruk, V.V., Adv. Mater. 22, 115 (2010).

[73] Singamaneni, S., Chang, S., Jang, J.-H., Davis, W., Thomas, E.L., and Tsukruk, V.V., Phys. Chem. Chem. Phys. 10, 4093 (2008).

[74] Xu, T., Zhang, N., Nichols, H.L., Shi, D., and Wen, X., Materials Science and Engineering 15, 1043 (2007).

[75] Su, W.-T., Chu, I.-M., Yang, J.-Y., and Lin, C.-D., Micron 37, 699 (2006).

[76] Gupta, S., Hunter, M., Cebe, P., Levitt, J.M., Kaplan, D.L., and Georgakoudi, I. Biomaterials 29, 2359 (2008).

[77] Anderson, K.D., Marczewski, K., Singamaneni, S., Slocik, J.M., Jakubiak, R., Naik, R.R., Bunning, T.J., and Tsukruk, V.V., ACS Appl. Mater. Interfaces 2, 2269–2281 (2010).

[78] Zhai, L., Cebeci, F.C., Cohen, R.E., and Rubner, M.F., Nano Lett. 4, 1349 (2004).

[79] Bavykin, D., Friedrich, J., and Walsh, F., Adv. Mater. 18, 2807 (2006).

[80] Warwicker, J.O., Acta. Cryst. 7, 565 (1954).

[81] Singamaneni, S., Kharlampieva, E., Jang, J.-H., McConney, M.E., Jiang, H., Bunning T.J., Thomas E.L, and Tsukruk V.V., Adv. Mater. 22, 1369 (2010).

[82] Kharlampieva, E., Jung, C.M., Kozlovskaya, V., and Tsukruk, V.V., J. Mater. Chem. 20, 5242 (2010).

[83] Bhawalker, S.P., Qian, J., Heiber, M.C., and Jia, L., Langmuir 26, 16662 (2010).

[84] Podsiadlo, P., Michel, M., Critchley, K., Srivastava, S., Qin, M., Lee, J.W., Verploegen, E., Hart, A.J., Qi, Y., and Kotov, N.A., Angew. Chem. 48, 7073 (2009).

[85] Lvov, Y.M., Shchukin, D.G., Möhwald, H., and Price, R. R., ACS Nano 2, 814 (2008).

[86] Tang, Z., Kotov, N.A., Magonov, S., and Ozturk, B., Nat. Mater. 2, 413 (2003).

[87] Pescarmona, P.P., and Maschmeyer, T., J. Chem. 54, 583 (2001).

[88] Wu, J., and Mather, J. Macromol. Sci. Part C 49, 25 (2009).

[89] Gunawidjaja, R., Huang, F., Gumenna, M., Klimenko, N., Nunnery, G.A., Shevchenko, V., Tannenbaum, R., and Tsukruk, V.V., Langmuir 25, 1196 (2009).

[90] Carroll, J.B., Waddon, A.J., Nakade, H., and Rotello, V.M., Macromolecules 36, 6289 (2003).

[91] Iacono, S.T., Budy, S.M., Mabry, J.M., and Smith, D.W. Jr., Macromolecules 40, 9517 (2007).

[92] Drummy, L.F., Koerner, H., Farmer, K., Tan, A., Farmer, B.L., and Vaia, R.A., J. Phys. Chem. B 109, 17868 (2005).

[93] Jiang, C., Singamaneni, S., Merrick, E., and Tsukruk, V.V., Nano Lett. 6, 2254 (2006).

[94] Nolte, A.J., Rubner, M.F., and Cohen, R.E., Macromolecules 38, 5367 (2005).

[95] Dicko, C., Knight, D., Kenney, J., and Vollrath, F., Biomacromolecules 5, 2105 (2004).

[96] Hermanson, K., Huemmerich, D., Scheibel, T., and Bausch, A.R., Adv. Mater. 19, 1810 (2007).

[97] Tong, W., Gao, C., and Möhwald, H., Macromol. Rapid Commun. 27, 2078 (2006).

[98] Beall, G.W., Sowersby, D.S., Roberts, R.D., Robson, M.H., and Lewis, L.K., Biomacromolecules 10, 105 (2009).

[99] Kopesky, E.T., Haddad, T.S., McKinley, G.H., and Cohen, R.E., Polymer 46, 4743 (2005).

[100] Lewin, M., and Pearce, E., "Handbook of Fiber Chemistry", Marcel Dekker Vol. 15, 415 (1998).

[101] Tajima, F., J. Insect Biotechnol. Sericol. 73, 85 (2004).

[102] Rousseau, M.-E., Beaulieu, L., Lefèvre, T., Paradis, J., Asakura, T., and Pèzolet, M., Biomacromolecules 7, 2512 (2006).

[103] Silva, S.S., Motta, A., Rodrigues, M.T., Pinheiro, A.F.M., Gomes, M.E., Mano, J.F., Reis, R.L., and Migliaresi, C., Biomacromolecules 9, 2764 (2008).

[104] Podsiadlo, P., Kaushik, A.K., Arruda, E.M., Waas, A.M., Shim, B.S., Xu, J., Nandivada, H., Pumplin, B.G., Lahann, J., Ramamoorthy, A., and Kotov, N.A., Science 318, 80 (2007).

[105]Keten, S., Xu, Z., Ihle, B., and Buehler, M.J., Nat. Mater. 9, 359 (2010).

[106] Manevitch, O.L., Rutledge, G.C., J. Phys. Chem. B 108, 1428 (2004).

[107] Sofia, S., McCarthy, M.B., Gronowicz, G., and Kaplan, D.L., J. Biomed. Mater. Res. 54, 139 (2001).

[108] Tereshchenko, T.A., Shevchuk, A.V., Shevchenko, V.V., Snegir, S.V., and Pokrovskii, V.A., Polym. Sci. 48, 1248 (2006).

[109] McConney, M.E., Singamaneni, S., and Tsukruk, V.V., Polym. Rev. 50, 235 (2010).

[110] V.V. Tsukruk, Rubber Chem. Technol. 70, 430 (1997).

[111] Jiang, H., Johnson, W.E., Grant, J.T., Eyink, K., Johnson, E.M., Tomlin, D.W., and Bunning, T.J., Chem. Mater. 15, 340 (2003).

[112] Stafford, C.M., Harrison, C., Beers, K.L., Karim, A., Amis, E.J., Vanlandingham, M.R., Kim, H.C., Volksen, W., Miller, R.D., and Simonyi, E.E., Nat. Mater. 3, 545 (2004).

[113] Jiang, C., Markutsya, S., Pikus, Y., and Tsukruk, V.V., Nat. Mater. 3, 721 (2004).

[114] Hua, F., Cui, T., and Lvov, Y.M., Nano Lett. 4, 823 (2004).

[115] Daillant, J., and Gibaud, A., "X-ray and Neutron Relectivity: Principles and Applications", Springer Lecture Notes in Physics Vol. 770 (1999).

[116] Tolan, M., "X-ray Scattering from Soft Matter Thin Films", Springer Tracts in Modern Physics Vol. 148 (1999).

---

[117] Foster, M.D., Crit. Rev. Anal. Chem. 24, 179 (1993).

[118] Peri, S., Akgun, B., Satija, S.K., Jiang, H., Enlow, J., Bunning, T., and Foster, M., ACS Appl. Mater. Interfaces 3, 3375 (2011).

[119] Harroun, T.A., Kucerka, N., Nieh, M.-P., and Katsaras, J., Soft Matter 5, 2694 (2009).

[120] Vaknin, D., Kjaer, K.; Ringsdorf, H., Blankenburg, R., Piepenstock, M., Diedrich, A., and Losche, M., Langmuir 9, 1171 (1993).

[121] Yano, Y.F., Uruga, T., Tanida, H., Terada, Y., Takagaki, M., and Yamada, H., Langmuir 25, 32 (2009).

[122] Evers, F., Shokuie, K., Paulus, M., Sternemann, C., Czeslik, C., and Tolan, M., Langmuir 24, 10216 (2008).

[123] Sheller, N.B., Petrash, S., Foster, M.D., and Tsukruk, V.V., Langmuir 14, 4535 (1998).

[124] Green, R.J., Su, T.J., Lu, J.R., and Webster, J.R.P., J. Phys. Chem. B 105, 9331 (2001).

[125] Kent, M.S., Yim, H., and Sasaki, D.Y., Langmuir 21, 6815 (2005).

[126] Evers, F., Steitz, R., Tolan, M., and Czeslik, C.J., Phys. Chem. B 113, 8462 (2009).

[127] Haas, H., Steitz, R., Fasano, A., Liuzzi, G.M., Polverini, E., Cavatorta, P., and Riccio, P., Langmuir 23, 8491 (2007).

[128] Jean, B., Dubreuil, F., Heux, L., and Cousin, F., Langmuir 24, 3452 (2008).

[129] Losche, M., Schmitt, J., Decher, G., Bouwman, W.G., and Kjaer, K., Macromolecules 31, 8893 (1998).

[130] Russell, T.P., Karim, A., Mansour, A., and Felcher, G.P., Macromolecules 21, 1890 (1988).

[131] Dufresne, A., Molecules 15, 4111 (2010).

[132] Marsh, R.E., Corey, R.B., and Pauling, L., Biochem. Biophys. Acta. 16, 1 (1995).

[133] Takahashi, Y., Gehoh, M., and Yuzuriha, K., J. Poly. Sci. Pt. B: Poly. Phys. 29, 889 (1991).

[134] Lotz, B., and Keith, H.D., J. Mol. Biol. 61, 201 (1971).

[135] Saitoh, H., Ohshima, K.-I., Tsubouchi, K., Takasu, Y., and Yamada, H., Int. J. Bio. Macromol. 34, 259 (2004).

[136] Paulus, M., Lietz, D., Sternemann, C., Shokuie, K., Evers, F., Tolan, M., Czeslik, C., and Winter, R.J., J. Synchrotron Radiat. 15, 600 (2008).

[137] Seeck, O.H., Kaendler, I.D., Tolan, M., Shin, K., Rafailovich, M.H., Sokolov, J., and Kolb, R., Appl. Phys. Lett. 76, 2713 (2000).

[138] Fragneto-Cusani, G., J. Phys.: Condens. Matter 13, 4973 (2001).

[139] Cullity, B. D. "Elements of X-Ray Diffraction", Second Edition, Addison Wesley, (1978).

[140] Shulha, H., Wong, C., Kaplan, D.L., and Tsukruk, V.V., Polymer 47, 5821 (2006).

[141] Gopinadham, M., Ivanova, O., Ahrens, H., Guenther, J.U., Steitz, R., and Helm, C.A., J. Phys. Chem. B 111, 8426 (2007).

[142] Haas, H., Steitz, R., Fasano, A., Liuzzi, G.M., Polverini, E., Cavatorta, P., and Riccio, P., Langmuir 23, 8491 (2007).

[143] Wang, X., Kim, H.J., Xu, P., Matsumoto, A., and Kaplan, D.L., Langmuir 21, 11335 (2005).

---

[144] Shulha, H., Foo, C.W.P., Kaplan, D.L., and Tsukruk, V.V., Polymer 47, 5821 (2006).

[145] Valluzzi, R., Winkler, S., Wilson, D., and Kaplan, D.L., Phil. Trans. R. Soc. Lond. B 357, 165 (2002).

[146] Bini, E., Knight, D.P., and Kaplan, D.L., J. Mol. Biol. 335, 27 (2004).

[147] Zhou, C.-Z., Confalonieri, F., Jacquet, M., Perasso, R., Li, Z.-G., and Janin, J., Proteins: Struct., Funct., Genet. 44, 119 (2001).

[148] Omenetto, F.G., and Kaplan, D.L., Science 329, 528 (2010).

[149] Cho, J., Char, K., Hong, J.-D., and Lee, K.-B., Adv. Mater. 13, 1076 (2001).

[150] Craig, V.S.J., Soft Matter 7, 40 (2011).

[151] Song, B., Walcyzk, W., and Schoher, H., Langmuir 27, 8223 (2011).

[152] Ochanda, F.O., Samaha, M.A., Tafreshi, H.V., Tepper, G.C., and Gad-el-Hak, M. J., Appl. Polym. Sci. 124, 5021 (2012).

[153] Peri, S.R., Habersberger, B., Akgun, B., Jiang, H., Enlow, J., Bunning, T.J., Majkrzak, C.F., and Foster, M.D., Polymer 51, 4390 (2010).

[154] Kharlampieva, E., Kozlovskaya, V., Ankner, J.F., and Sukhishvili, S.A., Langmuir 24, 11346 (2008).

[155] Xia, Y., and Whitesides, G.M., Annu. Rev. Mater. Sci. 28, 153 (1998).

[156] Tsioris, K., White, R.D., Kaplan, D.L., and Wong, P.Y. Mater. Res. Soc. Symp. Proc. 1052 (2008).

[157] Zhou, Y., Chen, W., Itoh, H., Naka, K., Ni, Q., Yamane, H., and Chujo, Y., Chem. Commun. 23, 2518 (2001).

---

[158] Jang, J.-H., Ullal, C.K., Gorishnyy, T., Tsukruk, V.V., and Thomas, E.L., Nano Lett. 6, 740 (2006).

[159] Keten, S., and Buehler, M.J., Appl. Phys. Lett. 96, 153701 (2010).